

Design of a Small Wind Turbine Rotor and Hub for Wind Tunnel Testing

MSc. Thesis
Cedric van Wijk

Design of a Small Wind Turbine Rotor and Hub for Wind Tunnel Testing

Thesis

by

Cedric Franciscus Corneel van Wijk

s1356054

in partial fulfilment of the requirements for the degree of

Master of Science

in Mechanical Engineering

at the University of Twente department of Engineering Technology

Thesis committee

Chairman: prof. dr. ir. C.H. Venner¹

Supervisor: dr. ir. A. van Garrel¹

External members: Dr. A. Martinetti²

Dr. H. Özdemir^{1,3}

UNIVERSITY OF TWENTE.

June 26, 2020

¹University of Twente, Faculty of Engineering Technology (ET), Engineering Fluid Dynamics (EFD)

²University of Twente, Faculty of Engineering Technology(ET), Maintenance Engineering & Operations(MEO)

³TNO Energy Transition

Preface

This report has been written for the master thesis assignment at the University of Twente (UT). The master thesis assignment is the final assignment of the Mechanical Engineering Master's education. The master thesis is performed in close collaboration with R.F.O. van Wijk who designed a separate part of the wind turbine. This assignment was performed for the department of thermal and fluid engineering (TFE). The assignment was provided and supervised by dr.ir. A. van Garrel, assistant professor at the UT for the department of TFE. The master thesis assignment is supposed to last 8 months and was performed at the UT. The thesis is concluded with this report, a presentation and an oral exam. The presentation and exam are conducted by the examination committee that consists of the supervisor for this thesis, dr.ir. A. van Garrel, the head of the department of TFE, prof.dr.ir. C.H. Venner and Dr. A. Martinetti and Dr. H. H. Özdemir (of TNO Energy Transition)

During the writing of this thesis the COVID-19 (Coronavirus) virus spread in the Netherlands, resulting in a lockdown of the university during the final phase of this project. This meant that the wind tunnel in which tests were to be performed was not accessible for most of this phase. In the end, 1 day of testing was allowed which limited the amount of testing results. Before testing in the wind tunnel alternate testing plans were made, but its results were severely lacking and therefore the testing results and conclusions from these tests are very limited.

I would like to thank dr.ir. A. van Garrel for supervising, helping and supporting me throughout this project. I would also like to thank my brother R. van Wijk with whom I shared this assignment, he also helped me a lot with my part of the assignment. Furthermore I would like to thank ing. W. Lette for his role in supervising the building of the wind turbine and its components. I would also like to thank E.M.P. Leusing MSc, S. Wanrooij, D.R.F. de Kinkelder, Quint Meinders and especially H.L. Stobbe for their role in building the wind turbine and making this thesis possible. Finally, I would like to thank my friend Rick Zwagerman for his support and for helping out with the 'at home' experiments.

Abstract

Renewable energy is growing in importance due to the increasing scarcity of fossil fuels and their impact on the environment. The most prominent and fastest growing sector of renewable energy is wind energy. The number of wind turbines and wind turbine farms is increasing around the world. For this reason the demand for better, bigger and more efficient turbines is increasing. At the University of Twente (UT), wind turbine research is done and the topic of wind energy is taught. Wind turbine theory is taught to master students in the Wind Energy course. This course includes practical assignments such as the observation of the flow over a wing in a wind tunnel environment. However, the course does not have a practical involving wind tunnel experiments on an actual wind turbine, that would connect the Blade Element Momentum (BEM) theory taught in the course with the physical experiment. It was found that no existing design fits the needs of the wind energy course or the geometrical constraints of the wind tunnel at the UT. The need for the development of a model wind turbine for this goal was the basis for the present master thesis.

To satisfy the demand of a wind turbine practical, a new design of a wind turbine is developed. The design is created specifically for the UT aeroacoustic wind tunnel, meaning that it fits the already present mounting table and is useable at various wind speeds that the wind tunnel can reach. The wind tunnel can reach wind velocities of up to 60 m/s , however for safety reasons the operating range of the turbine is much lower: up to 13.8 m/s wind speed

In this thesis the design and construction of the wind turbine rotor is discussed. The rotor is designed to be modular and to have an adaptable blade pitch. The design process is documented in detail. The rotor performance is predicted using Beam Element Momentum (BEM) theory and the numerical program QBlade, which uses the same theory. Both results are compared to each other. The rotor is tested in simple experimental setups, indicating the basic functionality of the wind turbine and its rotor, as well as in the university's wind tunnel, creating a more detailed overview of the wind turbine performance. Further testing in the wind tunnel is recommended to completely map the rotor performance at different pitch angles, tip speed ratios and wind speeds, as well as to include effects that were not yet taken into account, such as the blockage effect. The result of the thesis is a wind turbine that can be used for demonstrative practicals and future research in the wind tunnel.

Contents

1	Introduction	1
1.1	Background	1
1.2	Existing Technology	2
2	Starting Points for Wind Turbine Design	5
2.1	Research Goal	5
2.2	The Aeroacoustic Wind Tunnel	5
2.3	Design Choices	7
2.4	Requirements	8
3	Analysis	11
3.1	Force Analysis	11
3.2	Wind turbine airfoils	13
3.2.1	Defining airfoils	14
3.2.2	Airfoil Non-Dimensionalization	16
3.3	BEM Theory Blade Design	17
3.3.1	Momentum Theory	17
3.3.2	Blade Element Theory	19
3.3.3	Applying BEM Theory to Determine Blade Shape	20
3.3.4	Tip and Root Loss	20
3.3.5	Other Effects on Blade Performance	21
4	Aerodynamic Rotor Design	23
4.1	Airfoil Selection	23
4.2	Preliminary Blade Design Using BEM Theory	24
4.2.1	Blade geometry	24
4.2.2	Performance Prediction	25
4.3	QBlade Design Process	27
4.3.1	Airfoil and Polar Creation	27
4.3.2	QBlade Geometry Design	29
4.4	Rotorblade concepts	31
4.4.1	Concept 1: The Matlab Design	31
4.4.2	Concept 2: The QBlade Design	31
4.4.3	Concept 3: The Linear Chord	31
4.4.4	Concept 4: The Multi-Foil	32
4.5	Concept Choice	32
5	Detailed Design	35
5.1	Geometry Design	35
5.1.1	The Rotor Hub	35
5.1.2	The Blade Foot	35
5.1.3	The Blade Root	36
5.2	Material Choice & Production Method	36
5.2.1	The Rotor Hub	37
5.2.2	The Blade Foot	37
5.2.3	The Blades	38
5.3	Force Analysis	40

5.3.1	Global Forces	40
5.3.2	Local Forces	43
5.4	Performance Predictions	45
5.4.1	Simulation Corrections	45
5.4.2	Varying TSR	46
5.4.3	Varying Blade Pitch Angle	46
5.4.4	Varying Wind speed	48
5.5	The Definitive Rotor Assembly	50
6	Testing and Results	51
6.1	Test 1: The Car Test	51
6.1.1	Test 1 Setup	51
6.1.2	Test 1 Results	53
6.2	Test 2: The Fan Test	53
6.2.1	Test 2 Setup	53
6.2.2	Test 2 Results	54
6.3	Test 3: Wind Tunnel Testing	57
6.3.1	Test 3 Setup	57
6.3.2	Test 3 Results	58
7	Conclusions & Recommendations	63
	Appendices	66
A	BEM Equations Derivation	67
A.1	Momentum Theory	67
A.1.1	Blade Element Theory	70
A.1.2	Applying BEM Theory to Determine Blade Shape	71
A.1.3	Tip and Root Loss	73
B	Lift Over drag Graphs for Selig Airfoils	75
C	SD7037 Selig Polar File	79
D	Rotorblade Tables for Concept Rotors	81
E	Technical Drawings	83
F	PA2200 Material properties	89
G	Wind Tunnel Test Data	91
H	Matlab Code for Preliminary Blade Design	95
I	Matlab Code for Rotor Performance Predictions	103

Nomenclature

A	$[m^2]$	Surface area
a	$[-]$	Axial induction factor ($a = \frac{U_1 - U_2}{U_1}$)
a'	$[-]$	Angular induction factor ($a' = \frac{\omega}{2\Omega}$)
B	$[-]$	Number of blades of the wind turbine
c	$[m]$	Airfoil chord length
c_{Betz}	$[m]$	Betz optimal chord length
C_d	$[-]$	Drag coefficient
c_I	$[m]$	Chord length approximation
C_l	$[-]$	Lift coefficient
C_p	$[-]$	Power coefficient
C_q	$[-]$	Torque Coefficient
$c_{Schmitz}$	$[m]$	Schmitz optimal Chord length
C_t	$[-]$	Thrust coefficient
D	$[kgms^{-2}]$	Drag force (also F_D)
D_{foot}	$[m]$	Blade foot component diameter
E	$[kgm^{-1}s^{-2}]$	Elasticity modulus
F_D	$[kgms^{-2}]$	Drag force (also D)
F_M	$[kgms^{-2}]$	Moment driving force
F_c	$[kgms^{-2}]$	Centrifugal force (also $F_{centrifugal}$)
$F_{centrifugal}$	$[kgms^{-2}]$	Centrifugal force (also F_c)
F_L	$[kgms^{-2}]$	Lift force (also L)
F_T	$[kgms^{-2}]$	Thrust force (also T)
$F_{tip/root}$	$[-]$	Prandtl tip/root loss correction factor
F_{wind}	$[kgms^{-2}]$	Wind force exerted on rotor blade(s)
F_0	$[kgms^{-2}]$	Internal clamping force on blade at root
I	$[m^4]$	Area moment of inertia
L	$[kgms^{-2}]$	Lift force (also F_L)
l	$[m]$	Characteristic length
M	$[kgm^2s^{-2}]$	Blade moment
m	$[kg]$	Blade (section) mass
M_0	$[kgm^2s^{-2}]$	Internal clamping moment at blade root
\dot{m}	$[kgs^{-1}]$	Mass flow
$M(w)$	$[kgm^2s^{-2}]$	Momentum equation
M_p	$[kgm^2s^{-2}]$	Pitching moment
Ma	$[-]$	Mach number
N	$[-]$	Blade element section number
P	$[kgm^2s^3]$	Power generated by the wind turbine rotor
p	$[kgm^{-1}s^{-2}]$	Static pressure
P_{wind}	$[kgm^2s^{-3}]$	Power in the wind
p_{1-4}	$[kgm^{-1}s^{-2}]$	Static pressure at locations 1-4
Q	$[kgm^2s^{-2}]$	Rotor torque
r	$[m]$	Local radius
R	$[m]$	Blade radius
Re	$[-]$	Reynolds number
T	$[kgms^{-2}]$	Thrust force (also F_T)
t_{foot}	$[m]$	Blade foot component thickness
t_I	$[m]$	Airfoil thickness approximation

TSR	$[-]$	Tip speed ratio ($TSR = \frac{\Omega R}{U_{wind}}$)(also λ)
U_{rel}	$[ms^{-1}]$	Wind velocity relative to the blade at the rotor
U_{rel1}	$[ms^{-1}]$	Wind velocity relative to the blade in the free stream
U_{rot}	$[ms^{-1}]$	Axial velocity in the rotor
U_{wind}	$[ms^{-1}]$	Free stream wind velocity
U_{1-4}	$[ms^{-1}]$	Absolute wind velocities at locations 1-4
\vec{v}	$[ms^{-1}]$	Wind velocity vector
w	$[ms^{-1}]$	Rotor velocity in plane of rotation
w_{UDL}	$[kgs^{-2}]$	Divided gravitational load on the blade
y	$[m]$	Distance from neutral axis to bending location
α	$[-]$	Angle of attack (AoA)
θ	$[-]$	Blade twist angle
θ_{Betz}	$[-]$	Betz optimal twist angle
θ_{pitch}	$[-]$	Blade pitch angle
$\theta_{Schmitz}$	$[-]$	Schmitz optimal twist angle
λ	$[-]$	Tip speed ratio (also TSR)
λ_r	$[-]$	Local tip speed ratio at radius r
μ	$[kgm^1s^1]$	Dynamic fluid viscosity
ρ	$[kgm^{-3}]$	Fluid density
σ	$[kgm^{-1}s^{-2}]$	Bending stress
τ	$[kgm^{-1}s^{-2}]$	Shear stress
φ	$[-]$	Angle of relative wind with the rotor plane at the rotor
φ_{Betz}	$[-]$	Betz optimal angle of relative wind
$\varphi_{Schmitz}$	$[-]$	Schmitz optimal angle of relative wind
φ_1	$[-]$	Angle of relative wind with the rotor plane in the free stream
Ω	$[s^{-1}]$	Angular velocity
ω	$[s^{-1}]$	Wake rotation angular velocity

Chapter 1

Introduction

1.1 Background

Wind energy and therefore wind turbines are becoming increasingly important as a source of energy. According to the BP Statistical Review of World Energy, it is the largest and the fastest growing branch of renewable energy in the world, as can be seen in Figure 1.1. In 2018 ca 1300 TWh of energy was produced, around 5% of global electricity produced [1]. It is expected that by 2030, 25% of total electricity will be renewable and by 2040, this will most likely increase to 45%. Wind energy will play a significant role in the development. More and more wind farms are installed and wind turbine technology is advancing at a rapid pace. Average wind turbine size is increasing and the average turbine output is increasing as well. An indication of wind turbine size can be seen in Figure 1.2 An average onshore wind turbine puts out 2 - 5 MW at peak performance with some of the newest off-shore wind turbines producing 12 MW, like the Haliade X prototype in the port of Rotterdam, which has a rotor diameter of 220 m, the largest in the world. At the moment, only 4% of wind energy is produced in off-shore facilities due to technological and financial constraints, however this is expected to increase drastically in the coming years[2].

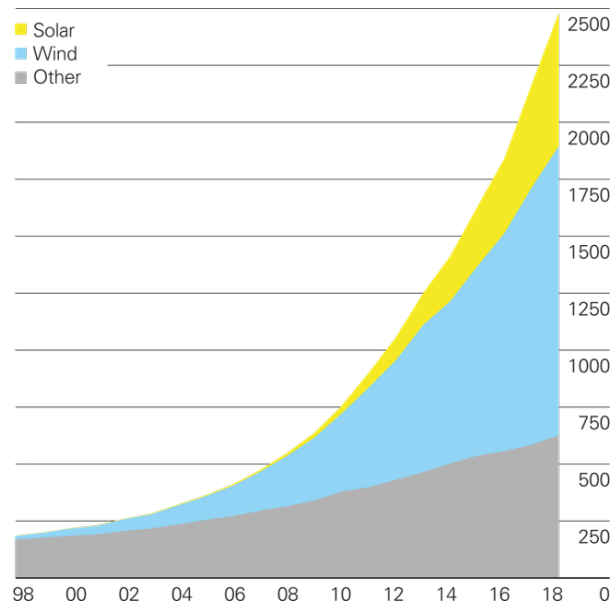


Figure 1.1: Energy production in TWh of different sources of renewable energy over the years [1].

At the University of Twente the design of wind turbines and farms, as well as the science of wind energy conversion systems are taught in the master course "Wind energy". During this course students are introduced to wind energy conversion systems, like wind turbines. The course also includes a practical in a wind tunnel, where flow over a wing is examined in order to create an understanding of the aerodynamic workings of airfoil shapes.

However, the course and the practical do not include the study of a physical wind turbine. It is suggested

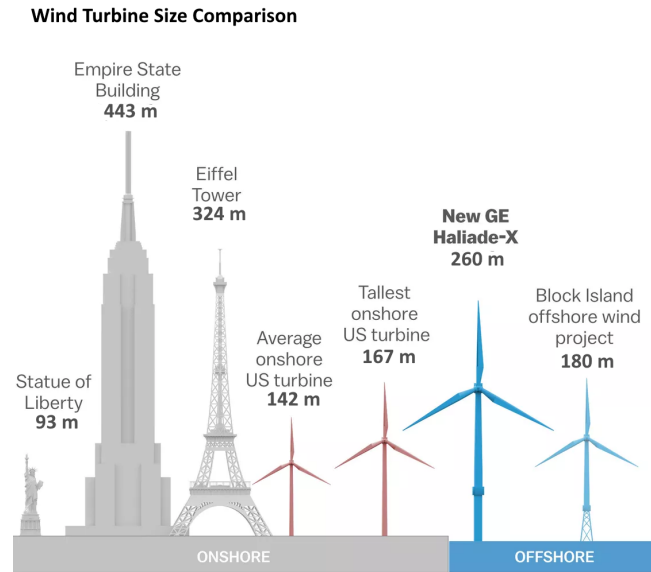


Figure 1.2: Indication of wind turbine sizes [3].

that in order to create an understanding of not only the aerodynamic properties of a single wing, but the entire workings of a wind turbine, another practical should be added that does include the study of a physical wind turbine in wind tunnel tests. The wind turbine should be a small scale wind turbine that is of suitable size for the UT (University of Twente) aeroacoustic wind tunnel. It should also operate in wind conditions set by this wind tunnel. In order for students to have an interactive and educational experience during the use of this wind turbine, it is necessary that performance statistics, force (torque/RPM/thrust etc.) measurements and other information can be measured and documented by the user. This, in turn can be compared to theory to add an empirical and physical aspect to the learning goals of the wind energy course. The wind turbine can also be applied for further research at the UT.

This research focuses on the design of a rotor for such a small wind turbine. In order to make the wind turbine interesting for research and teaching, blades are designed that fit various operating conditions. For instance, it should be possible to replace the blades with new ones or change pitch angles and observe the effects on the wind turbine performance. To create such a wind turbine rotor an aerodynamic analysis is done and blades are designed. The rotor (and the rest of the turbine) will be build and tested for this research, therefore the research includes building plans like material selections and production method design. The final product of the research includes an operating wind turbine rotor, test results of the wind turbine and finally a report on the wind turbine design process. All of these can contribute to the wind energy course and practical.

1.2 Existing Technology

To find if it is necessary to develop a wind turbine for the aforementioned goals, existing small scale wind turbines are considered for the use in lecture practicals and research. such wind turbines can be found in (online) stores and their suitability for wind energy course practicals is considered. Wind turbine testing and research is already done and wind turbines for this goal already exist. Currently used research turbines are considered for use in the UT wind tunnel.

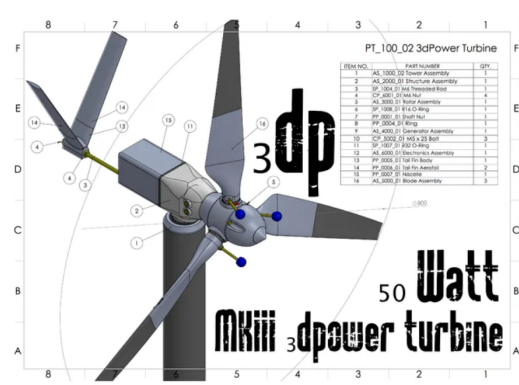
A restricting factor for the design of the wind turbine is its size. The turbine is required to fit inside the operational area of the UT aeroacoustic wind turbine, which is $700 \times 900 \text{ mm}^2$. Buying an existing turbine, as well as using an existing design is considered. Research into buying a small wind turbine indicates that the required size of the wind turbine makes for a very small number of suitable wind turbines. Wind turbines defined as 'small' generally have a rotor diameter of over 1 meter and are mounted on boats or houses. These wind turbines are too large and generally very expensive ($> 1000\text{€}$). Smaller wind turbines (miniature wind turbines) are scarcely available and of much lower quality. Their applications are generally orientated towards charging batteries or simply as a toy. A typical example of such a wind turbine is the 'Texenergy Infinite Air' [4] wind turbine in Figure 1.3a, which has a diameter of only 280 mm . This wind turbine, like others available in this

size, is of poor quality, is not able to adjust pitch or regulate rotation speeds and is therefore not suited for the research goal. Furthermore, if such a turbine should be used, sensors for RPM, thrust, torque etc. have to be mounted on the exterior of the wind turbine, as there is no space inside the nacelle, which is another big disadvantage, because sensors would be vulnerable to exterior influence.

Independent designers also have created wind turbines of relevant size and are shared for free on the internet. Good examples of these are the wind turbines available on Thingiverse[5], a website sharing 3D printable designs. These designs only require a 3D printer and some basic components like nuts, bolts and bearings. An example of such a design is the 'MKIII 50 Watt 3d printable Wind Turbine' [6] in Figure 1.3b. Which is a 3D-printable wind turbine with a diameter of ca. 400 mm. This is a design that features a passive variable pitch (PVP) system that automatically optimises pitch angle. This design is more interesting, however, it does not include (space for) any sensors. Furthermore, the PVP system is not ideal for research situations, where pitch has to be regulated manually. The fully 3D-printed design also makes the wind turbine rickety, due to printing mistakes and the printed plastic not being very stiff.



(a) 'Texenergy Infinite Air' wind turbine [4]



(b) 'MKIII 50 Watt 3d printable Wind Turbine' [6]

Figure 1.3

Wind tunnel testing on small/scaled down wind turbines is already done. However, generally these tests are still performed with bigger turbines and in bigger wind tunnels than the UT wind tunnel. An example are the tests done by Botasso et al.[7] Where a scaled down model based on the Vestas V90 was tested in a large wind tunnel. The model was scaled down to 1/45 of its original size, resulting in a 2 m rotor diameter. This size insured enough space for a large number and variety of sensors. Still allowing two turbines to be placed in front of each other, while still avoiding excessive blockage. Such a large design allows for many sensors, including sensors that can track rotor blade location and pitch angle. A large size is also helpful when trying to reach higher (> 100.000) Reynolds numbers in the flow while limiting the required RPM to do so.

Another example of a wind turbine used is the BeRT (Berlin Research Turbine) developed at the Technical University of Berlin, shown in Figure 1.4. This wind turbine developed for wind tunnel testing includes an active load control system and a variety of high-end sensors that can measure surface pressures, inflow angle, blade tip acceleration, blade root bending moments, angular flap position and angular rotor position. This turbine has a diameter of 3 m and is therefore considered too large for application in the UT wind tunnel, however the sensors on this wind turbine are very elaborate and are able to measure both turbine performance, as well as aerodynamic properties. Although in an ideal case the wind turbine for the UT wind tunnel is also able to measure these properties, it is likely that due to its small size, the sensors will not fit or will influence the turbine performance properties. The wind turbine design for this thesis will mostly focus on mapping turbine performance properties, rather than aerodynamic flow properties at the rotor. However the BeRT is considered to be a good example of an ideal case end result, if its properties and measuring capabilities could be transferred to a smaller wind turbine for the UT wind tunnel. Finally, the BeRT was developed and optimised using QBlade a free software used to design wind turbine rotors, this software will also be applied in the research in this thesis.

Although the existing technologies are in some ways a good fit for the UT wind tunnel, they do not meet the needs for use in the UT wind energy practicals. The option of buying a commercially available turbine or 3D-printing an existing designing would result in a turbine that would fit the UT wind tunnel, but would not



Figure 1.4: The Berlin Research Turbine 'BeRT'.

include (space for) sensors that map the turbine performance. Furthermore, a turbine of which the optimal performance properties and the blade and rotor geometry is unknown means that rotor performance is hard to predict. These predictions are an interesting part of the wind energy course and would be an integral part of the wind energy practical. Furthermore existing wind tunnel experiments generally include a much larger turbine with very high-end and expensive sensors that can give more information, but is considered too elaborate for the practical's teaching goal. This means that the design of a new turbine is considered necessary. This thesis aims to create a design that fully meets the requirements for the UT wind energy course and to create a wind turbine that fits the UT aeroacoustic wind tunnel perfectly.

Chapter 2

Starting Points for Wind Turbine Design

2.1 Research Goal

The problem as stated in the introduction is to design a small scale wind turbine rotor. The wind turbine design assignment is divided into two parts: The design of the rotor and the nacelle. The rotor design includes the design of the rotor blades and the hub, how these fit together and how they are attached to the nacelle. The design of the nacelle includes the design of the drive train, the generator, measurement systems/sensors and structural connection of the nacelle to the operating environment. The design of the nacelle is done by R.F.O. van Wijk, as a master thesis at the University of Twente. The assignments are performed in tandem and good communication during the execution of both assignments is maintained. The design process of the nacelle is not considered in the report and the nacelle design is not considered as a factor during the aerodynamic analysis of the blade performance. Furthermore, the nacelle design is expected and assumed to fulfil the requirements that are set in relation to measurement capability and structural integrity of the wind turbine.

The goal of this thesis is to design, build and test a small wind turbine rotor that is part of a small wind turbine that can be used in the University of Twente aeroacoustic wind tunnel. The wind turbine is designed for use in the Wind Energy course practical as well as for research at the UT involving wind turbines.

2.2 The Aeroacoustic Wind Tunnel

The wind turbine is to be operated in the UT aeroacoustic wind tunnel. To create an effective wind turbine design for this wind tunnel, its properties are considered.

The aeroacoustic wind tunnel is known as a 'silent' wind tunnel, because its walls are designed to absorb almost all noise produced by the airflow. The anechoic chamber in which the flow is present and where experiments are done, has dimensions of $6\text{ m} \times 6\text{ m} \times 4\text{ m}$. Inside, a table is mounted that allows the mounting of test setups. The table top is 1.435 m from the floor and can be rotated 360° . Directly above the table top, the air from the wind tunnel flows. Above the table a 'ceiling' can be mounted at the point where the flow stops (in case of the biggest nozzle). The flow area of the wind tunnel is $700\text{ mm} \times 900\text{ mm}$ when the biggest nozzle is mounted, and $351\text{ mm} \times 450\text{ mm}$ when a smaller nozzle is mounted. The smaller nozzle is mounted in case higher flow velocities are required. A render of the table with the wind turbine setup can be seen in Figure 2.1

The aeroacoustic wind tunnel can reach flow velocities of 240 km/h . A schematic view is displayed in Figure 2.2 and the most important parts are mentioned. The wind tunnel is driven by an 130 kW electrical motor driving two large radial turbines (1). To prevent the heating of air, the air is cooled in a water-cooled heat exchanger (2). The flow is directed through a settling chamber (5) and some anti-turbulence grids (6), producing a laminar airflow. The flow exits the nozzle (7) and enters a closed test section (8), after which it flows into the anechoic chamber (9) where the table is mounted. The flow exits at (10) and a closed system is formed [8].



Figure 2.1: The wind turbine experiment setup in the UT wind turbine.

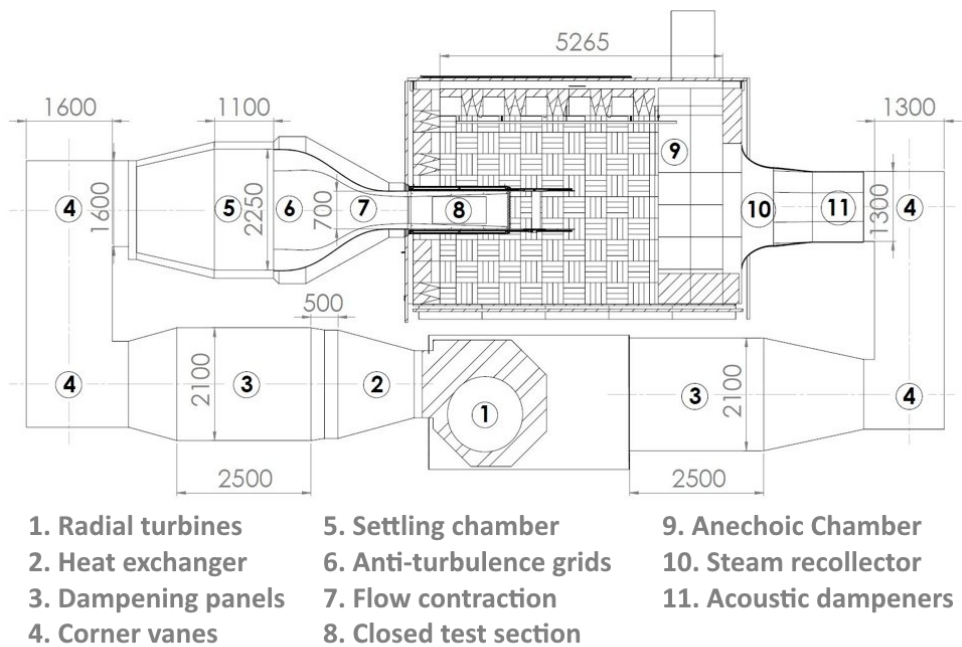


Figure 2.2: Schematic view of the aeroacoustic wind tunnel at the UT. [8]

2.3 Design Choices

The to-be-designed wind turbine will be a Horizontal Axis Wind Turbine (HAWT). The design will not focus on optimal performance in a given situation, but instead emphasises applicability in different testing situations, such as different wind speeds, rotation speeds, pitch angles, etc. Furthermore, the design is to be used as an up-wind as well as a down-wind turbine. This means that rotation in both directions should be possible, the design should be able to withstand forces from both directions and the rotor should be able to be either mounted on the back, or the entire turbine should be turned around and the blades/rotor changed to face the other way.

The wind turbine is to be applied in the UT aeroacoustic wind tunnel. During the operation the bigger nozzle will be mounted. This means a flow area of $0.7 \times 0.9 \text{ m}^2$ is available. To prevent the "edge" of this area to influence the wind turbine experiments, it is suggested to make the rotor diameter 500 mm . This ensures a minimal distance of 200 mm with the flow area edge and lessens boundary effects of the flow from influencing rotor performance in experiments. A velocity range of operation has to be chosen for the wind turbine. The wind tunnel can reach wind velocities up to 65 m/s , but this is much faster than wind speeds during normal wind turbine operating conditions. The energy in the wind is kinetic and the power follows the equation:

$$P_{wind} = \frac{1}{2} \rho A U_{wind}^3 \quad (2.1)$$

An increase in wind velocity means a cubed increase in power. This means a vast difference in power between low and high wind speeds. Furthermore, at a given tip speed ratio (TSR) > 1 another problem arises. The tip speed ratio means the ratio of the wind speed and the blade speed at the tips of the blades. this can be expressed with the equation:

$$TSR = \frac{\Omega R}{U_{wind}} \quad (2.2)$$

Where Ω is the angular speed of the wind turbine rotor, R is the blade radius and U_{wind} is the free stream wind velocity.

At a given tip speed ratio (TSR) > 1 , high wind velocities will result in extremely high rotation and tip speeds, which can be dangerous. It is also hard to find a generator that can operate at this range of power. For this reason, a wind velocity range is chosen at lower wind speeds. The cut-in speed of the wind turbine is unknown, however the operation wind speed of the wind turbine is set at 11.11 m/s (40 km/h), meaning the turbine will be optimised for operation at this wind speed. The maximum wind speed for which the wind turbine can be applied is set at 25 m/s . This wind speed should result in a manageable power output and not result in excessive and dangerous rotation velocities. The wind turbine is required to function at all wind velocities between $11.11 - 25 \text{ m/s}$ and preferably starting at a speed of 5 m/s or lower

In wind turbine design, two important choices are the number of blades and the optimal Tip Speed Ratio (TSR). A wind turbine rotor optimisation can be performed with a specific TSR and number of blades in mind. More blades generally mean higher efficiencies, however, after 3 blades the increase in efficiency quickly becomes marginal. Moreover, more blades can increase the complexity of the construction and increase material costs. Therefore, it is opted to choose between either 2 or 3 blades.

Wind turbine efficiency is generally expressed in the form of the power coefficient C_p . This power coefficient expresses the amount of kinetic energy that is converted into rotor rotation and torque by the wind energy. It is the fraction of P_{wind} in Equation 2.1 extracted by the wind turbine:

$$C_p = \frac{P}{P_{wind}} \quad (2.3)$$

Where C_p is the power coefficient, P is the rotor power and P_{wind} is the total power in the wind.

It is proven that this power coefficient can not exceed 0.593. This is called the Betz limit, because it was first discovered by Albert Betz in 1919 [9]. The reason a wind turbine can not be 100% efficient is that in order to reach such an efficiency, the wind has to be completely stopped by the wind turbine. This would mean that the air behind the turbine is standing still, preventing more wind from coming into the turbine. The goal in designing a wind turbine is to get as close to this Betz limit as possible. Common wind turbine efficiencies are in the 35 – 45% range. [9]

To help make a decision if 2 or 3 blades are used, Figure 2.3 is observed. It compares efficiencies of rotors with 2 or 3 blades with different airfoils. The airfoil differences are defined by the lift over drag ratio C_l/C_d . C_l and C_d are the lift and drag coefficients, respectively. These are aerodynamic characteristics of an airfoil that influence the rotor efficiency. The optimal airfoil is dependent on the Reynolds number along the blade radius and will be determined later. Using the figure, a choice for the number of blades and the applied TSR can be made. In the figure it can be seen that 3 blades can increase the efficiency by up to 4% at certain TSRs (and for certain lift over drag C_l/C_d values) [10]. Even though this increase in efficiency is quite small, it is assumed the complexity and material cost increase for 3 blades will not be very significant. Finally, a three bladed model is considered more aesthetically pleasing, as it more resembles the common known image of a wind turbine.

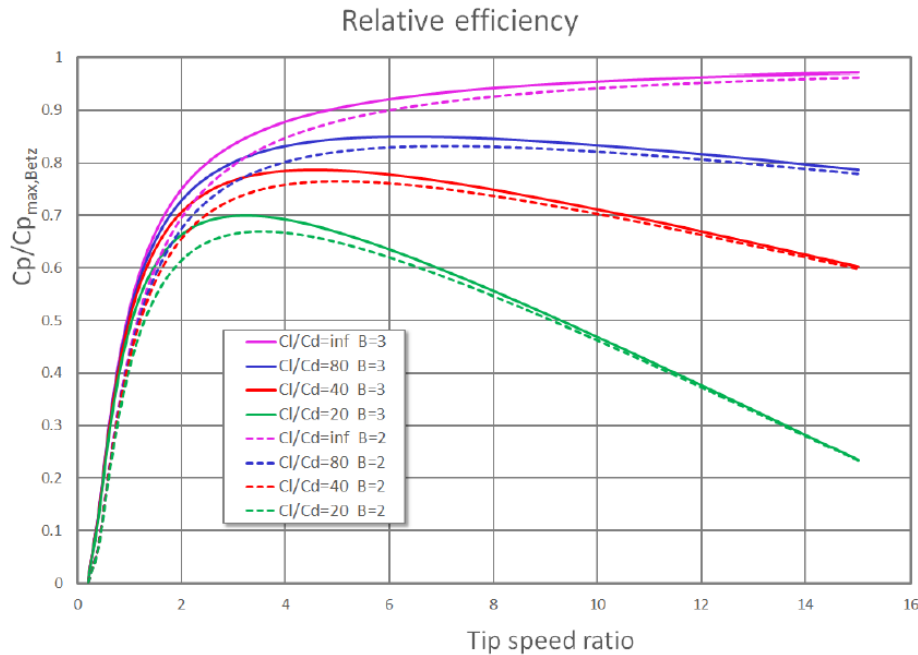


Figure 2.3: TSRs versus different lift over drag ratios for 2 or 3 bladed wind turbines. [10]

The design TSR impacts the efficiency of a turbine. A higher TSR means a higher rotation speed, resulting in less losses in the wake rotation. A low TSR results in higher torque [10]. Since the wind turbine design is relatively small, meaning a small blade radius, the turbine will have to operate at relatively high rotation speeds, compared to a wind turbine with the same TSR, but longer blades. Because of this, it is desirable use a lower TSR. High TSRs will result in very high rotation speeds, which might be impossible to reach or might lead to problems due to the centrifugal forces working on the rotor. In addition, using a low TSR will result in more wake rotation and stronger tip vortices, which lowers the rotor efficiency, but this is an interesting phenomenon to research and/or show in a practical. Using a lower TSR will make it easier to observe and measure tip vortices and wake rotation effects during research. Because of this reason, the chosen optimal TSR for the rotor is chosen to be 4, which is relatively low. Note that even though the blades will be optimised for a TSR of 4, the wind turbine should be able to operate and function at both lower and higher TSRs.

2.4 Requirements

A list of requirements is made to determine the operating conditions of the wind turbine. The requirements are split into quantitative and qualitative requirements. The list of requirements can be used to during the design process and is used to determine the success of the final product.

Quantitative requirements

The designed wind turbine:

- has 3 blades

This is a design choice made in the previous section.

- has optimal performance at a TSR of 4
A TSR of 4 is relatively low, making it easier to observe wake rotation and tip vortex effects. A low TSR is also considered safer, because the turbine will operate at lower RPM.
- can operate in a wind speed of at least 8.33 *m/s* up to 25 *m/s*
It is desirable to have a large range of wind speeds at which the turbine can operate, to create a large range at which tests can be done. To ensure that there is not too much energy in the wind and to prevent dangerous situations these wind speeds (which are relatively low for the UT wind tunnel) are chosen.
- can operate at a TSR of 2 to 6
It is desirable to be able to perform tests at TSRs both lower and higher than the optimal TSR of 4, using this range should result in safe rotation speeds and a wide enough range.
- has an adjustable pitch of 360°
Adjustable pitch will create an interesting array of measurements for various pitch angles. Since it is considered to be relatively easy to create a round blade base, a 360° range should be easily attainable.
- has a minimal power coefficient of 0.3 at optimal settings
It is expected that many mechanical losses and aerodynamic effects will influence the turbine. The set power coefficient is considered realistic and efficient enough, in comparison to existing small scale wind turbines.
- has a maximum diameter of 500 *mm*
This makes the turbine fit in the wind tunnel and leaves enough room to be at a safe distance from the edges of the experiment table in the wind tunnel.

Qualitative requirements

The designed wind turbine:

- can measure the RPM of the rotor
- can measure the rotor torque
- can measure the rotor thrust
- can measure rotor pitch
RPM, torque, thrust and pitch are important parameters to map the wind turbine performance
- generates electricity
- can measure the generated electricity
It is interesting to study the conversion of mechanical power to electric power. The electric system can also be used to influence operating TSR.
- is produced at low cost
Since the research is conducted as a master thesis, only limited financial resources are available. Furthermore, this is the first attempt at designing this kind of wind turbine, further financial investments can be done off the basis of this project, if it is a success.
- has detachable blades
It was decided that being able to replace the blades with other blade designs could be part of an interesting project or assignment for students following the wind energy course, for instance by having a competition of designing the most efficient blades.
- is safe to use at the mentioned wind speeds
Safety is very important, because it is expected that experiments will be conducted with people present in the wind tunnel during operation. Their safety is important as well as preventing damage to the wind tunnel in the case of a malfunction.

- is compatible and can connect to the existing experiment table in the wind tunnel
The existing experiment table is hard to remove or replace. Furthermore, it provides a very good base for the wind turbine.

Chapter 3

Analysis

3.1 Force Analysis

A preliminary force analysis is done to determine all the working forces on the rotor. Several forces occur on the rotor part of the wind turbine, both dynamic and static. The rotor experiences aerodynamic loads and centrifugal forces, resulting from the rotation of the rotor. Fatigue loads can occur during long-term use of the wind turbine. Gravitational loads and a horizontal load due to the wind in the wind tunnel are also present. The wind in the wind tunnel is steady and uniform, therefore at constant wind speed this load does not fluctuate (much). the gravitational load results in bending in flap-wise direction and the horizontal load results in bending in edgewise direction of the rotor blades. These loads and how to determine them are discussed below.

Aerodynamic load

The aerodynamic load on the rotor blades is a result of the lift and drag occurring along the airfoil. These forces can be determined when the shape of the airfoil is this determined. It also requires the angle of attack, the angle between the relative flow velocity and the chord line of the airfoil, to be known. The resulting forces can be seen below in figure 3.1. This figure shows the lift and drag forces, as well as the thrust and reaction forces of the wind turbine rotor.

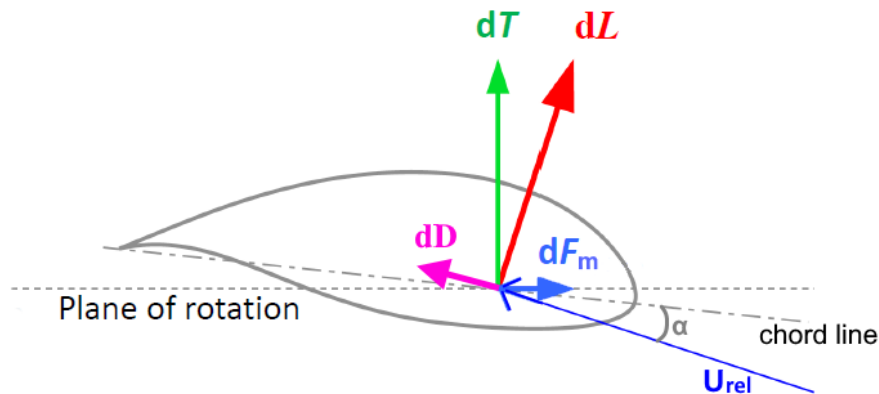


Figure 3.1: Forces working on the blades of a horizontal axis turbine. [11]

After determining the airfoil shape, the lift and drag forces can be determined using the lift and drag coefficients, which are dependent on airfoil properties and the angle of attack (α), the Reynolds (Re) number and Mach number (Ma). For slow turning situations, the coefficient is not dependent on the Mach number [12]. Determining the lift coefficient is complex and is usually done experimentally or through numerical simulations [13]. Knowing the lift and drag coefficients, the lift and drag forces can be determined for a blade section with

constant chord length with the following equations:

$$L = \frac{1}{2} C_l \rho U_{rel}^2 A \quad (3.1)$$

$$D = \frac{1}{2} C_d \rho U_{rel}^2 A \quad (3.2)$$

Where U_{rel} is the relative wind speed, ρ is the air density and A is the wing area.

The resulting lift and drag forces are converted to a useful reaction force (F_m) and thrust (T). The reaction force F_m , induces a moment on the axle and drives the rotation of the wind turbine. The thrust force (T) causes bending out of the rotor plane. The design of the rotor blades has to resist this force with limited deformation [11].

Centrifugal forces

Due to the rotation of the rotor, the blades are subjected to centrifugal forces along the blade. These forces are dependent on the mass of the blades. According to Schubel, turbines under 10 meters have negligible inertial loads and for turbines over 70 meters these loads are critical [11]. The purpose of the research is to design a small turbine ($R \ll 10 m$). However, the rotational speed is relatively high. Since the centrifugal force scales with the square of the rotation speed and is dependent on the mass of the blade, the centrifugal force might be critical. The general equation for centrifugal force of an object with mass m spinning around a point at radial distance r with rotational velocity ω is:

$$F_{centrifugal} = m\Omega^2 r \quad (3.3)$$

However, this equation considers a point mass. For the wind turbine case the load case is slightly different, with the mass of blade divided over the radius. Depending on the shape and size of the rotor blades the centre of mass of the blades can move away from or towards the hub. Therefore the centre of mass of the blades must be known. To see if the blades wont break under the centrifugal force, the internal forces of the blade have to be known, again dependent on the blade mass distribution over r .

Resulting in:

$$F_{centr}(r) = \int_r^R \omega^2 r(d)m \quad (3.4)$$

Edgewise bending

Edgewise bending stress occurs as a result of gravity on the blade mass. It alternates sign during each rotation. For small turbine blades this bending stress is very small. Only at turbines of a diameter of 70 m and over, this load becomes critical [11]. This means that this load is most definitely not critical for the proposed project. However, for completeness sake, the load is still examined. The gravitational load can be examined as a distributed load (the blade mass) in a cantilever beam equation. The maximum bending stress occurs when the turbine blade is in horizontal position. The load case can be seen in figure 3.2. Here the gravitational force is modelled as a distributed load w dependent on blade dimensions and edgewise bending deflection is determined using the equation for bending angle or using a FEM method.

$$\frac{d^2 y}{dx^2} = \frac{M(w)}{EI_x} \quad (3.5)$$

Where y is the deflection, M is the bending moment dependent on distributed load w , E is the Young's modulus of the material and I_x is the area moment of inertia. Using this, the bending stress can be calculated:

$$\sigma = \frac{My}{I} \quad (3.6)$$

Because w and I are dependent on blade geometry and mass which varies over the radius, using a FEM method will be the preferred method of determining the bending deflection and stress.

Because there is a point with a maximum stress in edgewise direction (when the blade is horizontal), fatigue stress can occur. This fatigue stress is determined by the amount of cycles that the turbine performs in its

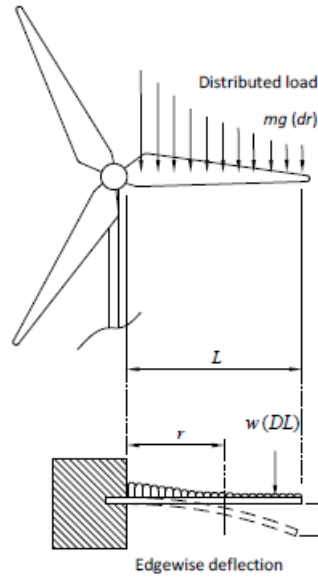


Figure 3.2: Gravitational load modelled as a cantilever beam. [11]

life. A cycle for the wind turbine is defined as a full rotation of the wind turbine rotor. In this cycle, the blade experiences the maximum load twice, each time it reaches a horizontal position. In both cases the stress is in reversed direction, relative to the blade. Since the turbine will perform a large amount of cycles, the applied maximum stress has to be well below the fatigue strength of the chosen material, to prevent deformation. The fatigue strength of a material is determined by the amount of cycles and the stress range ($\sigma_{max} - \sigma_{min}$). Because the wind turbine has such a small radius and will most likely have light-weight blades, it is not expected that edge-wise bending stress or fatigue loads due to these stresses will be significant.

Flapwise bending

Flapwise bending is the result of the aerodynamic load on the blade. In the design of an outdoor wind turbine, the extreme case of a long-lasting storm is used to determine the (extreme) aerodynamic loads on the turbine blades. For the proposed wind turbine used in a wind tunnel, the extreme case of the highest operable wind velocity can be used. The wind pushes against the blade and causes flapwise bending, this can be approached using the fundamental beam bending equation. The situation is shown in figure 3.3.

The uniformly distributed load (w_{UDL} , also just w) is dependent on the wind conditions at the blade. As mentioned, the maximum operating velocity is chosen for this case. In the determined operating conditions, 25 m/s was set as the maximum operating condition for this case. Assuming all the wind is stopped by the blade (worst-case) then the maximum force the wind can apply to the turbine blade would be:

$$w_{UDL} = \frac{F_{wind}}{L} = \frac{\frac{1}{2}\rho U_{wind}^2 \frac{1}{3}A_{total}}{L} \quad (3.7)$$

Where F_{wind} is the total thrust force of the wind on the rotor (1/3 for one blade), A_{total} is the total swept area of the wind turbine rotor (πR^2), ρ is the density of air and U_{wind} is the maximum operable wind speed of the wind turbine. When these are known, the flapwise bending stress can be calculated with the cantilever beam equation for a uniformly distributed load on a clamped beam:

$$\sigma = \frac{My}{I} = -\frac{\frac{1}{2}w_{UDL}(R-r)^2 y}{I} \quad (3.8)$$

3.2 Wind turbine airfoils

For the wind turbine to operate correctly and efficiently, an airfoil shape has to be selected. An airfoil is a structure with a geometrical shape that creates mechanical forces due to the relative motion of the airfoil and a

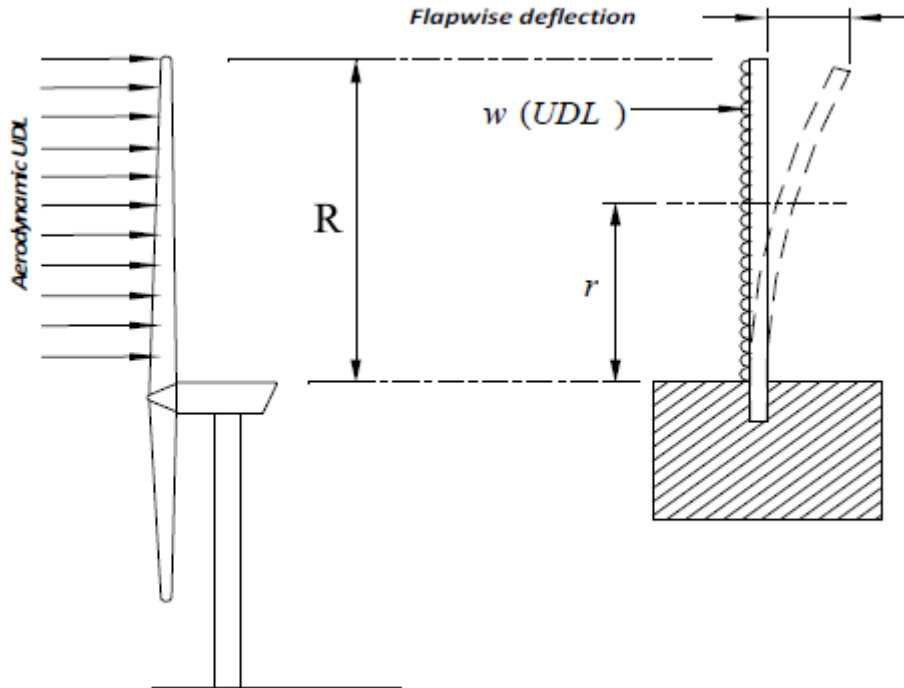


Figure 3.3: The blade modelled as a cantilever beam with uniformly distributed aerodynamic load. [11]

surrounding fluid [14]. In a wind turbine, the airfoil is the cross-section of the wind turbine blades. The airfoil shape is directly related to the aerodynamic performance of the blade.

3.2.1 Defining airfoils

The airfoil is defined by several parameters, collectively determining the shape of the airfoil. A standard airfoil shape can be seen in Figure 3.4. The forward and backward point of the airfoil are the leading and trailing edge, respectively. The leading edge is defined by its radius. The trailing edge angle is defined by the angle between the mean camber line (the line halfway between the top and bottom of the airfoil) and the direction of the trailing edge. The chord c is a straight line between the leading edge and the trailing edge. The thickness is the maximum distance between the top and bottom of the airfoil, perpendicular to the chord line. Finally, the angle of attack α is defined as the angle between the relative velocity of the fluid on the airfoil (U_{rel}) and the chord line. Another parameter of the blade is the span, which is the length of the blade, the length perpendicular to the cross-section.

When the airfoil is positioned in an air flow, the air flows around the airfoil shape, the air stream is deflected downward at the trailing edge of the airfoil. Pushing the air stream downward creates a reactionary force that pushes the airfoil upward, increasing in velocity over the relatively longer convex surface. This results in a lower pressure on that side of the airfoil. Meanwhile, the air velocity over the lower, concave side of the airfoil decreases, resulting in a higher pressure. This difference in pressure creates a force in the upward (relative to the airfoil) direction, this creates lift. These effects and therefore the lift, increase when the angle of attack is increased. In the case of symmetrical airfoils, the airfoil will only generate lift with an angle of attack $\alpha \neq 0$. The lift force is defined to be perpendicular to the direction of the oncoming air flow. The air that flows along the airfoil slows down due to friction with the airfoil surface. This results in friction drag. Another factor contributing to drag is that the pressure distribution over the air flow direction is not uniform. The drag force is defined to be parallel to the air flow direction. Finally, a pitching moment is present, this moment tips the airfoil around an axis perpendicular to the airfoil cross-section. The lift force, drag force and pitching moment act along the chord at a point one quarter chord length ($c/4$) from the leading edge. This point is aptly named the 'quarter chord' [14]. The forces acting on the airfoil are shown in Figure 3.5.

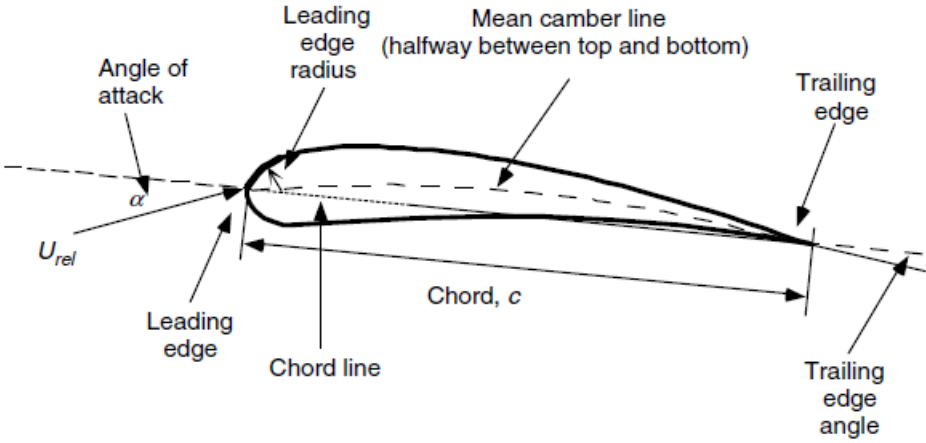


Figure 3.4: Airfoil nomenclature. [14]

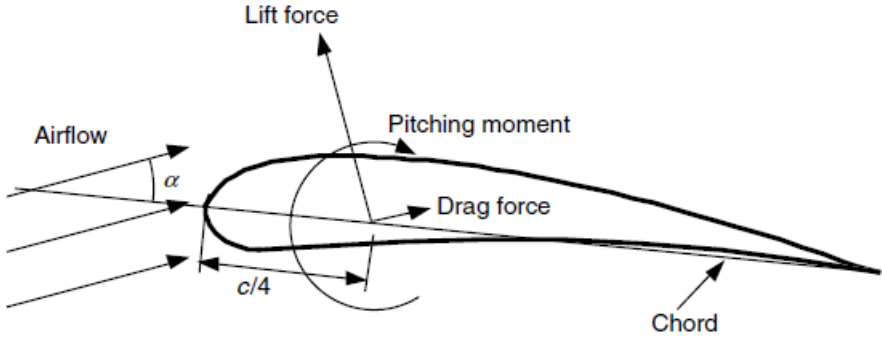


Figure 3.5: Forces and moments on airfoil section. [14]

3.2.2 Airfoil Non-Dimensionalization

To generalise information about airfoil performance a non-dimensionalization is performed to define airfoil characteristics. The most important factor to define flow conditions is the Reynolds number Re . The Reynolds number is defined as:

$$Re = \frac{\rho U l}{\mu} = \frac{\text{Inertial Force}}{\text{Viscous Force}} \quad (3.9)$$

Where ρ is the fluid density, μ is fluid viscosity, U is a characteristic velocity and l is a characteristic length.

Generally, for wind turbines, the characteristic velocity is the relative wind speed U_{rel} and the characteristic length is the chord length c of the airfoil.

To further define the non-dimensional behaviour around an airfoil, lift, drag and moment coefficients can be defined. These coefficients are dependent on the Reynolds number and can be defined 2-dimensionally, meaning an infinite span of the blade and not including end effects, these are designated with a lower case subscript (C_l , C_d , C_m , respectively). Alternatively, 3-dimensional coefficients can be defined, including a finite span length and end effects at the blade end. These are denoted with an upper case subscript (C_L , C_D , C_M , respectively). For wind turbine blade design generally 2-dimensional coefficients, for a range of angles of attack and Reynolds numbers, are used [14].

The 2-dimensional lift coefficient is defined as:

$$C_l = \frac{L/l}{\frac{1}{2}\rho U^2 c} = \frac{\text{Lift force/unit length}}{\text{Dynamic force/unit length}} \quad (3.10)$$

The 2-dimensional drag coefficient is defined as:

$$C_d = \frac{D/l}{\frac{1}{2}\rho U^2 c} = \frac{\text{Drag force/unit length}}{\text{Dynamic force/unit length}} \quad (3.11)$$

The 2-dimensional pitching moment coefficient is defined as:

$$C_m = \frac{M_p/l}{\frac{1}{2}\rho U^2 c^2} = \frac{\text{Pitching moment}}{\text{Dynamic moment}} \quad (3.12)$$

Where L is lift force, D is the drag force and M_p is pitching moment. Furthermore, l is the airfoil span and c the airfoil chord length.

3.3 BEM Theory Blade Design

To determine the airfoil geometry and performance two theories are applied. These are the blade element theory and momentum theory. In momentum theory, an analysis is done of the forces on a control volume based on the conservation of linear and angular momentum. In blade element theory a section of the blade is analyzed with respect to the blade geometry. When these two theories are combined, the blade shape can be related to the power extracted from the wind. This theory is called the Blade Element Momentum (BEM) theory. In this section, both theories are explained, with and without wake rotation. This theory can be used to design a simple wind turbine rotor and is used to explain the workings of the optimisation done by the QBlade program that is applied to this project in section 4.3.

3.3.1 Momentum Theory

The aim in this section is to find expressions for the thrust and torque using linear and angular momentum conservation. First a situation without wake rotation is considered. A control volume with boundaries at the start, the end and at two cross-sections in a stream tube is considered. In this schematic these cross-sections are designated 1-4 and parameters at these cross-sections will be denoted with a subscript. An actuator disc is placed in the stream tube, which represents the turbine. This disc creates a discontinuity in the pressure of the air that flows through it. The flow is assumed to be homogeneous, incompressible and steady state. Furthermore, the disc is assumed to have no frictional drag, the thrust is uniform over the disc the wake is non-rotating and the far upstream and downstream pressures are assumed to be equal. The situation can be seen in Figure 3.6. In this situation the disc is non-rotating. From this figure and using momentum theory, the equations for thrust and power can be derived. The force that the wind exerts on the blades/disc is called the thrust. The full derivation can be found in Appendix A. The expressions for thrust and power included a power C_p and thrust coefficient C_t , which in turn are dependent on the axial induction factor a .

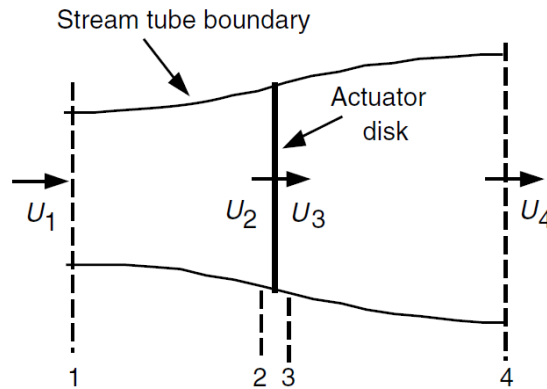


Figure 3.6: Actuator disc model of a wind turbine; U , mean air velocity; 1, 2, 3, and 4 indicate locations. [14]

The axial induction factor a is the fractional decrease in wind velocity between the free stream and the rotor plane:

$$a = \frac{U_1 - U_2}{U_1} \quad (3.13)$$

This axial induction factor is an important characteristic of a wind turbine and is used to express the power and thrust (coefficients). Following the derivation in Appendix 3.3 the power and thrust are:

$$P = \frac{1}{2} \rho v_1^3 A C_p \quad (3.14)$$

$$T = \frac{1}{2} \rho v_1^2 A C_t \quad (3.15)$$

with:

$$C_t = 4a(1 - a) \quad (3.16)$$

$$C_p = 4a(1 - a)^2 \quad (3.17)$$

Optimising the power coefficient C_P is the key to designing an efficient wind turbine. It can be deduced that the optimal value for C_P occurs at $a = 1/3$, resulting in a power coefficient of $C_P = 16/27$, which is known as the Betz limit.

Next, it is noted that wake rotation is present in the flow behind the disc. A new situation is proposed, with a rotating actuator disc. A schematic view of the flow through an horizontal axis turbine with wake rotation is shown in Figure 3.7. The rotation in the wake means that less energy is extracted by the rotor than is expected in the case without wake rotation. It is assumed that the rotation in the wake ω is small compared to the rotation speed of the blades Ω . Because of this, it is assumed that the pressure in the free stream is equal to the pressure in the far wake: $p_1 = p_4$. In this stream, an annular control volume is considered that moves with the angular velocity of the blades. This annular stream tube has a radius r and a thickness of dr and can be seen in Figure 3.8.

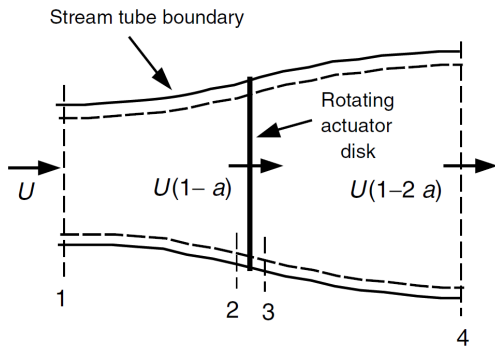


Figure 3.7: Geometry for rotor analysis; U , velocity of undisturbed air; a , induction factor; r , radius. [14]

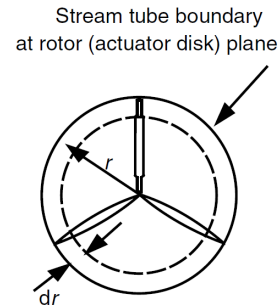


Figure 3.8: Annular stream tube. [14]

When an angular induction factor a' is defined as:

$$a' = \omega/2\Omega \quad (3.18)$$

Following the derivation in Appendix A the equation for thrust force including wake rotation then becomes:

$$dT = 4a'(1 + a')\frac{1}{2}\rho\Omega^2r^22\pi r dr \quad (3.19)$$

When the thrust equation is determined in the same manner, but using the axial induction factor a , the thrust equation then becomes:

$$dT = 4a(1 - a)\frac{1}{2}\rho U^2r^22\pi r dr \quad (3.20)$$

Equating Equations 3.20 and 3.19 gives:

$$\frac{a(1 - a)}{a'(1 + a')} = \frac{\Omega^2r^2}{U^2} = \lambda_r^2 \quad (3.21)$$

Where λ_r is the local speed ratio. The tip speed ratio λ is defined:

$$\lambda = \Omega R/U \quad (3.22)$$

The equation for torque Q is defined using the conservation of angular momentum. The exerted torque on the rotor Q must equal the change in angular momentum of the wake. Using $U_2 = U(1 - a)$ and $a' = \omega/2\Omega$ this becomes:[15]

$$dQ = d\dot{m}(\omega r)(r) = (\rho U_2 2\pi r dr) (\omega r)(r) = 4a'(1 - a) \frac{1}{2} \rho U \Omega r^2 2\pi r dr \quad (3.23)$$

The total torque can be defined as:

$$Q = \frac{1}{4} \rho A D U^2 C_q \quad (3.24)$$

with the torque coefficient C_q :

$$C_q = 4a'(1 - a)\lambda \quad (3.25)$$

3.3.2 Blade Element Theory

Next, blade element theory is considered. For this theory it is assumed that the forces on the blades are determined purely by the lift and drag coefficients of the airfoil. To determine the forces, the blade is divided into N sections with a length of dr . It is assumed that there is no radial flow and therefore no interactions between the sections. The lift force is perpendicular to the relative wind velocity and the drag force is parallel to the relative wind velocity. The relative wind velocity consists of the wind velocity at the rotor and the wind velocity due to rotation of the blade. The rotational component consists of the blade angular velocity and the induced angular velocity. The equation for the rotational component becomes:

$$\Omega r + (\omega/2) r = \Omega r (1 + a') \quad (3.26)$$

First a number of parameters have to be defined. To do this a schematic view of the airfoil is shown, including forces, important angles and geometry parameters. situation can be seen in Figure 3.9.

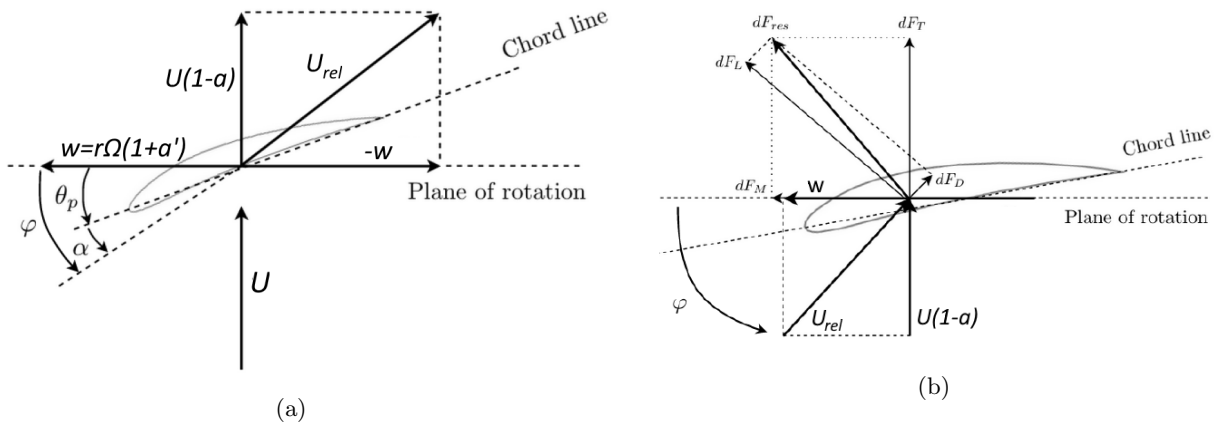


Figure 3.9: Geometric (a) and force (b) parameters working on the airfoil.

In Figure 3.9, $U(1 - a)$ is the wind velocity at the blades, U_{rel} is the relative wind velocity, θ_p is the section pitch angle, also known as the twist, α is the angle of attack (AoA), $\varphi = \theta_p + \alpha$ is the angle of relative wind, dF_L is the lift force, dF_D is the drag force, dF_T is the thrust force and dF_M is the force that induces a moment and drives the rotation of the rotor. Furthermore several equations can be derived from these figures and Equations 3.10 and 3.11 for lift and drag:

$$\varphi = \theta_p + \alpha \quad (3.27)$$

$$\tan \varphi = \frac{U(1-a)}{\Omega r(1+a')} = \frac{(1-a)}{(1+a')\lambda_r} \quad (3.28)$$

$$U_{rel} = U(1-a)/\sin \varphi \quad (3.29)$$

$$dF_L = C_l \frac{1}{2} \rho U_{rel}^2 c dr \quad (3.30)$$

$$dF_D = C_d \frac{1}{2} \rho U_{rel}^2 c dr \quad (3.31)$$

$$dF_T = dF_L \cos \varphi + dF_D \sin \varphi \quad (3.32)$$

$$dF_M = dF_L \sin \varphi - dF_D \cos \varphi \quad (3.33)$$

When B is defined as the number of blades, the thrust force on a section r from the centre can be defined as:

$$dF_T = B \frac{1}{2} \rho U_{rel}^2 (C_l \cos \varphi + C_d \sin \varphi) c dr \quad (3.34)$$

The torsion at a section r from the center is defined:

$$dQ = Br dF_M = B \frac{1}{2} \rho U_{rel}^2 (C_l \sin \varphi - C_d \cos \varphi) cr dr \quad (3.35)$$

3.3.3 Applying BEM Theory to Determine Blade Shape

The BEM theory can be applied to determine the shape of the rotor blade, It uses parts of both momentum and beam element method. Assuming that $C_d = 0$ and there are no tip loss effects (which will be explained later). To describe the optimal relative velocity angle φ and chord length two methods can be applied, resulting in different angles and chord lengths. The first is the Betz optimal chord, which is determined, considering only the Betz limit (best performance at $a = 1/3$) as a factor for the chord length optimization. It assumes no wake rotation, therefore $a' = 0$. Applying these assumptions in the derivation in Appendix A gives the Betz optimal chord length and inflow angle:

$$\varphi_{Betz} = \tan^{-1} \left(\frac{2}{3} \lambda_r \right) \quad (3.36)$$

$$c_{Betz} = \frac{8\pi r}{3BC_l \lambda_r} \sin(\varphi) \quad (3.37)$$

The Betz optimal is a good indication of the ideal chord length and twist, however a more efficient rotor blade can be designed when the wake rotation is taken into account. When this is the case, $a' \neq 0$ and the ideal twist and chord length change. Following the derivation in Appendix A the optimal chord length in case of wake rotation, the Schmitz optimal chord length and inflow angle, are:

$$\varphi_{Schmitz} = \frac{2}{3} \tan^{-1}(1/\lambda_r) \quad (3.38)$$

$$c_{Schmitz} = \frac{1}{B} \frac{16\pi r}{C_l} \sin^2 \left(\frac{1}{3} \tan^{-1} \left(\frac{1}{\lambda_r} \right) \right) \quad (3.39)$$

3.3.4 Tip and Root Loss

These proposed geometry parameters are a good start for designing the rotor blades, however the design is not yet reliable enough. Some effects that are not taken into account such as tip and root loss.

In practice air flows around the tip and root from the lower to the upper surface, due to the difference in pressure. This effect reduces the lift the blade generates and therefore the power. To correct for this loss, a correction factor F is introduced. The proposed correction factor is the one by Prandtl [16] For the tip loss:

$$F_{tip} = \left(\frac{2}{\pi}\right) \cos^{-1} \left[\exp \left(- \left\{ \frac{(B/2) [1 - (r/R)]}{(r/R) \sin \varphi} \right\} \right) \right] \quad (3.40)$$

Where the inverse cosine is in radians (otherwise the first factor becomes $1/90$), F is always between 0 and 1. This tip loss correction factor is added to the equations for thrust and torque 3.20 and 3.23:

$$dT = F_{tip} \rho U^4 a(1-a) \pi r \, dr \quad (3.41)$$

$$dQ = F_{tip} (\rho U^2 2\pi r dr) (\omega r)(r) = 4F a'(1-a) \rho U \pi r^3 \Omega \, dr \quad (3.42)$$

When this change in the torque equation is applied to the derivations for the optimal chord lengths, the result equals:

$$c_{Betz} = F_{tip} \frac{8\pi r}{3BC_1 \lambda_r} \sin(\varphi) \quad (3.43)$$

$$c_{Schmitz} = F_{tip} \frac{1}{B} \frac{16\pi r}{C_1} \sin^2 \left(\frac{\varphi_1}{3} \right) \quad (3.44)$$

A similar equation exists for the root loss which is:

$$F_{root} = \frac{2}{\pi} \cos^{-1} \left[\exp \left(- \left\{ \frac{(B/2) [r - R_{hub}]}{r \sin \varphi} \right\} \right) \right] \quad (3.45)$$

With the newly adapted equations, the chord length reduces to zero at the tip, creating a pointed blade end.

This tip loss effect is taken into account when designing the rotor blade, the root loss effect is not. The root loss is considered less important, because the effect it has on the power output is minimal. The design done by the QBlade program, does not take into account this tip loss or root loss effect when defining the ideal shape of the rotor blades, However, it is capable of simulating the tip loss and root loss effect on rotor performance, i.e. the power coefficient calculated by QBlade, does take into account the tip loss effect. Therefore, it is proposed to use the chord lengths as defined by the above mentioned equations for the design, as it will yield a higher performance of the blade, especially at the tips. QBlade can be used to predict the performance of the blades with and without the tip loss correction factor, however it is not able to change the blade design depending on this factor and does not take tip or root loss into account when designing the ideal blade shape. Taking into account tip and root loss in blade design would result in a blade that has a sharp(er) tip at the end as well as a decreasing chord length at near the root.

3.3.5 Other Effects on Blade Performance

There are more effects that are not taken into account by BEM theory. Such as 3D effects drag effects, effects as a result of a varying Reynolds number these effects are explained below. When different airfoil shapes are used in the blade, this also effects the correctness of the BEM theory performance prediction.

In a 3D scenario it seems that the maximum lift coefficient of an airfoil profile is higher on a rotating blade than on a stationary blade. The reason for this is that the centrifugal forces accelerate the boundary layer in radial direction. Due to this effect, the boundary layer is thinner which in turn delays stall. The radial airflow generates a Coriolis force opposite to the rotational direction of the rotor, opposing the rise in pressure of the profiles suction side, further delaying stall. This effect is called the Himmelskamp effect. Taking this into account means moving the stalled region to higher angles of attack [17][18].

For the blade design, the drag coefficient is assumed to be zero. In practice, this is not true. airfoil drag reduces the power coefficient and must also be taken into account to accurately determine the turbine performance.

Along the blade radius, the Reynolds number is generally not the same. Since airfoil polars are dependent on the Reynolds number, a single drag or lift polar is not enough to determine the behaviour at each section of the blade, because different Reynolds numbers occur [18][19].

Finally, when more than one airfoil is used in different sections of the blade, problems can occur, as in reality the sections do not instantly change shape at their edges. This means that the polars in between sections also experience a jump, resulting in strange jumps in optimal twist angles and chord lengths. To solve this problem, a foil interpolation can be applied to determine the behaviour at the edges of two sections [18].

Chapter 4

Aerodynamic Rotor Design

4.1 Airfoil Selection

To select an applicable airfoil for the situation of a small scale wind turbine, the Reynolds number has to be known. The lift and drag coefficients of an airfoil are dependent on the Reynolds number and have to be optimised for the situation. The Reynolds number around an airfoil is given by Equation 3.9. In this case, the characteristic velocity is the relative wind velocity U_{rel} and the characteristic length is the chord length c . The chord length and the relative wind speed are unknown at this point. However, using the assumption that the relative wind velocity almost equals the absolute wind velocity near the root and that the turbine blades will not have a chord larger than than 10 cm, an estimation can be done for the maximum occurring Reynolds number. Since the wind turbine will be designed for a maximum wind speed of 90 km/h. The maximum Reynolds number then becomes:

$$Re_{max} = \frac{1.208 \cdot 90/3.6 \cdot 0.02}{14,88 \cdot 10^{-6}} \approx 170.000 \quad (4.1)$$

However, in reality the Reynolds numbers will be even lower (e.g. below 50.000 for $c = 5$ cm and $U = 40$ km/h). These are relatively low numbers. therefore, an airfoil is to be selected that is applicable at low Reynolds numbers. To this end, the database of empirical data by M.S. Selig [20] is used. This database contains the data of airfoil experiments for airfoils in low Reynolds numbers. In this case, the data on power and lift coefficients is used. For the wind turbine it is desirable to use airfoils with high lift an low drag at low Reynolds numbers. Furthermore, since the wind turbine will have an adaptable pitch, it is also desired to have high lift and low drag for a large range of angles of attack. For wind turbines at low Reynolds numbers, Selig suggests a range of airfoils, which can be seen in Figure 4.1. For the airfoil selection, the performances of these airfoils will be compared. The Selig Database [20] provides lift over drag graphs for all the selected airfoils. These graphs can be found in Appendix B.

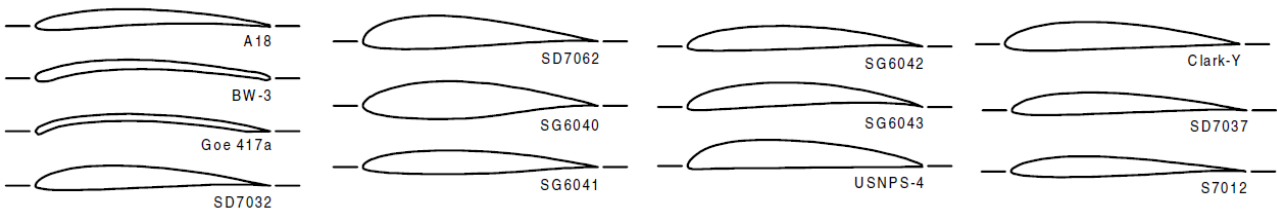


Figure 4.1: AirFoil type and shapes suggested for use in small wind turbines. [20]

In these graphs, some are described to have a boundary layer trip. In general wind turbine application dirt and weathering causes roughness on the blade surface. This roughness acts as a boundary layer trip, it trips the flow around the blade from laminar to turbulent flow. This can have adverse effects on blade performance, however the fuller velocity profile of the turbulent boundary layer can allow the flow to sustain the adverse pressure gradient without separating, preventing laminar separation. To emulate this effect of 'dirty blades' a boundary layer trip in the form of zig-zag tape can be added to the leading edge of the airfoil profile. In many airfoil performance tests this is done. This is the reason why some of the lift over drag graphs in Appendix B contain the mention of 'Zig-Zag Type C', this is the aforementioned trip tape. For some of the airfoils only the

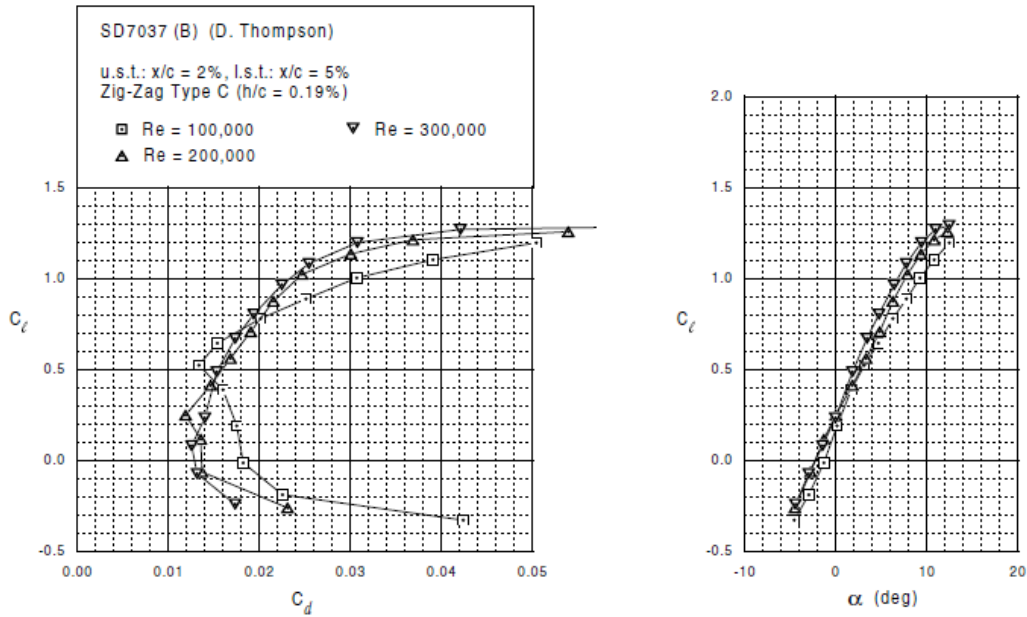


Figure 4.2: lift and drag for various AoA for the tripped SD7037 airfoil. [20]

tripped data was available in the Selig database [20]. In the case of the to be designed wind turbine, dirt will not be an issue, as the wind turbine will be applied in clean wind tunnel conditions. However depending on the production method, material choice and finishing possibilities early laminar-turbulent transition due to surface roughness could be an occurring phenomenon. The performance of each 'clean' blade will be considered for the airfoil comparison, unless no such data is available.

It can be seen that most of the airfoils suggested, perform quite poorly at Reynolds numbers around 100.000. These airfoils have relatively high drag coefficients for these low Reynolds numbers. However, airfoil types SD7032 and SD7037 have a reasonably low drag coefficient for a relatively wide range of angles of attack at low Reynolds numbers. These airfoils are very similar in performance. The SD7037 is chosen because of it's slightly better (lower drag) performance at low angles of attack. For this airfoil both the tripped and smooth flow lift over drag diagrams are available. Since it is impossible at this point to predict if laminar separation will occur on the finished smooth blade, the performance of the tripped situation will be assumed, as it is possible to add trip tape to the finished design if the performance deviates too much from the predicted behaviour. The chosen airfoil will therefore be characterised by the behaviour in Figure 4.2.

4.2 Preliminary Blade Design Using BEM Theory

4.2.1 Blade geometry

Using BEM theory in combination with empirical performance data and a set tip speed ratio, it is theoretically possible to determine the optimal blade twist and chord at every section. The chosen SD7037 airfoil with the known C_l/C_d at an angle of attack $\alpha = 6^\circ$, at a free stream velocity of $U = 11.11$ m/s results in the chord and twist along its radius as in Figure 4.3 and 4.4. The blade twist is the inflow angle minus the chosen angle of attack. The MatLab code used to calculate the BEM theory can be found in Appendix H

$$\theta = \varphi - \alpha \tag{4.2}$$

As can be seen, the different twist angles only vary for a radius length r close to the root of the blade, only for small values of r the Schmitz and Betz optimal twist angle are significantly different. The chord length shows a more distinctive difference between both methods along the radius, however these also converge as they approach the tip at $r = 0.25$ m. The plot also contains a linear approximation of the Schmitz chord length, which is used in one of the concepts in Section 4.4.3.

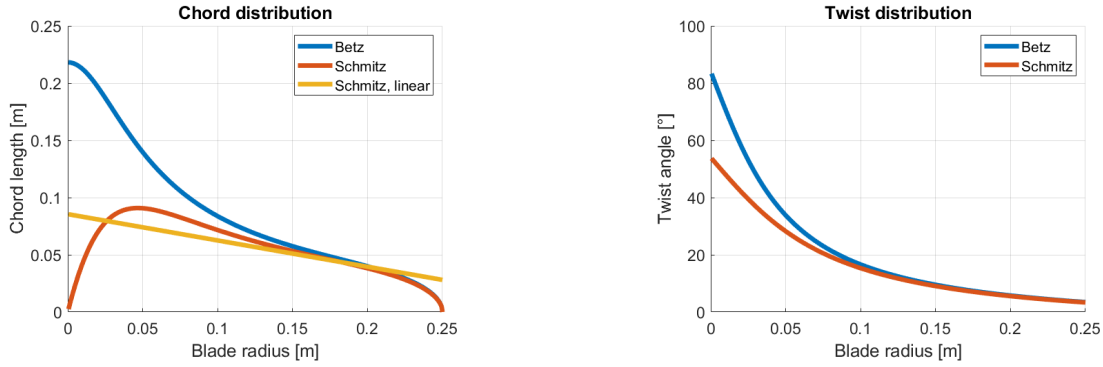


Figure 4.3: Chord length vs the radius for the proposed SD7037 airfoil at a wind speed of 40 km/h, $\alpha = 6$. Figure 4.4: twist angle vs the radius for the proposed SD7037 airfoil at a wind speed of 40 km/h, $\alpha = 6$.

4.2.2 Performance Prediction

Blade Forces

Using BEM theory, an initial prediction of the rotor performance can be made. This includes the forces working on each blade and the resulting torque and power output, assuming no mechanical or electrical losses. Firstly, the lift force generated by each infinitely small section of the blade is calculated. According to Figure 4.2 the best performance occurs at around an angle of attack between 4 – 6°. For the design, 6° will be used, because here the lift coefficient is highest, which results in a sleeker blade. Here the lift coefficient equals $C_l = 0.8$. From Equation 3.30 the relation between the lift coefficient and the Lift force can be determined for an infinitely small blade section. This equation can be rewritten to:

$$dF_L = 1/2\rho U_{rel}^2 C_l dA \tag{4.3}$$

Where: Here dF_L is the lift force on an infinitely small blade element, $dA = cdr$ is the surface of the infinitely small blade element.

The same can be done for the drag force. In the graph in Figure 4.2 the corresponding C_d of 0.02 can be derived. Using Equation 3.31 the equation for drag force is:

$$dF_D = 1/2\rho U_{rel}^2 C_d dA \tag{4.4}$$

Here dF_D is the drag force on the infinitely small blade element.

Next, from the geometric relations the Equation 3.32 and 3.33 are known giving the equations for the trust force dF_T and the moment driving reaction force dF_M . When the known, C_l and C_d are put in for the variable twist angle values Figure 4.5 is the result for the operating speed of $U_{wind} = 11.11$ m/s and a TSR of 4(a) and for the extreme situations of $U_{wind} = 25$ m/s(b)(Airfoil polar values at $Re = 200.000$. The calculated forces are divided by the element thickness dr to get the Lift force per meter span of each element. The total force working on the blade then is the integral of the force function or the area under the graph. The total forces can be found in Table 4.1. In this calculation the axial induction factor is assumed to be 1/3.

Table 4.1: Forces working on the blade at a wind speed of 11.11 m/s and 25 m/s.

Force	At 11.11 m/s	At 25 m/s
Lift Force (F_L)	3.57 N	18.06 N
Drag Force (F_D)	0.09 N	0.44 N
Thrust Force (F_T)	3.39 N	18.06 N
Moment Force (F_M)	0.96 N	4.86 N

The moment driving force F_M is the force inducing torque on the rotor axle and is responsible for the power output of the wind turbine. The total moment of one blade can be calculated for each element by multiplying the force each element is exerting by the radius at that element as in Equation 4.5. Finally the predicted power generated by the wind turbine in an ideal ($a = 1/3$) situation can be determined using Equation 4.6. For a wind

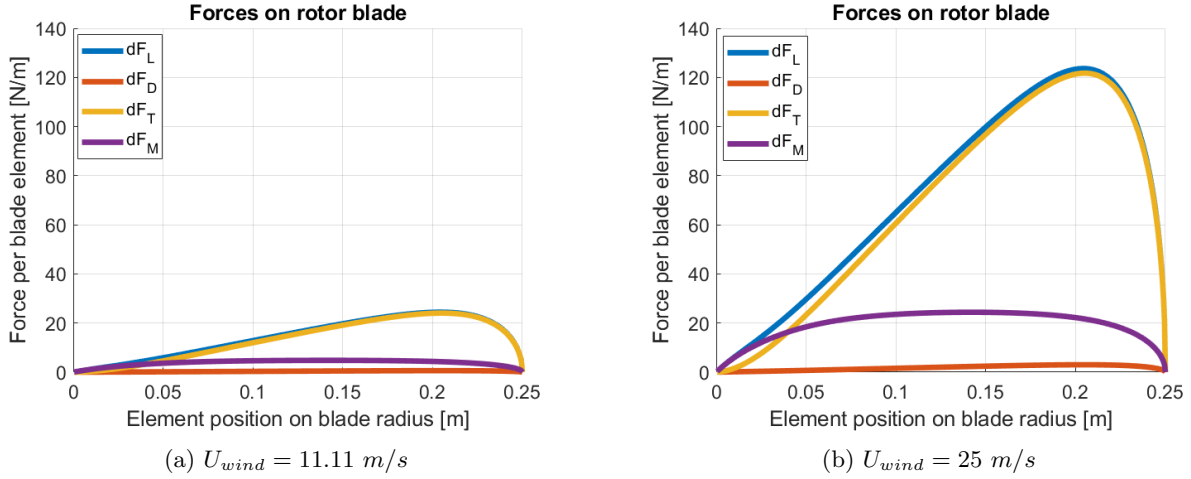


Figure 4.5: Resultant forces on the airfoil at a wind speed of 11.11 m/s (a) and 25 m/s (b) With a TSR of 4, assuming $a = (1/3)$.

speed of 11.11 m/s this results in 22.45 W power output per blade. Giving the total rotor (3 blades) a generated power of 67.36 W at a wind speed of 25 m/s this would be 767.25 W .

$$dM = r dF_M \quad (4.5)$$

$$dP = \Omega dM \quad (4.6)$$

The power coefficient can be determined by dividing the rotor power with the kinetic energy in the airflow passing through the rotor:

$$C_p = \frac{P_{rotor}}{\frac{1}{2} \rho A U_{wind}^3} \quad (4.7)$$

Where A is the area covered by the rotor: πR^2

The power coefficient for the rotor in case of $a = 1/3$ is found to be 0.414. In reality this is lower, due to frictional losses in the wind turbine gearing system, electrical losses in the generator and due to the fact that in reality $a \neq 1/3$. Although, the efficiency losses are hard to predict at this point, a prediction of the actual value for a can be calculated using BEM theory or using QBlade.

4.3 QBlade Design Process

Using the QBlade software wind turbine blades can be designed and their performance simulated and analysed. The QBlade design tool is also an efficient way to combine different airfoil types and create a realistic and aesthetic wind turbine blade. In order to design a blade that is both efficient as well as practically shaped, QBlade is used. Several iterations of wind turbine blades are designed and their performance is predicted using QBlade. The whole design process in QBlade will be explained .

4.3.1 Airfoil and Polar Creation

The first thing to do, is to create the chosen SD7037 airfoil geometry in QBlade. Airfoil geometries and corresponding data files containing the airfoil geometry coordinates can be found online, the *Airfoil Tools*[21] website offers these data sheets and these can be uploaded into QBlade. QBlade also offers a tool to automatically create airfoils using the NACA system. However, since the chosen airfoil is not a NACA foil, the first method is applied, resulting in the airfoil shape that can be seen in Figure 4.6.

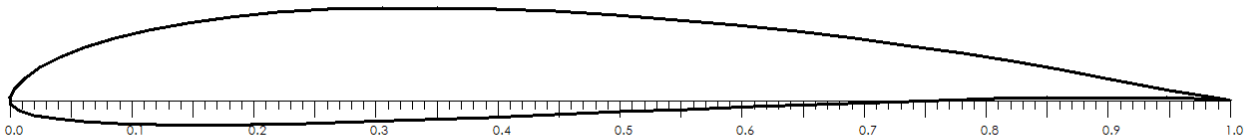


Figure 4.6: The SD7037 airfoil shape.

Once the airfoil shape is uploaded into QBlade, a visual representation of the airfoil is present, however, QBlade does not have any data on the airfoil performance yet. To add this data, an airfoil polar has to be generated or uploaded. The airfoil polar, or drag polar diagram, is representation of the airfoil performance. It is the relationship between an airfoil's generated lift and drag. Usually, this is depicted in a diagram showing lift and drag coefficients of an airfoil at various angles of attack, at a set Reynolds number [22].

QBlade has an option to generate the airfoil polar of a given airfoil geometry numerically. To do this, QBlade uses the implemented *XFOIL Direct Analysis module*. In this module, the flow around the airfoil is simulated to create a polar. The created polar represents the airfoil behaviour along a maximum range of -5 to $+25$ angle of attack (AoA) at a set Reynolds number.[18] However, the experimental data from the SD7037 airfoil profile can be found in Selig's *Summary of Low-Speed Airfoil Data*[20]. To determine the Reynolds number at which the wind turbine rotor will operate, the Reynolds number at the operational wind speed of 11.11 m/s is calculated along the radius of the blade:

$$\text{Re} = \frac{\rho U l}{\mu} \quad (4.8)$$

Where U is a characteristic speed of the fluid, l characteristic length and μ the dynamic viscosity of the fluid. In the case of a wind turbine the relative wind speed U_{rel} is chosen as the characteristic speed, the chord length c as the characteristic length and $\mu = 1.825 \cdot 10^{-5} \text{ kg/ms}$ at 20°C

As is known from Equation A.49, U_{rel} is dependent on the angle of relative wind φ . To calculate the Reynolds number the calculated angle φ_{Betz} and chord length $c_{Schmitz}$ are used. The reason the Betz optimal angle of relative wind is chosen and not the Schmitz optimal, is because the QBlade program itself uses this same angle [18]. To make sure the angles of relative wind that are determined by QBlade are the same as the ones calculated in MATLAB, the same optimal angle and chord lengths are used. Furthermore, the difference between the Betz and Schmitz optimal is considered small enough to neglect the impact on the rotor performance, as the amount of torque generated near the root is relatively small. The resulting graph is shown in Figure 4.7 below. Note that the fact that the Reynolds number is variable is a result of applying the Prandtl tip correction factor and using the Schmitz optimal chord length. If the uncorrected Betz optimal chord is used the result is a constant value of $Re \approx 107.000$.

In this figure, the middle part ($r/R \approx 0.4 - 0.8$ is the part that will generate most of the torque, therefore the airfoil characteristics at this Reynolds number should be used. The Reynolds number in this range averages

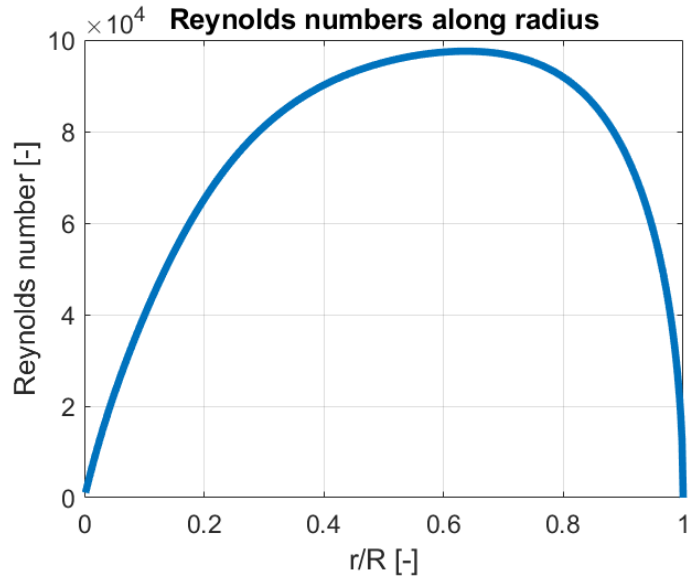


Figure 4.7: The Reynolds numbers along the radius of the blade at $U_{wind} = 11.11 \text{ m/s}$ and $TSR = 4$.

$Re = 95.740$. Because of this, the Selig experimental airfoil data at $Re = 100.000$ will be used and uploaded to QBlade.[20] An XFOIL approximation at $Re = 100.000$ is also created using the XFOIL module in QBlade and the results are compared in Figure 4.8.

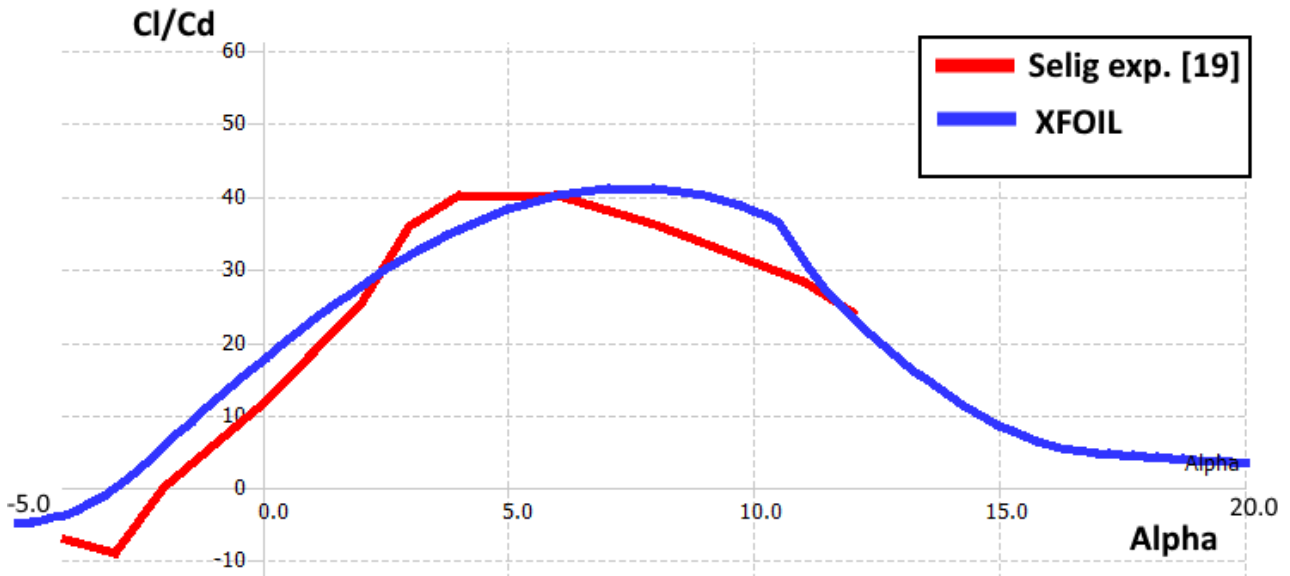


Figure 4.8: Lift over drag ratio vs angle of attack for the SD7037 airfoil at $Re = 100.000$.

In Figure 4.8 the lift over drag ratio (C_l/C_d) versus different angles of attack is considered. The exact data uploaded to QBlade for the experimental polar can be found in Appendix C. In the figure, the differences between the XFOIL prediction and the experimental data by Selig[20] can be seen: The XFOIL prediction seems a more 'optimistic' prediction of the airfoil performance, as it shows a higher lift over drag ratio for nearly all angles of attack. Another difference is the angle of attack at which the highest lift over drag ratio occurs. For the XFOIL prediction, this occurs around an AoA of 8°, Whereas the experimental polar data peaks somewhere between 4 – 6°. The fact that no clear maximum can be determined is because the Selig airfoil data had to be copied to a data file by hand, introducing some (small) inaccuracies. The Selig data also only provides data for certain angles of attack, sometimes introducing large jumps between

measuring points. The proposed design angle of attack is 6° , because the figure suggests the highest lift over drag ratio and because the lift coefficient C_l at this angle is the highest, resulting in a smaller blade (chord length).

To make the polar suitable for 3D modelling and simulation, the behaviour over 360° of pitch angle has to be extrapolated. This can be done in the QBlade 360° module. It offers two methods of extrapolation, namely by Montgomerie [23] and Viterna [24]. The analytical description of both methods will not be discussed, however, the differences observed in QBlade will be reviewed and can be seen in Figure 4.9. Both methods extend the existing empirical polar over a 360° range. However, in QBlade, the Montgomerie extrapolation method assumes a sudden drop of the lift coefficient after the maximum lift in the initial polar. The Viterna method assumes a more gradual decrease of the lift coefficient after its peak. Furthermore, the Montgomerie method assumes low drag at high pitch angles, whilst the Viterna method assumes a relatively high drag coefficient. In QBlade, it is also possible to manually alter the extrapolated lift and drag coefficient diagrams. This was tried but it was found that doing this gives unpredictable results, such as an effect on the optimal blade shape. This results from the fact that the stall point is not defined in the (limited) experimental data from the Selig database and manipulations of the lift and drag diagrams can result in a new optimal lift over drag ratio, at a different angle of attack.

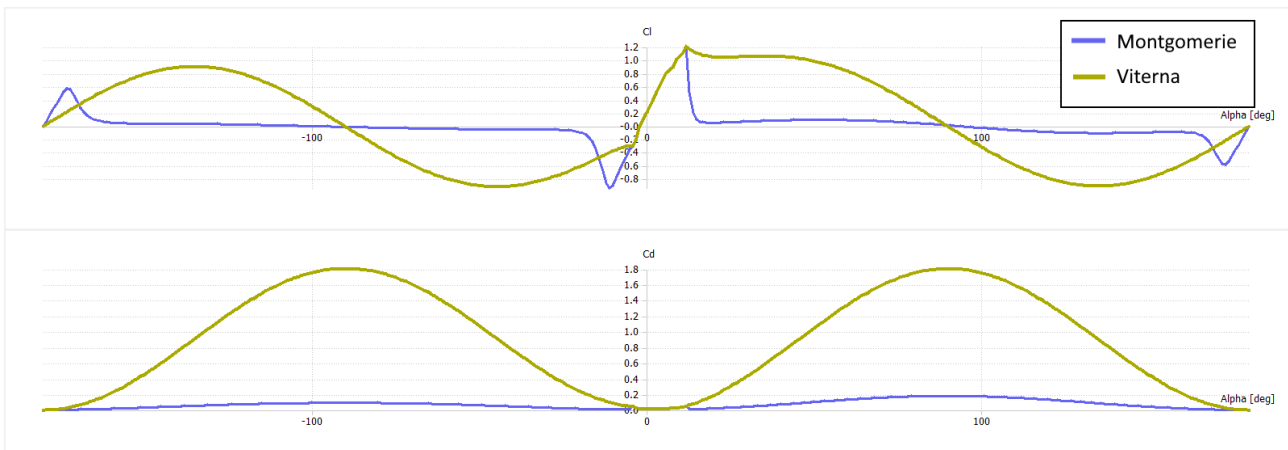


Figure 4.9: The 360° lift(top) and drag(bottom) polar graphs for the SD7037 airfoil at $Re = 100.00$ using the Montgomerie and Viterna extrapolation method.

Both methods are tested and used for the QBlade analysis and it is found that the methods (without manual alterations) do not influence the optimal blade angle and chord length. The effect of the two different methods is mostly noticeable when the blade performance is analysed. Generally, using the Viterna method gives better blade performance for higher pitch angles. This is to be expected, because the lift over drag ratio for higher pitch angles (up to $\alpha \approx 45^\circ$) is higher using the Viterna method. For the simulation results, the Viterna results will be analysed.

4.3.2 QBlade Geometry Design

Once the aerodynamic properties of the chosen airfoil are known, the geometry of the blade can be determined using the QBlade HAWT Rotorblade Design module. This module contains helpful tools to design the rotor blade. First, the hub size and number of blades have to be defined in the module. The hub radius is set to 20 mm , however the final hub design will be determined later, in the detailed design phase. The blade design is then created by defining a number of sections along the blade, as used in the blade element method. Each section has to have its airfoil and corresponding 360° polar defined. The 230 mm blade is defined into 23 sections (of 10 mm each), this makes the total rotor diameter 50 cm following the design criteria. For each section the chosen SD7037 airfoil is chosen. However, at the root a circular foil is applied for design purposes, as it will be easier to fit a circular profile in the hub. Having a circular root will also allow for easier rotation of the blade to adjust the pitch angle. For each section, both the Viterna and Montgomery extrapolated 360° polars are applied. The circular foil at the root has a standard circular foil 360° polar ($C_l = 0$, $C_d = 1.2$, across all angles of attack). Next, the module optimisation tool can be used to determine the ideal chord length and twist angle for each section. Several options are available in QBlade and these can be seen in Figure 4.10.

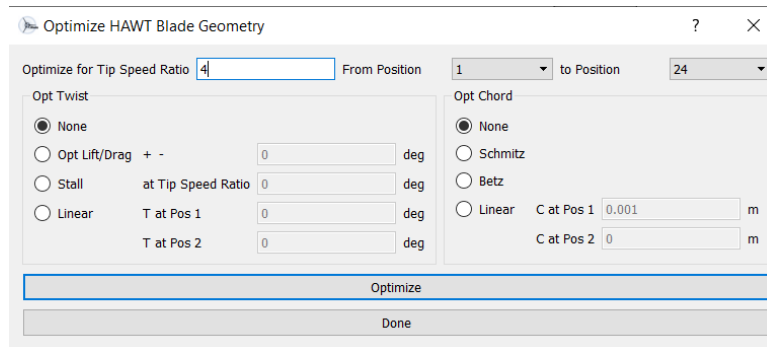
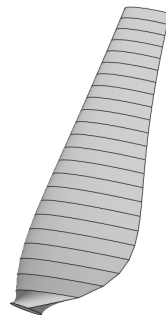


Figure 4.10: The QBlade geometry optimisation menu.

The QBlade geometry optimisation module uses BEM theory to solve the ideal geometry. The theory behind this can be found in Appendix A as well as in the QBlade manual [18]. The module consists of a chord optimisation and twist optimisation part. For both optimisations the design TSR is important for the optimisation process. In this case, the design TSR is 4. The twist can be optimised at the optimal C_l/C_d ratio. In case the AoA with the optimal lift over drag ratio is too extreme, or too close to the stall angle, the module contains an option to change the chosen angle by a set amount of degrees. In the blade design, this option is used. The optimal C_l/C_d occurs at an AoA of 6° . For the angle deviation 0° is used, because there is no need to deviate from this ideal angle of attack, as the stall angle for the SD7037 airfoil is at 12° , or higher. The QBlade module uses the Betz optimal twist as in Equation 3.37 [18]. Other options for optimising the pitch angle are choosing a TSR at which the wind turbine will experience stall. In common wind turbines, steady stall is used as a means to regulate peak power and loads. Airfoils do not stall the same on rotating wings, as they do in non-rotating wind tunnel tests. [25] However, this method of optimisation is not chosen, because in the wind tunnel, wind speeds are regulated and peak power and loads can be prevented by lowering the wind speed and by applying a brake to the system. Finally, an option to manually set a linear transition of twist angle between two of the wind turbine blade sections is present.

The chord optimisation also contains several options. Two of the options are the usage of the Schmitz and Betz optimal chord as explained in Section 3.3, using Equations 3.37 and 3.39, respectively. Note that these optimisations do not contain the Prandtl tip loss correction factor. The applied equations for chord optimisation contains the parameter relative wind speed angle φ . This means that the optimal chord length is dependent on the chosen twist angle. Therefore, it important to either optimise the twist before optimising the chord in QBlade, or to perform both optimisations at the same time. Optimising the chord first will yield incorrect optimal chord values. For the initial QBlade design the Schmitz optimal chord is used. Finally an option for a linear transition of the chord length between two sections is also available.

An initial QBlade design is made, using the AoA at 6° and the Schmitz optimal chord length. The result can be seen in Figure 4.11. It is also interesting to see if the results match the Matlab calculation, therefore the calculated twist and chord distributions are compared to the QBlade result in Figure 4.12.

Figure 4.11: The rotorblade designed with QBlade for $TSR = 4$ with the SD7037 airfoil.

In Figure 4.12 it can be seen that the BEM theory Matlab calculation corresponds with the QBlade design

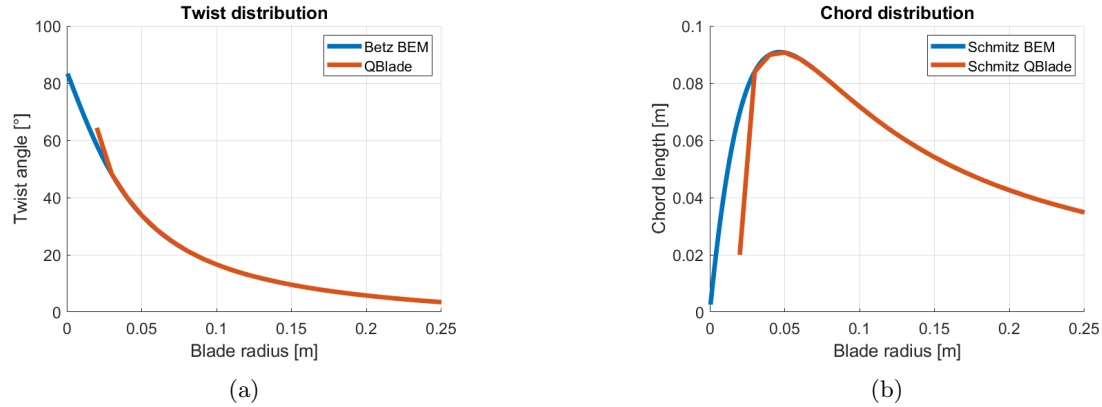


Figure 4.12: Betz optimal twist angle(a) and Schmitz optimal chord length(b), calculated with Matlab and determined by QBlade at $TSR = 4$, $\alpha = 6^\circ$ with the SD7037 airfoil and $U_{wind} = 11.11 \text{ m/s}$.

result. The difference is, that the QBlade design starts at the hub radius at $r = 2 \text{ cm}$. Furthermore, the first section of the QBlade differs in chord and twist, this is because this section does not have the SD7037 airfoil, but the circular root shape with a diameter(=chord length in QBlade) of 2 cm , which results in a different optimal angle.

4.4 Rotorblade concepts

For the final blade design several concepts are proposed. These concepts contain elements from both the Matlab design, as well as the QBlade design. Also, some alterations to reduce the size of the rotor or increase structural integrity are proposed. To make the final choice between the concepts, the concept performance prediction is considered, as well as feasibility and applicability to the hub design. The QBlade HAWT Rotorblade design module is used to visualise each rotor concept. The rotor tables including chord length, twist and airfoil type at each blade section for ever concept and the final concept can be found in Appendix D

4.4.1 Concept 1: The Matlab Design

This concept follows the twist and chord distribution as calculated by the BEM theory Matlab script. It uses the Betz optimal twist angle and the Schmitz optimal chord length at a TSR of 4. The Prandtl tip loss correction factor is applied during the chord length optimisation process. The SD7037 airfoil is applied along the entire radius, with exception of the root section, which has a circular profile. The concept can be seen in Figure 4.13a.

4.4.2 Concept 2: The QBlade Design

This concept follows the twist and chord distribution as determined by QBlade. It uses the Betz optimal twist angle and the Schmitz optimal chord length at a TSR of 4. The Prandtl tip loss correction factor is not applied in the chord optimisation process. The SD7037 airfoil is applied along the entire radius, with exception of the root section, which has a circular profile. The concept can be seen in Figure 4.13b.

4.4.3 Concept 3: The Linear Chord

This concept contains a linear chord progression along the chord progression is created by applying a linear approximation of the Schmitz optimal chord with the tip loss correction factor. The chord along the radius can be seen in Figure 4.3 This is done to make the blade less broad at the root section. This saves material and should make the blade less bulky. Since the largest difference with the Schmitz optimal chord length is near the root, the effect on blade performance should be very small. The SD7037 airfoil is applied along the entire radius, with exception of the root section, which has a circular profile. The concept can be seen in Figure 4.13c.

4.4.4 Concept 4: The Multi-Foil

This concept uses multiple airfoil types along the radius. The aim of using progressively thicker airfoils towards the root is to increase the structural integrity of the blade. Increasing the airfoil thickness near the root makes the blade more resistant to flapwise bending and bending stress. The increased blade thickness also helps to reduce stresses that result from the centrifugal force. This concept uses the Schmitz optimal chord length as calculated for the SD7037 airfoil with Prandtl's tip loss correction factor. For the twist, the Betz optimal twist angle is used for each individual airfoil at each section. The concept uses the SD7037 airfoil for the tip-side half of the blade and NACA foils for the root-side half of the blade. With the help of the Airfoiltools website [21] the NACA 3309 foil was chosen as a base, because its shape is almost identical to the SD7037 airfoil. Using this NACA foil as a base, the thicker airfoils NACA 3312, 3315 and 3318 were used to increase thickness towards the root, with exception of the root section, which has a circular profile. The concept can be seen in Figure 4.13d.

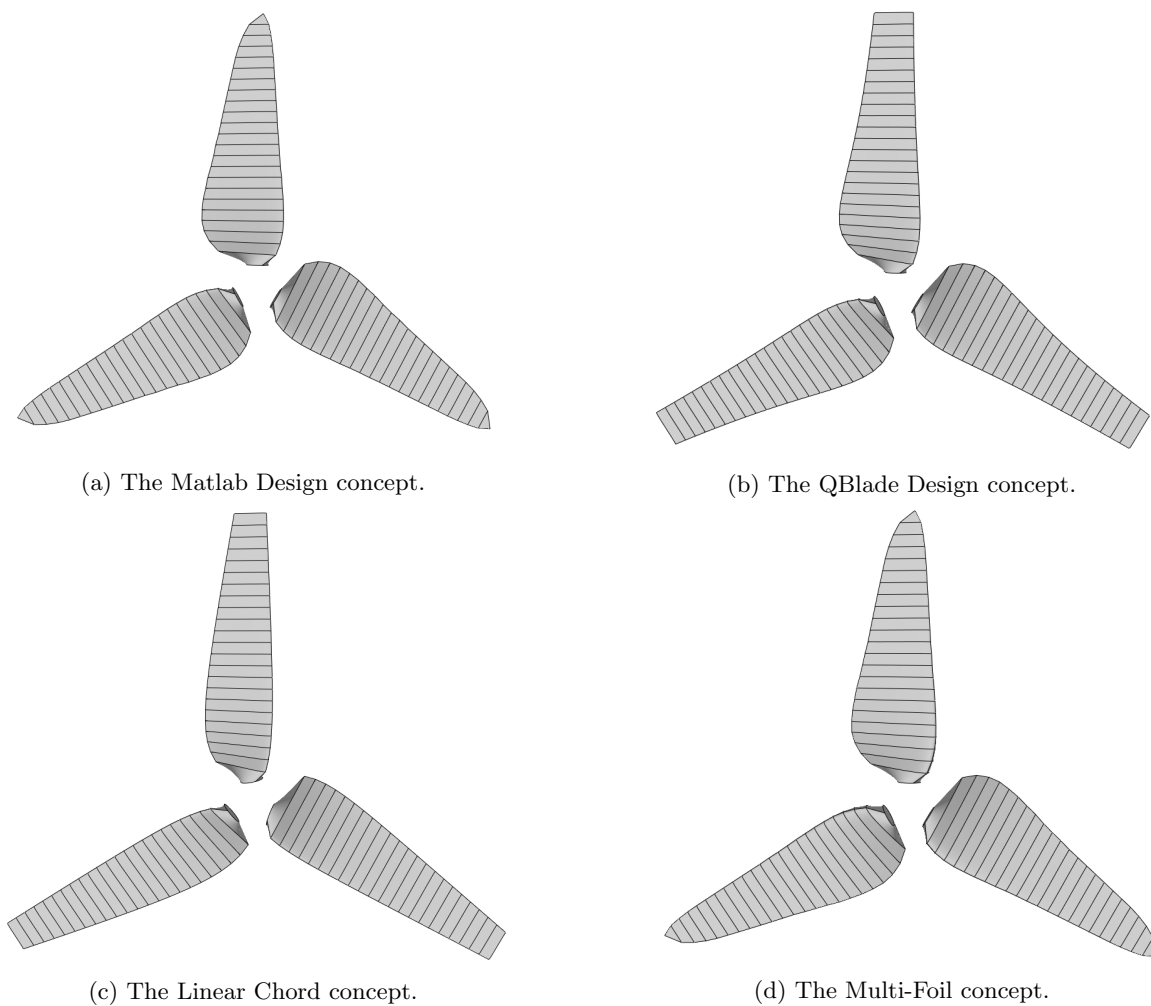


Figure 4.13: Four rotor design concepts.

4.5 Concept Choice

The concept power coefficients are compared in QBlade, to see if the differences in the concepts have big influences on the rotor power output. The Power coefficient vs. TSR plot can be seen in Figure 4.14 and the simulation settings can be found in 4.15. In later figures, the simulation settings are the same, unless mentioned otherwise. Figure 4.14 shows that none of the alterations in the different concept impact the rotor performance a lot. There is no noticeable difference at the optimal operating TSR of 4. For higher TSR, small differences occur, with the multi-foil concept performing the best and the QBlade concept performing the worst. Because the wind turbine will not operate at these higher (> 6) TSR, it is concluded that the impact on rotor performance is minimal. Therefore the concept choice can be based on other reasons.

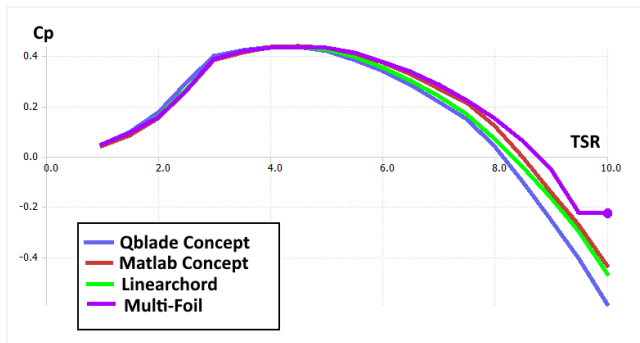


Figure 4.14: Power coefficient values for different TSR for each concept.

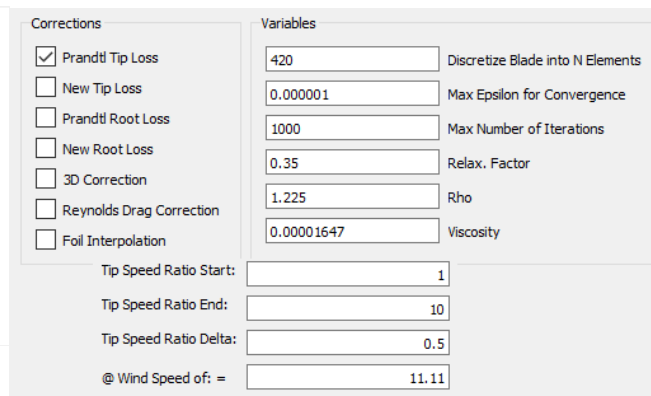


Figure 4.15: QBlade simulation settings for the performed simulation.

Because the centrifugal forces on the blade are influenced by the mass distribution of the rotor, and the weakest part of the blade will most likely be the connecting part to the hub, not the blade itself, it is chosen not to apply different airfoils along the blade radius to limit the stresses at the blade root due to these centrifugal forces. The linear chord adaptation is applied, because it saves space near the hub. This is important, because the blade is twisted backwards near the hub and this is undesirable, because it is possible that the large chord length makes the blade hit the nacelle, if these are too close together. This effect is even more present if the blade is pitched for operation. However, since enough space is available near the nacelle, and this problem can also be compensated by increasing the hub size and length, the linearisation is put slightly closer to the Schmitz optimal chord line. Finally, it is chosen to apply the tip loss correction near the tip of the blade, because it makes the blade perform marginally better at high TSR and there are no real drawbacks to applying it. The final concept can be seen in Figure 4.16 below.

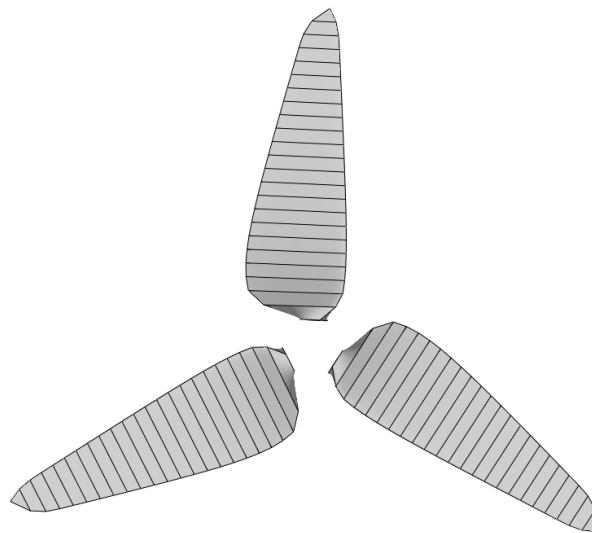


Figure 4.16: The proposed concept for the wind turbine blade design.

Chapter 5

Detailed Design

5.1 Geometry Design

To determine the (local) forces working on the blade as well as be able to select a suitable material and production method, the exact geometry of the blade needs to be designed. The blade geometry is known, however up to this point only a round connecting point and a hub radius of 20 *mm* were assumed. Therefore, three main parts are to be designed: the rotor hub, the rotor-to-blade-connection and the blade root shape. Designing these parts was an iterative process of which only the final result is presented and discussed. In the following sections each design can be found along with an explanation of each part. For each part a SolidWorks model and a technical drawing are made. The drawings can be found in their corresponding appendices.

5.1.1 The Rotor Hub

The rotor hub was designed after a rotor hub of a propeller that was observed during the research. Technical drawings of the rotor hub components can be found in Appendix E. Initially, the rotor hub was proposed to be 20 *mm*. However, it was implied that manufacturing such a small hub would be quite difficult. Therefore, the hub radius was increased to 40 *mm*. Finally, due to the available material being slightly smaller, the hub was redesigned to have a radius of 39.5 *mm*. The hub was designed in two parts that can be screwed together and can be seen in Figure 5.1a. An exploded view is available in Figure 5.1b. The part that has the rounded side and will be used in the upwind direction of the blade will be called the front part and the part behind that, which is more downwind is called the back part. The hub is designed to contain a round base for the blades. A round blade base is necessary in combination with this hub to facilitate pitching the blade in between tests. The 8 *mm* axle that sticks out of the nacelle goes through both parts and is clamped by two set screws that are inserted in the front part of the hub. To ensure that the rotation is transferred well to the axle, the axle is flattened near the end, so that the set screws are pushing down on a flat surface. Although the axle is designed in the nacelle/tower project, the technical drawing is included in Appendix E to get an idea of how the two parts are connected. The two components are attached to each other with three M6 hexagonal countersunk flathead screws. Three screws were used for symmetry, as well as to provide the correct alignment between the two components. The hub has three holes that fit the round bases of the blades. Due to the shape of the holes, the blades are enclosed in the hub during rotation. To also lock the blades from pitching, three M4 set screws are applied from the back up to the larger diameter part of the holes. When tightened, these should lock the pitching rotation of the blades. Finally, the hub component is given a rounded 'nose'. This is not done to increase performance or power output, but for aesthetic reasons, as no evidence could be found that the nose shape has any (significant) influence on the rotor performance.

5.1.2 The Blade Foot

To connect the blade geometry to the hub a special 'foot' was designed that attaches to the blade geometry. It was considered to integrate this foot with the blade, however it was decided to create a separate part due to structural and manufacturing reasons. This decision also gives the freedom to easily change blade shapes in the future. The blade foot can be seen in Figure 5.2a and an exploded view can be seen in 5.2b, the technical drawing can be seen in Appendix E. The blade foot is a simple part that consists of a wide circular base with a diameter of 40 *mm* and a slimmer cylinder with a diameter of 30 *mm* on top. From the top cylinder a slot is removed in which the blade root is placed. The blade is kept in place by an M5 hexagonal countersunk flathead



Figure 5.1: The assembled hub part(a) and an exploded view of all parts in the hub (b).

screw that is inserted into a Heli-Coil that is inserted in the blade root. Two 3 mm guiding pins are also added that ensure correct alignment of the blade in the blade foot. The blade foot with the attached blade can be inserted in the hub part by placing it in the form-closed holes in the hub. when the two hub components are attached to each other with the blade foot in between, the foot (and the blade) are locked in the hub.



Figure 5.2: The assembled blade foot (a) and an exploded view of all parts in the blade foot (b).

5.1.3 The Blade Root

The design of the blade root can be found in Figures 5.3a and 5.3b. The technical drawing of the root section of the blade can be found in E. The blade root is designed to fit inside the blade foot part. This means that the end of the blade has to be a rectangular part. Important for the mounting of the blade is that the angle at which the blade is placed is known. To do this, The square blade root is placed under exactly 40° . This means that to put the blade under the designed angle of attack, the blade root is first twisted in alignment with with the separating line between two hub components and then twisted 40° clockwise from that direction. To aid this, a degree indicator can be applied around the holes in the hub and an arrow-like point is added to the blade root. The blade root contains three holes. Two 3 mm holes for the guiding pins in and one hole to house an M5 Heli-Coil are made in the blade root. The exact size for this hole and details about the Heli-Coil can be found in the Heli-Coil catalogue [26]. As mentioned, the hub size was increased, this means that the blade root also starts later than the initial design. the square root section also has to be attached subtly to the rest of the blade. In the design, the section at $r = 60 \text{ mm}$ marks the start of the blade as designed in QBlade and as is displayed in the final concept rotor blade table in Appendix D.

5.2 Material Choice & Production Method

The material choice and production method are highly dependent on each other. Therefore they are determined together. Each material and production method combination is evaluated on the criteria: cost, feasibility and material properties. For the criteria of feasibility it is preferred that the production processes and materials are available at the Univeristy of Twente, as the preference is not to outsource production, as this could lead to high

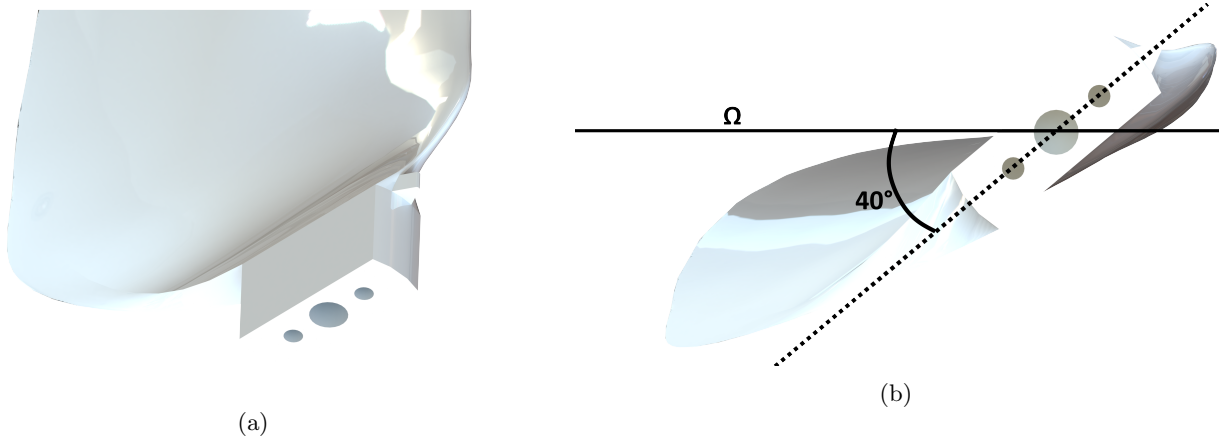


Figure 5.3: The blade root (a) and a bottom view of the blade root (b).

costs.

5.2.1 The Rotor Hub

The rotor hub is a complicated part. The holes that hold the blades are especially difficult to create. Possible production methods for these parts are 3D Printing and milling. The milling can only be done with a mill that has at least three axes of movement. Both of these methods are available at the UT. The rotor hub will be subject to the centrifugal forces working on the blade and the blade foot. Therefore it has to be resilient to stresses (mostly shearing) that work in radial direction. These stresses are dependent on the material and are calculated in Section 5.3.2. Because of this required strength, milling is chosen as a production method, because it can be used to produce a metal hub, which will be stronger than a 3D-printed plastic hub. The material to be milled is chosen to be aluminium. The grade used is Aluminium 6061, as this is readily available at the UT and its material properties are suitable for the application and production method [27]. The finished hub components can be seen in Figure 5.4.

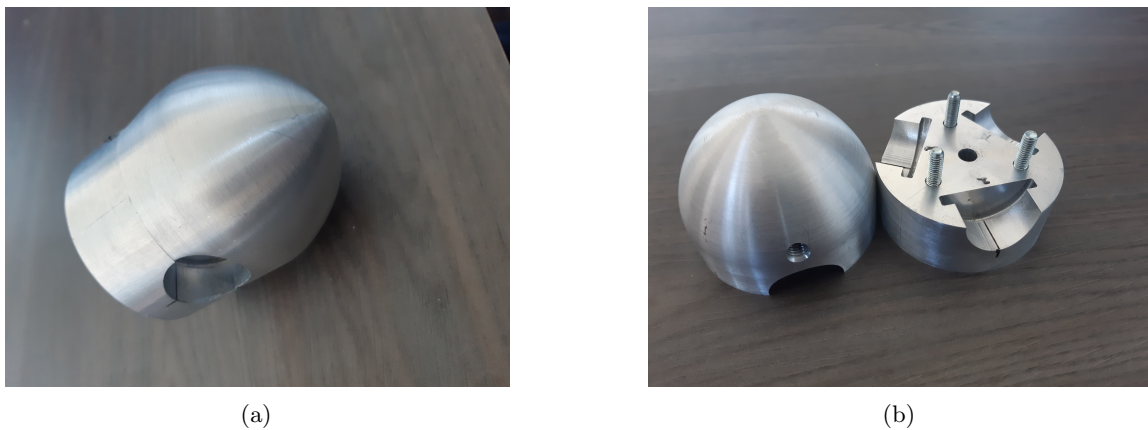


Figure 5.4: The finished rotor hub.

5.2.2 The Blade Foot

The blade foot is a relatively simple component compared to the other components in the rotor. Because of its simplicity, various production methods are available. First the material is chosen. Metal is preferred over a plastic, because this component will also be subject to shearing due to the centrifugal force working on the blade. Aluminium 6061 is again used. The product can be produced by turning on a lathe to create the outer diameters. Afterwards a milling machine is used to remove the slot from the upper cylinder and drill the holes. The blade foot is produced three times, one for each blade. The blade foot can be seen in Figure 5.5.



Figure 5.5: The finished bladed foot.

5.2.3 The Blades

The blades are difficult to make, as they contain double curved edges as well as holes that house a Heli-Coil that has to resist significant stresses. Again the production methods of 3D-printing and milling were considered. The milling production method is considered less optimal, as it is more difficult to do. The milling requires specific mills that are not available at the UT as well as a complicated production process. The milling process would require the blade to be turned over for production, losing the machine's point of reference. The upside of milling is again that metal can be used which makes for a stronger blade. However, using metal will most likely also increase the weight of the blade, increasing centrifugal forces and to a smaller degree edgewise bending stresses. Therefore, the production method of 3D-printing is preferred over milling.

Several 3D-printing methods are available and easily accessible at the UT, as well as outside the UT. The University of Twente offers Selective Laser Sintering (SLS), Stereolithography (SLA) (Another version of this is DLP: Digital Light Processing), Fused Deposition Modeling (FDM) and Binder Jetting Technology (BJ) at its Rapid Prototyping Lab (RPLab) [28]. Out of these methods, the SLA/DLP and SLS printing methods are the most interesting. SLA and DLP are interesting, because the method uses a light source that hardens out a resin. Using a resin instead of a plastic means that the surface of the created product is much smoother. Having a smooth surface i.e. low surface roughness, on the created blade will influence blade performance by delaying premature flow transition to turbulent flow. A downside of SLA is that the printer used can only make relatively small objects ($145 \times 145 \times 175 \text{ mm}^3$). The SLS method uses a laser to sinter a layer of powder. The resulting product has a higher surface roughness and can be less accurate than SLA printing. However the SLS printer at the University of Twente is capable of printing larger objects ($190 \times 240 \times 300 \text{ mm}^3$) [29]. The material used to print in SLA, a photopolymer resin called FLGPCL03, is inferior in strength to the material printed by the SLS method, which is PA 2200, as it has a lower yield strength, as well as a lower tensile modulus.[30][31]. Considering the size of the blade ($r = 210 \text{ mm}$) and the fact that it is possible to apply a finishing to the 3D-printed product, SLS is chosen as a manufacturing method. It is not excluded that SLA might be a suitable method of printing blades if a larger size could be printed.

To confirm the applicability of the SLS printed PA 2200 blades, two tests are done. First, the strength of the material and the proposed Heli-Coil connection are tested and compared to the material specifications in Appendix F. Secondly, a test blade is printed to determine if the 3D SolidWorks model is correct, as well as to assess if the resulting blade printing quality is acceptable.

The first test was performed at the wind tunnel lab in the Westhorst at the UT. A piece of 3D-Printed PA 2200 was tested to determine its resistance to tensile stress. A small piece with a section surface of $22 \times 1.5 \text{ mm}^2$ was subjected to a load up to 85 kg . The setup can be seen in Figure 5.6a and 5.6b. Knowing the section surface and the maximum load that was attached to the test piece, it can be deduced that the maximum tensile stress was $\frac{9.81 \cdot 85}{0.022 \cdot 0.0015} \approx 25.3 \text{ MPa}$, which is lower than the 50 MPa in the material specifications.

Another test was performed to test the strength of the Heli-Coil connection. a piece of 3D-printed PA 2200 was fitted with the same M5 Heli-Coil that is to be applied in the blade construction and an increasing load was applied. The setup can be seen in Figure 5.6c. The Heli-Coil connection was loaded with 120 kg and did not break. After this, no more weight was available. at 120 kg loading, the Heli-Coil connection was subjected to

approximately 8 MPa shear stress and showed no signs breaking. This is the shearing over the outer diameter of the Heli-Coil, at the connection with the PA 2200 material.

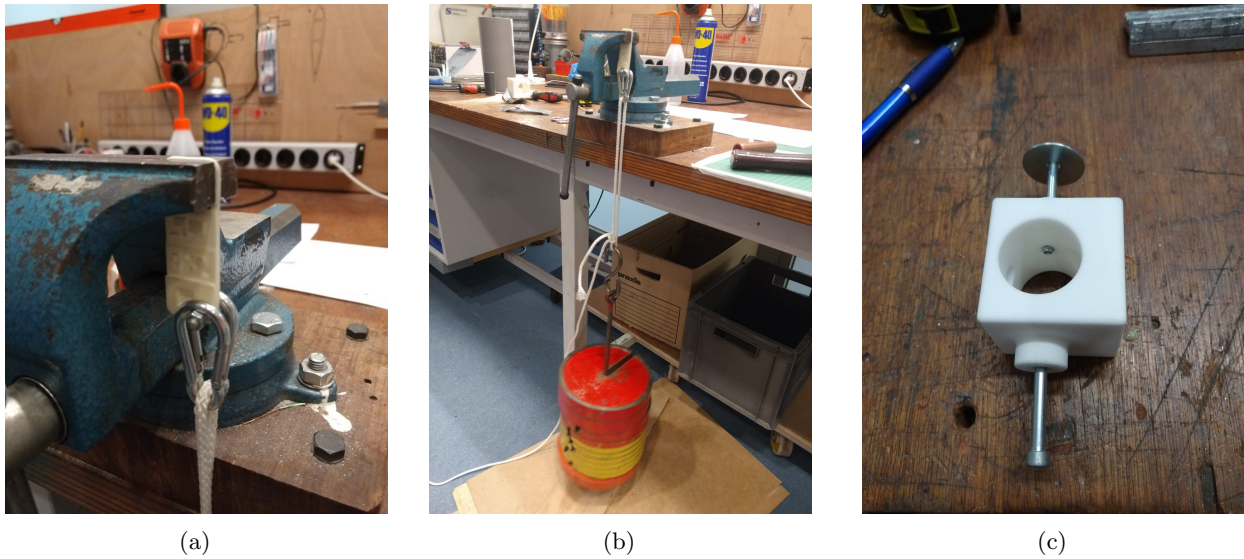


Figure 5.6: The PA 2200 testing strip setup (a), the testing strip with the maximum load of 85 kg (b) and the tested Heli-Coil connections (c).

Next, a test version of the proposed blade design is printed and its quality is judged. The blade prototype can be seen in Figure 5.7. Several problems were noted in this prototype. First, the surface was concluded to be very rough. Therefore, a finishing will be applied to the blades' next iteration. Next, the sharp point on top of the blade and the sharp trailing edge of the used airfoil profiles resulted in a serrated edge, because the SLS printer was not able to print such sharp angles.



Figure 5.7: The first printing test of the designed blade.

To prevent this from happening the SolidWorks model of the blade was altered. The previously used model used airfoil sections that have sharp trailing edges. The new model includes a Trailing Edge gap (TE gap). This means that each profile section has to be redesigned. QBlade has a module that can alter existing airfoil profiles by introducing a TE gap. For each airfoil section a TE gap was introduced such that the TE gap was approximately 0.5 mm . This should solve the problem, because the test blade indicated that the SLS printer was capable of printing a minimal thickness of approximately 0.3 mm . Furthermore, the trailing edge seemed to be wavy. It was found that this waviness was also present in the SolidWorks model and was a result of the loft function that was used to create the blade structure. To prevent this, fewer loft profiles can be used. However, using fewer loft profiles introduces small inaccuracies along the blade radius. It was opted to reduce the amount of loft sections on the linear part of the blade. The comparison of both lofts can be seen in Figure 5.8. Here the reduced amount of lofts, as well as the introduced TE gaps on the profiles can be seen, The new loft was compared with the old one and a very small difference was found between the blades, however this is not deemed significant as the differences everywhere were much smaller than 1 mm .

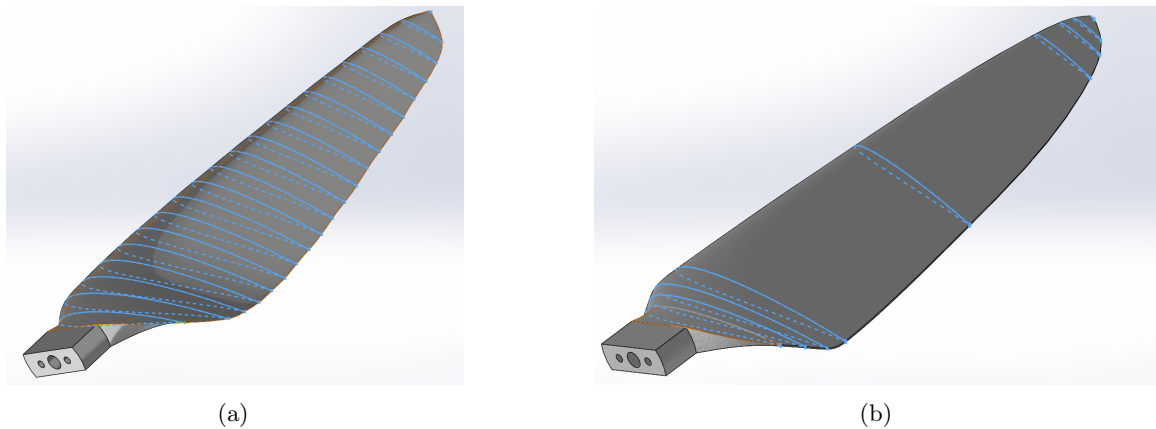


Figure 5.8: The blade lofts before (a) and after (b) reducing the number of lofts.

After these model corrections, three new blades were printed. After printing, a finishing was applied. The blade was painted with a white primer spray paint and then sanded with wetted sandpaper (P800 & P600) several times, after which a red high gloss paint was applied to the tips and finally a clear coating was applied. The result was a smooth blade surface. The final result can be seen in Figure 5.9.



Figure 5.9: One of the finished blades.

5.3 Force Analysis

With the material and detailed geometry known, it is now possible to predict the forces working on the rotor. The global forces and stresses mentioned in Section 3.1 will be determined and the local stresses near weak points and connection points in the blade will also be determined. For each calculation the extreme situation of $U_{wind} = 25 \text{ m/s}$ and $TSR = 4$ is considered. These calculations were considered before the components were created.

5.3.1 Global Forces

Centrifugal Forces

First the centrifugal forces are determined. From the SolidWorks mass properties module the estimated weight of the components can be determined. First the centrifugal forces on the blade are calculated. The blade is estimated to have a mass of ca. 43 g and its centre of mass is at 105.15 mm from the centre of rotation. The

maximum centrifugal force working on the blade then becomes:

$$F_{c,blade} = m\omega^2 r = 0.043 \cdot 400^2 \cdot 0.10515 = 723.4 \text{ N} \quad (5.1)$$

Where $\omega = (U_{wind}TSR)/R = 3819 \text{ RPM}$, however in practice a braking system will prevent the rotor from rotating at a higher speed than 3000 rpm . If this is taken into account $F_{c,blade}$ does not exceed 446 N

Next the centrifugal forces of the blade and foot on the hub are determined. Again using SolidWorks it, is determined that the weight of the two components together is ca. 79 g and the centre of mass is at 70 mm from the centre of rotation. The resulting centrifugal force at $\omega = 3819 \text{ RPM}$ is $F_{c,blade+foot} = 884.8 \text{ N}$ and at the maximum of 3000 RPM , $F_{c,blade+foot} = 545.8 \text{ N}$.

To see if these forces exceed the allowable stresses inside the blade, the local stresses at the weak points are determined in Section 5.3.2.

Edgewise & Flapwise bending

Observing the designed blade and the estimated weight, it can be concluded that the edgewise bending stress will be far less relevant than the flapwise bending stress. This is because the gravitational force on the blade is very small and because the stress is working in a direction which has a higher second moment of area, resulting in lower stresses. For this reason, only the flapwise bending stress is calculated.

The flapwise bending is approached as a problem of a beam bending under an equally divided weight. The maximum force the wind can apply on a flat blade that covers $1/3$ of the rotor area is expressed in the case of the maximum 25 m/s wind speed. The equation for this can be found in 3.7. Assuming $\rho_{air} = 1.208$ and the force divided from $r = 0 \text{ m}$ to $r = 0.25 \text{ m}$. gives $F_{wind} = 24.7 \text{ N}$ for working on one blade. When the blade is assumed to be clamped at $r = 0$ the shear line in 5.10a is relevant to the problem. When integrated, the moment line in 5.10b can be created. The corresponding shear and moment equations are also shown in the figures, in these equations F_0 is the clamping force working opposite the equally divided load at $r = 0$ and M_0 the clamping moment at $r = 0$.

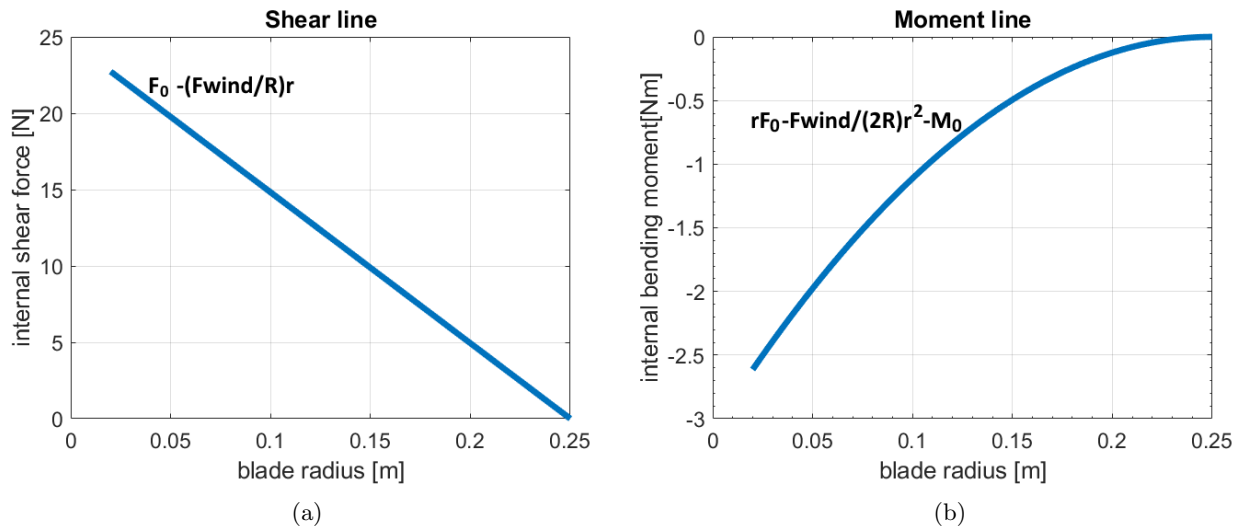


Figure 5.10: The shear line (a) and moment line (b) of the designed blade.

Next, the bending stress along the blade can be determined. To do this, the area moment of inertia (I) of the blade along its radius has to be known. Several ways of approaching are suggested and applied. First, the area moment of inertia of an airfoil of varying size is hard, especially when the element of twist introduced, meaning that the area of the section relative to its bending direction is rotating. Therefore it is suggested to approach the airfoil section as a rectangle, for simplification purposes. The thickness/height of the rectangle (t_I) is assumed to have a thickness of the airfoil maximum thickness: 9.2% of the chord length. (the Schmitz optimal chord length is assumed). The width of the rectangle (c_I) is assumed to be 70% of the Schmitz optimal chord length. For the first determination of I it is assumed that the blade varies in chord length and thickness, but no

twist is introduced. The equation for I at each blade section then becomes:

$$I = \frac{1}{12}c_I t_I^3 \quad (5.2)$$

And the equation for bending stress is:

$$\sigma = \frac{My}{I} \quad (5.3)$$

Where M is the bending moment, $y = \frac{1}{2}t_I$ is the distance from the neutral axis, for the maximum bending stress, this is the point the farthest away from the neutral line. The bending stress along the radius can be seen in Figure 5.11. The maximum bending stress occurs closest the hub and halfway the blade at $r = 0.14 \text{ m}$, assuming the hub radius is 40 mm , the maximum stress equals $\sigma_{max} \approx 3.4 \text{ MPa}$,

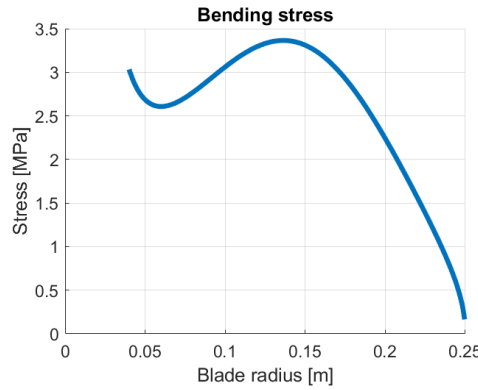


Figure 5.11: Bending stress along the radius, ignoring the twist in the blade.

However, in reality, the blade has a twist. This means that the blade is twisted in a direction more resistant to bending, especially towards the root. To take this into account, a new equation for the area moment of inertia is introduced. This takes into account a rotating rectangle.

$$I = \frac{c_I t_I}{12}(t_I^2 \cos^2 \theta + c_I^2 \sin^2 \theta) \quad (5.4)$$

Where θ is the blade twist angle. Also the point of maximum stress, farthest away from the neutral axis is redefined as:

$$y = (t_I \cos \theta + c_I \sin \theta)/2 \quad (5.5)$$

The resulting stress over the blade radius can be seen in Figure 5.12. In the new, more realistic, situation, no more stress peak occurs near the root, as a higher area moment of inertia results in lower stresses. The stress peak occurs at $r = 0.165 \text{ m}$ and is lower, ca. 3 MPa .

The calculated stressed do not reach the maximum allowable stress determined in the performed test, or the tensile strength defined in the PA 2200 material properties in Appendix F. Therefore it is considered safe to assume that the blade will resist the bending stress during operation. Another effect to be considered is the bending deflection of the blade. To determine this a test was done. The test blade was loaded with 2 kg weight across its length. The setup can be seen in Figure 5.13. It must be noted that this setup loads the blade in its weakest direction, therefore the deflection is most likely higher than during operation. However, as can be seen in the figure, the deflection at the point is quite significant. Although the blade did not show any signs of breaking under the weight, the blade was bent substantially. The bending at the tip approached 20 mm . Although the bending of the blade might affect the performance of the rotor, the most important factor is safety. Since the deflection of the blade does not pose a threat to the operation safety of the wind turbine (whereas, the breaking of the blade does), it is considered acceptable, if the tower clearance (the distance between the blades and the tower itself) is larger than this 20 mm . If the clearance is smaller than this, the blades might hit the tower during operation, resulting in a hazardous situation. Most likely this would also mean the that one or several parts in the turbine would break. In the tower design, this clearance will be applied to ensure operation safety.

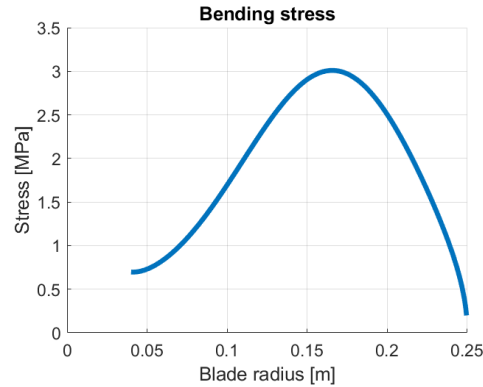


Figure 5.12: Bending stress along the radius, including the twist in the blade.

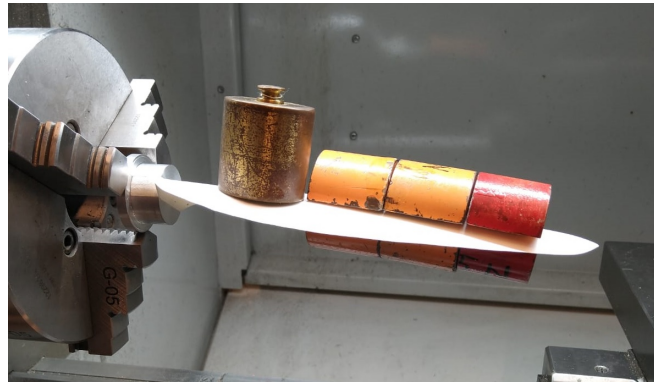


Figure 5.13: The testblade with a 2 kg divided load

SolidWorks stress analysis

Finally, a SolidWorks stress analysis is done on the model of the blade. Both the centrifugal force and the flapwise divided force are modelled at the same time and the effect on stress in the blade and displacement is simulated. In the SolidWorks simulation, the end of the blade root at $r = 60 \text{ mm}$ is given a fixed geometry fixture, which is the equivalent of a clamped end of the blade. Next, the centrifugal force is added, a 723.4 N force is added working over the entire blade surface in radial direction. The wind force or flapwise force is added as a 24.7 N force working over the blade surface in axial direction. The result in Figure 5.14a shows the stress (von Mises) distribution in the blade, as well as the displacement in the blade. According to this simulation, the stress in the blade is acceptable throughout the blade. and even local maximums (ca. 22 MPa) do not exceed even 50% of the tensile strength according to the material properties in Appendix F. As predicted, the displacement is quite large for this load case. According to the SolidWorks simulations results in Figure 5.14b the tip is estimated to have a displacement of ca. 1 cm , Which is less than the displacement from the empirical loading test, however this is to be expected, as the loading in the simulation is from a direction in which the blade is more stiff and because the centrifugal force partly prevents the blade from displacing too much in axial direction, reducing the total displacement at the tip (and throughout the blade).

5.3.2 Local Forces

For the local force analysis several weak points of the rotor construction are examined and the effect of the most prominent force(s) working on each weak point is examined and calculated. These weak points include the connection between the blade foot and hub, the screw connecting the blade foot and the blade and local stresses in the blade root.

Bladefoot connection

The blade foot inside the hub is subject to shearing due to the centrifugal force pulling the blade outward. The thinnest and weakest part where this occurs is at the bottom of the foot where the blade foot 40 mm cylinder

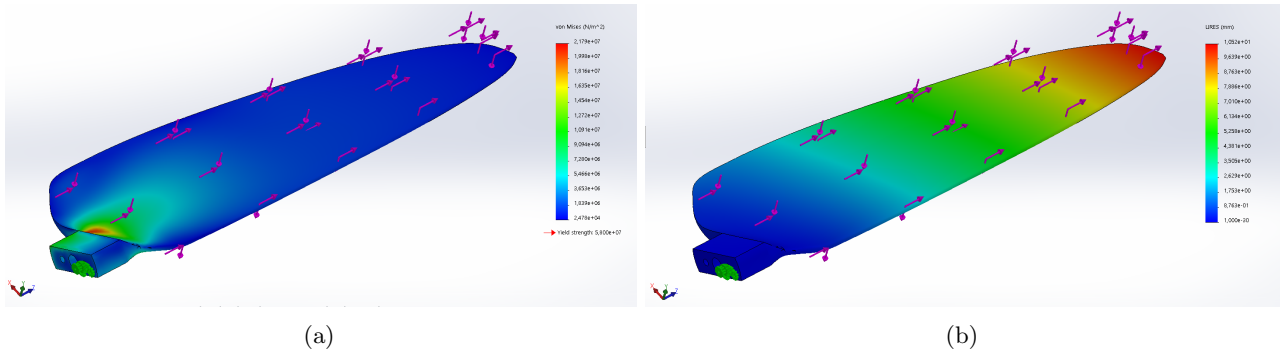


Figure 5.14: The Von Mises Stress (a) and displacement (b) as predicted by SolidWorks under the predicted centrifugal and wind force.

experiences shearing due to the centrifugal force. The situation can be seen in Figure 5.15, in this figure, the shearing occurs along the blue line. To determine the shearing stress, it is assumed that the centrifugal force is the only force contributing to the shearing and that the shearing occurs equally over the entire inner diameter of $30/mm$. The area is equal to the circumference times the height of the 40 mm cylinder, which is 5 mm , the shearing stress is:

$$\tau = \frac{F_{c,blade+foot}}{\pi D_{foot} h_{foot}} = \frac{884.8}{\pi \cdot 0.03 \cdot 0.005} \approx 1.88\text{ MPa} \quad (5.6)$$

This stress is well below the tensile strength of the material, which is 276 MPa [27]

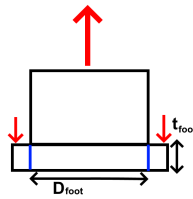


Figure 5.15: Schematic view of the location of shearing in the blade foot.

Heli-Coil screw connection

The next weak point that is examined, is the Heli-Coil screw connection in the blade. The testing of the Heli-Coil connection in the printed material determined that this connection can withstand very high loads. A 7.5 mm long Heli-Coil with an outside diameter of 6.25 mm was used [26]. Again it was assumed that the centrifugal force is the main force causing shearing in the material. Equation 5.6 was again applied, using the centrifugal force caused by the blade ($F_{c,blade} = 723.4\text{ N}$). The resulting shear stress at the Heli-Coil connection with the PA2200 material equals approximately 4.9 MPa , well below the maximum tested 8 MPa .

Blade root

The stresses in the blade were already determined using SolidWorks, However another calculation is done for the tensile strength of the part of the blade with the lowest surface area under the centrifugal force of the blade. The part of the blade with the lowest surface area (not including the tip, as the centrifugal force goes to 0 towards the tip) is the blade root connection itself with a surface area of ca. 252 mm^2 . Calculating the tensile stress in this area gives:

$$\sigma = \frac{F_{c,blade}}{A} = \frac{723.4}{252 \cdot 10^{-6}} \approx 2.87\text{ MPa} \quad (5.7)$$

This tensile stress is acceptable and not close to the PA 2200 tensile strength given in Appendix F or the lower ultimate tensile strength determined experimentally of 25.3 MPa .

5.4 Performance Predictions

The preliminary Matlab predictions assume an ideal situation where $a = 1/3$, however in reality this is not true. To predict the actual behaviour of the rotor at various wind speeds, TSRs and blade pitches, QBlade can be used to make a more accurate prediction of the expected rotor performance. Although a Matlab script was created and included in Appendix I, the correctness and comparison of BEM theory with QBlade results has already been researched by Thomas De Lange and was found to be rather good, where differences arise mostly due to differences in correction models used or the application of complex code [32]. The correctness of the QBlade predictions with real experiments is something that can be researched with this thesis. QBlade predictions are verified with the designed turbine, which gives insight into QBlades accuracy, as well as the accuracy of BEM theory as a tool to predict wind turbine behaviour.

The proposed wind turbine design includes sensors to measure rotor torque, RPM and thrust force. It also generates electricity by using a generator of which the electric resistance can be tweaked for optimal rotor performance (by keeping the wind turbine at its optimal TSR). The wind turbine in the wind tunnel can operate at different wind speeds (0 – 25 m/s), rotate the blades to adapt the blade pitch and adapt its operating TSR by reducing or increasing the resistance in the generator. These settings can be used to keep the wind turbine at its optimal TSR, but also to test the effects of these variables on rotor performance.

It is proposed to review the thrust, RPM and torque and therefore indirectly the power (coefficient) output from the wind turbine at different TSRs, pitch angles and wind speeds of the designed wind turbine and compare these to the QBlade BEM predictions. It is possible to vary all these parameters at the same time in the QBlade Multi-Parameter BEM Simulation module, however since the experiments will be done by only varying one parameter at a time, while keeping the other at standard operating values, the QBlade simulations are performed under the same conditions. These standard operating values are defined as $U_{wind} = 11.11 \text{ m/s}$, $TSR = 4$ and $\theta_{pitch} = 0^\circ$. The aim is to create an understanding of the correctness of QBlade simulations and BEM theory as well as to obtain data on the wind turbine efficiency and its workings.

5.4.1 Simulation Corrections

To determine the difference between the methods (BEM theory, QBlade, experiments), the BEM theory as applied in the Matlab script is applied without any corrections for tip and root loss or for any of the other effects in Section 3.3.5. In QBlade, all applicable corrections are applied to create a result that should be as close to the experimental results as possible. The QBlade correction models for each effect are discussed, but to find out about the exact workings of each correction and their corresponding assumptions and limitations, the reader is referred to the source material.

Tip and Root loss

The tip and root loss can be modeled after Prandtl's model [16]. In this model the helicoidal vortex sheet is modeled as a succession of solid disks moving in the wake. This model was further expanded by Shen. [33] He found that the Prandtl correction overestimates the loads at the tip when compared to experimental data and proposed a new model. A new correction term was added to the normal and thrust force coefficients and can be implemented along with the Prandtl tip and root loss correction. The QBlade simulation module contains a 'New Tip/Root Loss' correction factor which takes into account the corrections by both Prandtl and Shen [16][18][33].

3D Correction

To compensate the 3D effects mentioned in Section 3.3.5, The QBlade guidelines suggest the method developed by Snel et al. [17] Snel et al. developed a semi-empirical formula to correct 2D profile data to be more accurate in 3D situations. This formula only corrects the lift coefficient polar and claims there is no need to modify the drag polar [18].

Reynolds Number Drag Correction

To compensate the varying Reynolds numbers along the radius during operation, the method by Hernandez and Crespo is suggested. [19] A correction of the drag polar is applied, the lift polar remains the same. The drag polar is scaled inversely with the Reynolds number. The suggested correction is very simplistic and might not

completely cover the complex drag behaviour at low Reynolds numbers. The suggested scaling equation is: [18]

$$C_D = C_{D_{ref}} \left(\frac{Re_{ref}}{Re} \right)^{0.2} \quad (5.8)$$

Where Re_{ref} is the Reynolds number for which the polar was computed or determined experimentally.

Foil Interpolation

Since the final design of the wind turbine blades contains only one airfoil type (SD7037), airfoil interpolation is not applied (and therefore not explained). A method for foil interpolation is explained in the QBlade Guidelines [18].

To summarise, the corrections applied in QBlade are: New Tip and Root loss by Shen[33], 3D correction by Snel et al.[17] and Reynolds number drag correction by Hernandez and Crespo[19]. The applied settings in QBlade can be seen in Figure 5.16.

Corrections	Variables
<input type="checkbox"/> Prandtl Tip Loss	<input type="text" value="500"/> Discretize Blade into N Elements
<input checked="" type="checkbox"/> New Tip Loss	<input type="text" value="0.001"/> Max Epsilon for Convergence
<input type="checkbox"/> Prandtl Root Loss	<input type="text" value="1000"/> Max Number of Iterations
<input checked="" type="checkbox"/> New Root Loss	<input type="text" value="0.35"/> Relax. Factor
<input checked="" type="checkbox"/> 3D Correction	<input type="text" value="1.225"/> Rho
<input checked="" type="checkbox"/> Reynolds Drag Correction	<input type="text" value="0.00001647"/> Viscosity
<input type="checkbox"/> Foil Interpolation	

Figure 5.16: The QBlade simulation settings used for the final prediction of the rotor performance.

5.4.2 Varying TSR

First, the effect of varying the TSR is examined. Uncorrected BEM results are compared to the corrected QBlade simulation results. These values will be compared to the results of the experiments performed. In practice, the TSR is varied by increasing or decreasing (electrical) resistance on the generator on the nacelle. The calculations are performed for varying TSR between 1 – 8 at $U_{wind} = 11.11 \text{ km/h}$ and $\theta_{pitch} = 0^\circ$. The results can be seen in Figure 5.17.

When the results are compared it can be seen that for all parameters the uncorrected BEM method has higher values on average. After comparisons were made using the various correction methods separately, it was found that these lower values are mostly the result of tip and root loss corrections, meaning that at the design TSR of 4 over 5% of turbine efficiency is lost due to tip and root losses. Furthermore, the behaviour at high TSRs differs significantly from the uncorrected BEM method, as the corrected model shows a significant increase of the power coefficient after TSR 5. This behaviour is found to be the result of the combination of the (Prandtl) root loss factor combined with the 3D effect correction. This behaviour does not occur if either of these correction factors is not applied, or if they are applied separately. Further investigation indicates that this peak is caused by the iteration process for the axial induction factor. This iteration process includes a relaxation factor (RF) that increases the speed at which convergence for the induction factor occurs [34], by decreasing the amount of iterations necessary. The introduction of this relaxation factor also increases the inaccuracy of the iteration process. To combat this, the RF is reduced to 0.1 in the figure and a result is found that agrees with the MatLab BEM simulation. Finally, a thing to note is that the results for low TSR include relatively high angles of attack, therefore these results are very dependent on the 360° polar extrapolation. The Matlab and QBlade extrapolations are not identical. These angles of attack are not known from the Selig experimental polar data and the result for low TSR is therefore not very reliable.

5.4.3 Varying Blade Pitch Angle

During the blade pitch variation simulation the TSR is kept at 4 and the wind speed is 11.11 m/s . The pitch angle is varied between -10 and $+20$ degrees. The pitch angle is defined in the opposite direction of the twist, meaning: $\theta_{total} = \theta_{twist} - \theta_{pitch}$. In the simulations, the Selig polar is only usable at an AoA of -4° - $+12^\circ$. This means that, at a TSR of 4 (average AoA of 6°), the Selig polar is only usable for pitch angles of -10° - $+6^\circ$.

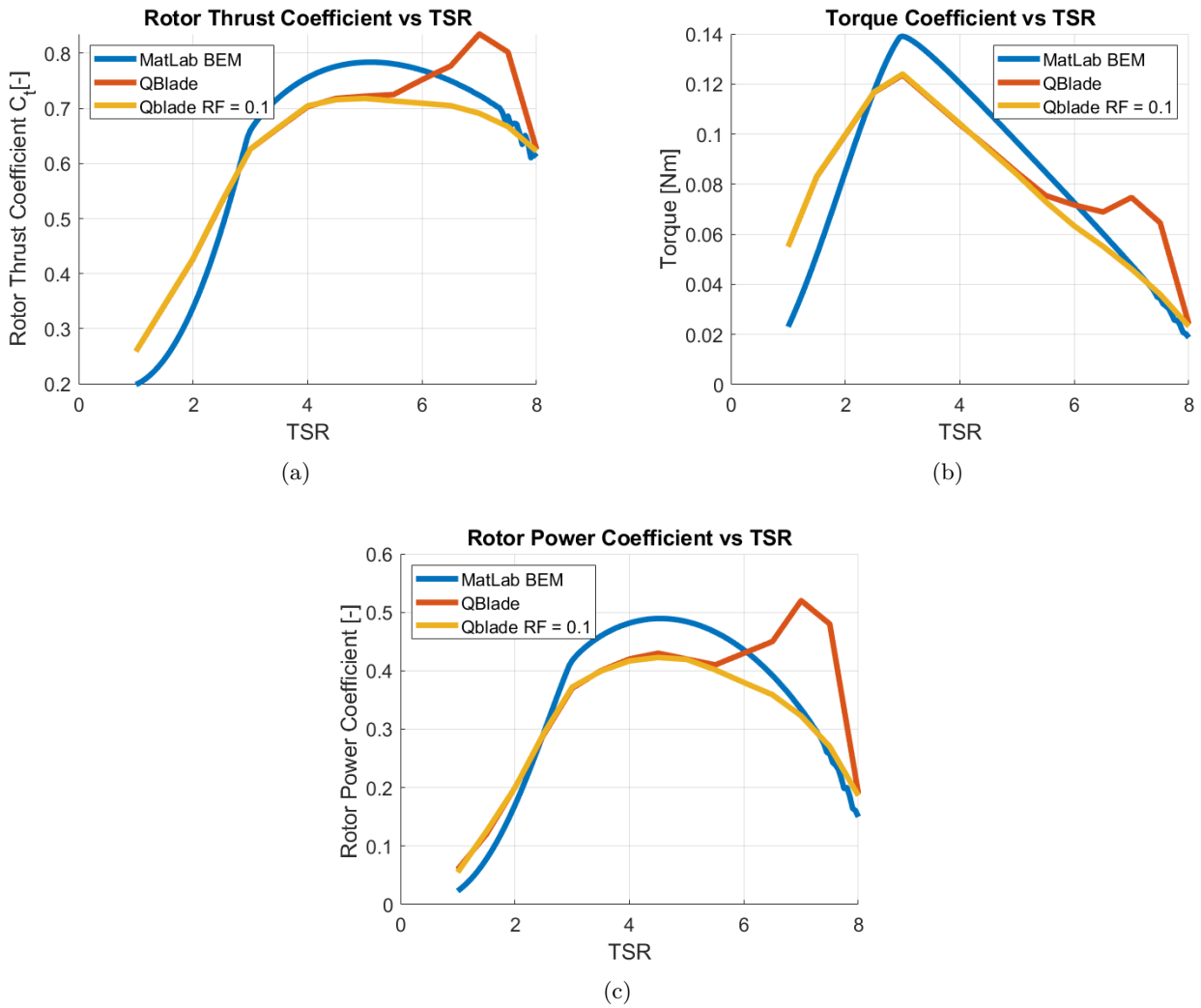


Figure 5.17: The thrust coefficient (a), torque coefficient (b), and power coefficient (c) of the proposed turbine design at a wind speed of 11.11 m/s and a pitch angle of 0° .

Lowering the pitch any further will not generate any lift and will most likely result in no rotation of the turbine. Furthermore, since the pitch is adapted by hand, it is likely that the accuracy of the pitch setting during testing will not be smaller than 1° . Therefore it is suggested to test the wider range of $-10 - +20^\circ$, to find a trend in the behaviour of the tested parameters. However this means that a large range of the tested pitch angles ($+6 - +20^\circ$) is in the extrapolated polar range, meaning the prediction might be inaccurate, however it is a good opportunity to test the correctness of the QBlade 360° polar extrapolation method. The uncorrected BEM and QBlade simulation results can be seen in Figure 5.18

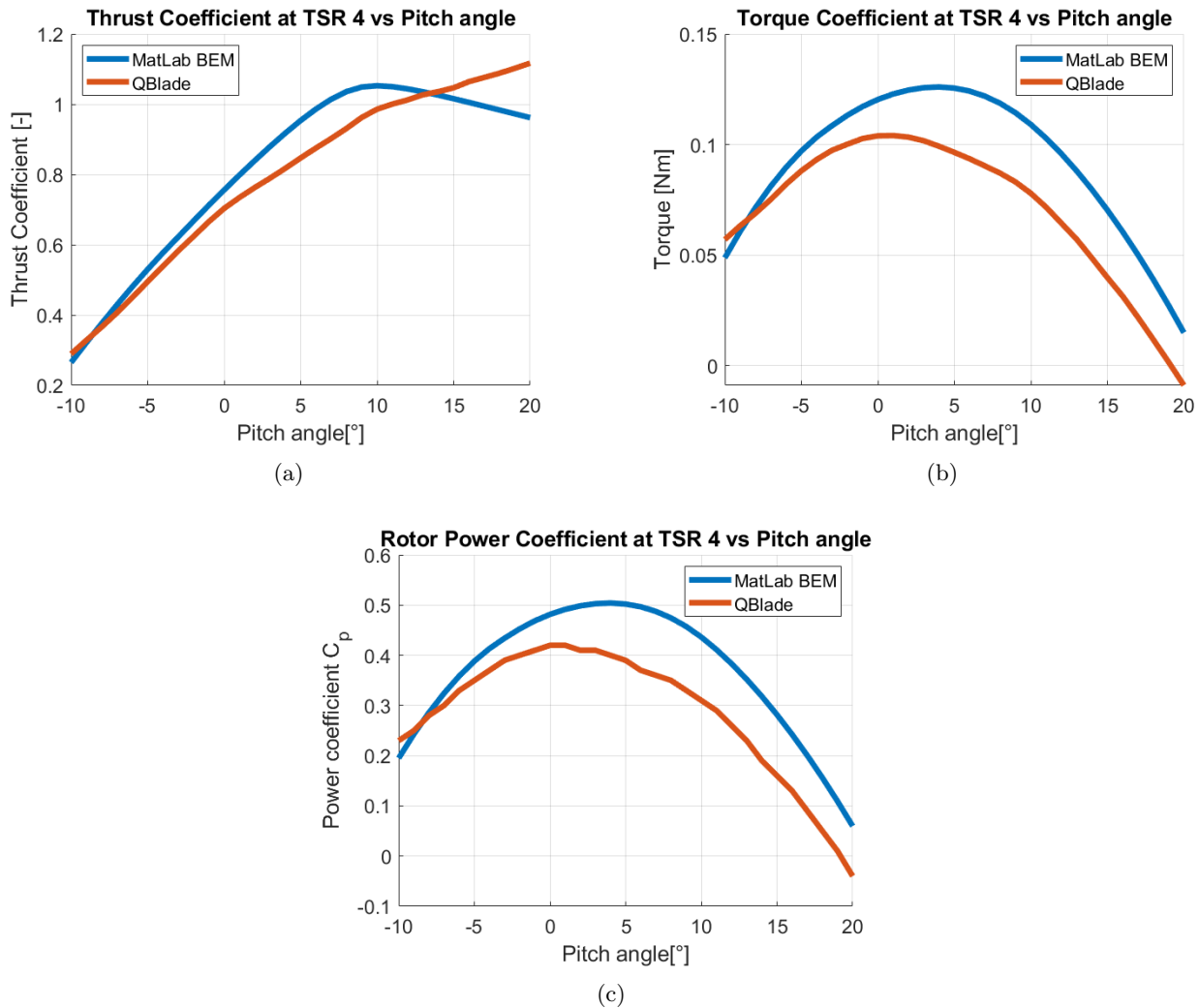


Figure 5.18: The thrust coefficient (a), torque coefficient (b), and power coefficient (c) of the proposed turbine design at TSR 4 and a wind speed of 11.11 m/s .

In the predictions, a difference can again be seen. The QBlade simulation again gives lower results for all three parameters due to the tip and root loss corrections. All other behaviour seems mostly similar, with an exception of the thrust coefficient at high pitch angles. This difference is explained by the different polar extrapolations in both models.

5.4.4 Varying Wind speed

Finally the effect of varying the wind speed on rotor performance is examined. The rotor is tested at TSR 4 and at a pitch angle of 0° . Of interest are the predictions of the power generated by the turbine. Even though the power coefficient is not expected to change when varying the wind velocity and not the TSR, it is interesting to predict the actual power output of the wind turbine, as well as the maximum forces working on the turbine. The result is displayed in Figure 5.19.

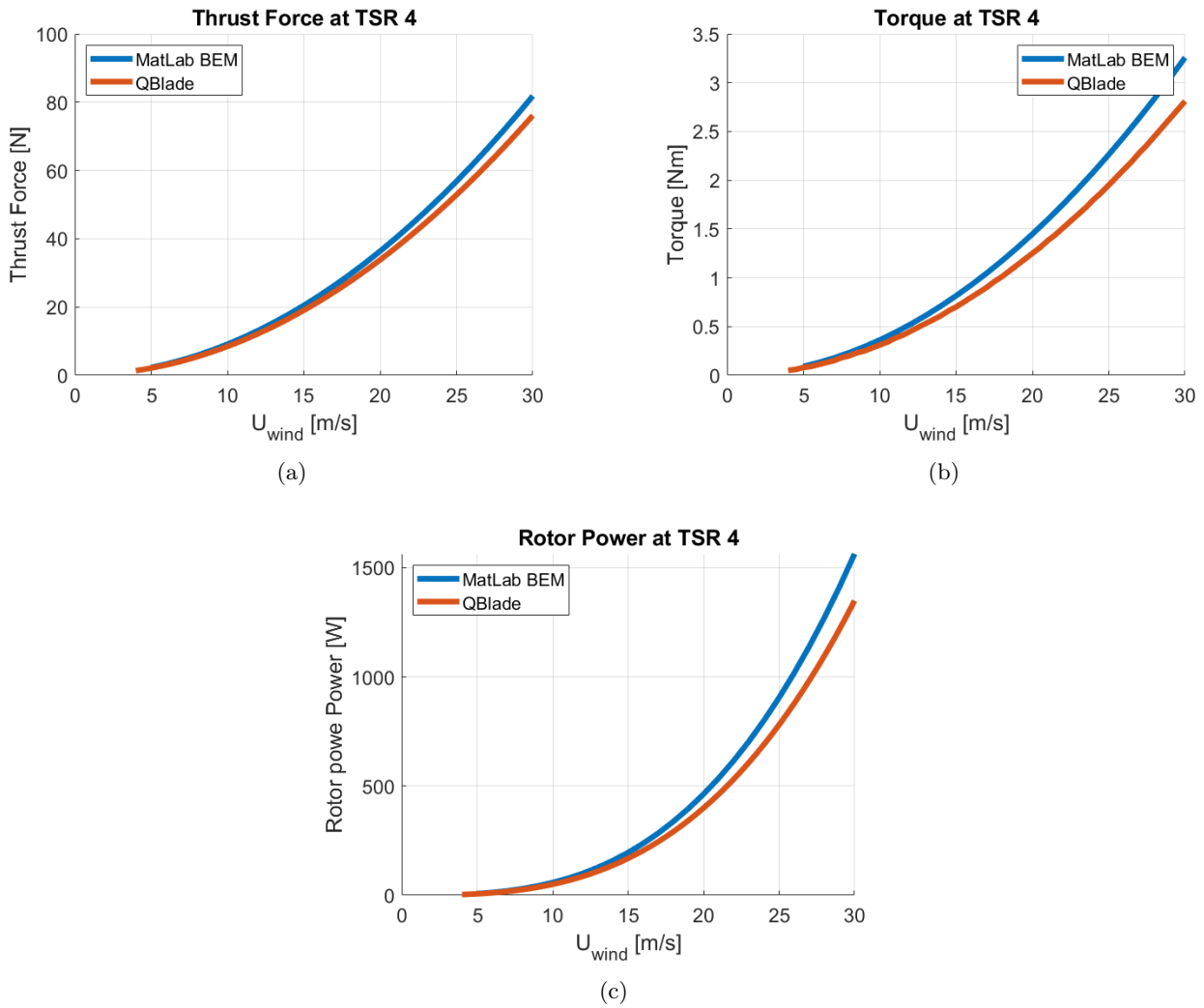


Figure 5.19: The thrust force (a), torque (b), and power (c) of the proposed turbine design at TSR 4 and a pitch angle of 0° .

The prediction results are nearly identical, except for the lower power output due to the tip and root loss corrections. According to QBlade, the maximum power output at $U_{wind} = 11.11 \text{ m/s}$ is ca. 68 W and at the maximum speed of $U_{wind} = 25 \text{ m/s}$ the power output equals ca. 780 W . This is quite a big difference and a suitable generator or a braking system must be applied to prevent the generator from overloading. The maximum torque at $U_{wind} = 35 \text{ m/s}$ equals ca. 2 Nm and the maximum thrust force ca. 55 N . These values are very close to the predicted values for 1 blade and $a = (1/3)$ in Table 4.1 in Section 4.2.2 .

5.5 The Definitive Rotor Assembly

The final rotor assembly can be seen in Figure 5.20. The turbine was named the Twente Instrumented Nacelle wind turbine or for short: *TwIN Turbine*. After the measuring instruments in its nacelle and the fact that it was made at the University of Twente.



Figure 5.20: The assembled rotor.

Chapter 6

Testing and Results

Originally, the turbine was to be tested in the UT aeroacoustic wind tunnel over the course of several days, however due to the outbreak of the COVID-19 virus, the university was closed during most of the testing phase of this thesis. Three different tests were performed to prove the workings of the designed wind turbine. Unfortunately, because only limited time on the UT wind tunnel was available, only few really accurate results were found. The tests include mounting the turbine on a car (test 1) and testing the wind turbine with a fan (test 2), these two tests were subject to many external factors and suboptimal test conditions, which influenced these test results. Finally the wind turbine was tested in the UT wind tunnel (test 3).

6.1 Test 1: The Car Test

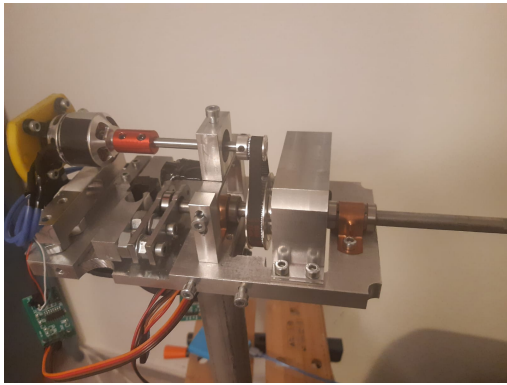
It was proposed that a way to control wind speed was to place the wind turbine on a moving car, making the assumption that the wind speed at the rotor roughly equals the speed of the car.

6.1.1 Test 1 Setup

The rotor was tested as part of the total wind turbine design and was placed on the separately designed nacelle and tower. The nacelle and tower include sensors for RPM, torque and Thrust that work on the rotor. The nacelle also includes a tooth belt transmission, a generator that generates electricity out of the rotor rotation and a centrifugal brake that prevents the rotor from spinning too fast. a picture of the nacelle and its inner workings can be seen in Figure 6.1a. The data from the sensors is transferred to an Arduino unit which displays the information on an LCD screen that is attached to the system. The LCD screen shows: Rotor torque, rotor RPM, rotor thrust, mechanical power, electrical resistance in the system, voltage, current and electrical power generated. Underneath the LCD screen a potentiometer, which is a variable electrical resistance that can be set by hand, is present. By decreasing electrical resistance, the mechanical resistance on the generator is increased. The result is an increase in torque and a decrease in RPM. This potentiometer is used to set the TSR of the wind turbine. When the rotor is spinning faster than the desired TSR, electrical resistance is decreased and vice versa. The LCD and the potentiometer can be seen in Figure 6.1b

Since it is not possible to directly connect the wind turbine to the car, the wind turbine is held outside the window. During the test the wind turbine is facing forward in driving direction of the car. The assumption is made that the wind velocity is equal to the cars velocity, however in reality many other effects influence the test in this setup. External influences in this case are things like outside wind that is blowing, the fact that the wind is influenced by the car and that the wind turbine is not held completely still or exactly in the direction of the wind. A picture of this test setup is shown in Figure 6.2.

The idea of this test is to be able to map the wind turbine behaviour at different different wind speeds and TSRs. However, due to the closure of the UT workshop and laboratory it is hard to make structural alterations to the wind turbine in case something is not working or a malfunction occurs. Furthermore, the hub does not have an angle/pitch indicator for the blade pitch, therefore only the 0° pitch is tested.



(a)



(b)

Figure 6.1: The sensors and gearing inside the nacelle (a), and the LCD screen and potentiometer attached to the wind turbine and Arduino unit (b).



Figure 6.2: The TwIN Turbine on the car.

6.1.2 Test 1 Results

The results from the car test turned out to be very limited. For this reason, only the main findings are discussed and no exact mapping of the turbine performance could be done. Exact performance results for the wind turbine are lacking and require wind tunnel testing and alterations to the turbine before it is fully functional.

The rotor performance indicated a cut-in speed of 7 m/s . Due to the generator in the wind turbine not having enough resistance to lower the TSR to the required ratio of 4, it was considered dangerous to increase the wind speed over 17 m/s . At this maximum wind speed, the brake had already kicked in, limiting the the RPM to ca. 3000 RPM . Another test without a brake was performed, resulting in a rotor RPM of ca. 4000 RPM at 17 m/s . Tests at higher wind velocities were not performed, because higher RPMs were deemed to dangerous and the cork brake lining failed at some point during the tests.

Due to the inconsistent nature of the wind, the set base wind speed of 11.11 m/s did not give a stable result for the resulting RPM. The RPM at this speed varied between $1800 - 2300\text{ RPM}$. In all cases this results in a TSR above 4. The reason for this unstable rotor RPM is most likely wind gusts outside or an inconsistent car speed. It was concluded that to reach the desired TSR of 4 and even lower TSRs, a generator with a higher mechanical resistance is required to slow down the rotor.

A positive result for the structural integrity in the rotor and hub was found. After the test all parts seemed to be in perfect condition. No screws, nuts or bolts were loosened due to vibrations. Furthermore, the rotor blades maintained their pitch angle perfectly. After use the different parts were disassembled and inspected and no indication of mechanical or material failure was found, with the exception of the cork brake lining of the centrifugal brake inside the nacelle, which failed during the test. This was because the cork was too brittle to be used as a brake lining (as well as too flammable). A new leather brake lining is applied to the centrifugal brake for further testing

The conclusions of the car test were that the turbine shows a cut in speed of 7 m/s and a TSR of minimally 6.7. The turbine functions in its goals as a wind generator, meaning that the blades spin in the wind at an RPM that is high enough to generate electricity, as well as reach the design TSR. However, due to a low internal mechanical resistance in the generator, the TSR could not be lowered enough using the electrical resistance in the system. It is critical for the correct usage of the wind turbine as well as for user safety that this TSR can be controlled and lowered. To this end, the generator needs to be replaced with a generator with a higher motor constant. This leads to a higher voltage at a lower current, increasing the efficiency of the generator and so increasing the mechanical resistance in the generator.

Finally, it is noted the the wind turbine is not suitable for these car tests as the wind turbine is quite heavy and therefore hard to hold still. Furthermore, the wind turbines electrical components do not work well when the turbine is constantly moved around.

6.2 Test 2: The Fan Test

The second test performed was a test performed in a home situation. An industrial fan used for paint drying was rented to test the turbine. In this test the fan was also combined with a self-made flow straightener.

6.2.1 Test 2 Setup

The test results of test 1 were used to improve the rotor design before this test was done. The brake lining of the centrifugal brake was replaced with a leather brake lining, which showed better results in pre-testing with a drill. Furthermore it was found that the tooth belt system was prone to slipping if the torque in the system became to high. To combat this, both axles in the system were fitted with 3D-printed (FDM printed PLA) gears.

Furthermore, to combat the issue of low mechanical resistance in the the generator, the generator was replaced with a heavier one. The new generator has a higher efficiency en therefore has higher mechanical resistance at the same electrical resistance and operating angular velocity. Using this new generator and by raising the maximum electrical resistance available to vary during operation, the new system should be able to lower the TSR below four at 11.11 m/s while also maintaining an acceptable cut-in speed. This new electrical

system does require the resistance to be varied during startup so the cut-in speed is low enough to get the rotor started. A figure showing the system in the nacelle with the new gears and generator can be seen in Figure 6.3a.

For the test an industrial paint drying fan was used. The fan was advertised to to have a volume flow of $7000 \text{ m}^2/\text{h}$ or $1.94 \text{ m}^3/\text{s}$. The fan has three settings: low, half and full. The outer and inner diameter of the fan are roughly equal to those of the TwIN Turbine: 500 and 80 mm , respectively. To determine the wind speed of the fan an anemometer was used. The anemometer can be seen in Figure 6.3b.



Figure 6.3: The sensors and gearing inside the nacelle for test 2 (a), and the anemometer used to determine the wind velocity (b).

Two different setups were used to perform the tests: a setup with and without a flow straightener. It was concluded using the anemometer that, at the maximum setting, the flow from the fan was turbulent, giving an inconsistent measuring result behind the fan and behind the turbine. The flow also increases in velocity towards the outside diameter of the fan resulting in a minimal flow speed of 6.8 m/s near the fan hub and a maximum flow speed of 12.3 m/s near the fan outer diameter. Because of this large difference it is difficult to define a single air velocity that enters the turbine and therefore making it difficult to define the operating TSR of the wind turbine. Furthermore, the turbulence and rotation the air stream from the fan could influence the rotor performance. To combat these problems a flow straightener was build out of PVC pipes. Although it was not confirmed that the flow behind the flow straightener was fully laminar, the turbulent behaviour was much less noticeable. Using the flow straightener reduced the maximum and average flow speed of the fan. Using the flow straightener the minimum flow speed at the centre of the straightener was 5 m/s and the maximum air velocity near the outer diameter was 9.4 m/s .

In Both cases the wind turbine was mounted on a workbench and the fan was mounted and fixed to a table. The workbench and the table were connected to each other to prevent either from moving and to ensure the same distance between the fan and the turbine for each test. Both situations can be seen below in Figure 6.4. The tests without the flow straightener is referred to as the turbulent test situation and the tests with the flow straightener are referred to as the straightened flow situation. Tests were performed for the minimum RPM (minimum electrical resistance) that could be measured before stall occurred and the maximum RPM (maximum electrical resistance) that could be reached before the brake activated in the system (ca. 2300 RPM). All tests were performed at the maximum setting of the fan.

6.2.2 Test 2 Results

The first result from the test was that the new generator and added electrical resistances had the desired effect. The turbine was able to reach a high rotation speed and generate electricity in both test situations and was even able to do so when the fan was set to half of maximum power (although this did require up to 20Ω of resistance added to the system). The RPM range in the turbulent situation was ca. $1500 - 2200 \text{ RPM}$. At 1500 RPM stall occurred. In the straightened flow situation The RPM range was higher: $1150 - 1900 \text{ RPM}$. This is a longer range, but at a lower average value, the reason for this is the lower average air velocity in the straightened flow situation, due to losses in the flow straightener. The straightened flow situation has a much lower minimal RPM, indicating that the turbulent behaviour and rotation in the flow might be a factor in the stalling of the turbine blades.



Figure 6.4: The test setup without the flow straightener (a), and the test setup with flow straightener (b).

For each test situation the rotor torque, thrust and mechanical power were considered. The tests were repeated and the results were put into graphs showing these values against rotor RPM. Because the TSR of operation was unknown, the RPM is shown on the X-axis instead. Because of the unknown TSR, the results could not be compared to the BEM and QBlade predictions. The power coefficient is also unknown, therefore the mechanical power is shown. The graphs showing torque, thrust and mechanical power are shown in Figure 6.5. The measured results are approximated by a fourth order polynomial trend line.

The first thing to note in in Figure 6.5 is that the turbulent flow situation has higher values for all parameters, this is due to the higher flow velocity in the turbulent flow and the losses in the flow straightener when it is applied. It is difficult to compare these results to the BEM and QBlade predictions. However considering the predictions for TSR and wind speed 11.11 m/s situations in Figure 5.17 the expected behaviour of the variables can be compared. For the thrust and power graphs a hyperbolic shape is expected and for the torque a more linear behaviour. If we compare this predicted graph shape with the results in Figure 6.5, it can be seen that the straightened flow situation resembles this prediction. However, the turbulent flow situation is much less similar, indicating that the influence of the turbulence in the flow is significant. Another thing noted from the individual measuring points is that the spread of the points is much larger in the turbulent situation. This is something that was also concluded during testing. During testing the sensors did not settle at a certain value and showed large fluctuations. Even though the straightened flow situation has fewer measuring points it is noted that the straightened situation gave much more constant values for all RPMs.

During testing several problems occurred with the 3D-printed gears. The gears would be pushed apart during use and seemingly experienced a lot of friction. The smaller (top) gear was completely stripped of its teeth after several tests. It was found that once one gear tooth breaks, the rest quickly breaks too. This method of 3D printing seems ill-suited for the application and a different material or method of production is recommended.

During one of the tests the rotor was not connected correctly to the main axle of the system, this led to the rotor falling off during one of the experiments. The accident damaged one of the rotor blades. The blade was chipped near the edge as seen in Figure 6.6. No test results with a chipped were used in Figure 6.5. However no new blade can be manufactured due to closure of the UT. Already performed tests were repeated and it was found that the chip has a negligible effect on the blade performance, However it is recommended to print a new blade as soon as possible.

This test was further used to prove the workings of the turbine. The large air flow velocity differences from the rented fan made determining the operation TSR impossible and the turbulent flow from the fan influenced the results. Testing in a (laminar flow) wind tunnel could solve these problems. It was found that the straightened flow roughly followed predicted behaviour. A wider range (especially lower) TSRs can be reached using the new generator. The addition of extra electrical resistances allowed lower cut-in speeds. For further testing, new gears are required, because the 3D printed ones break after prolonged use. Finally, due to an error made during testing, one of the blades was damaged, which does not seem to influence results, but does need to be replaced.

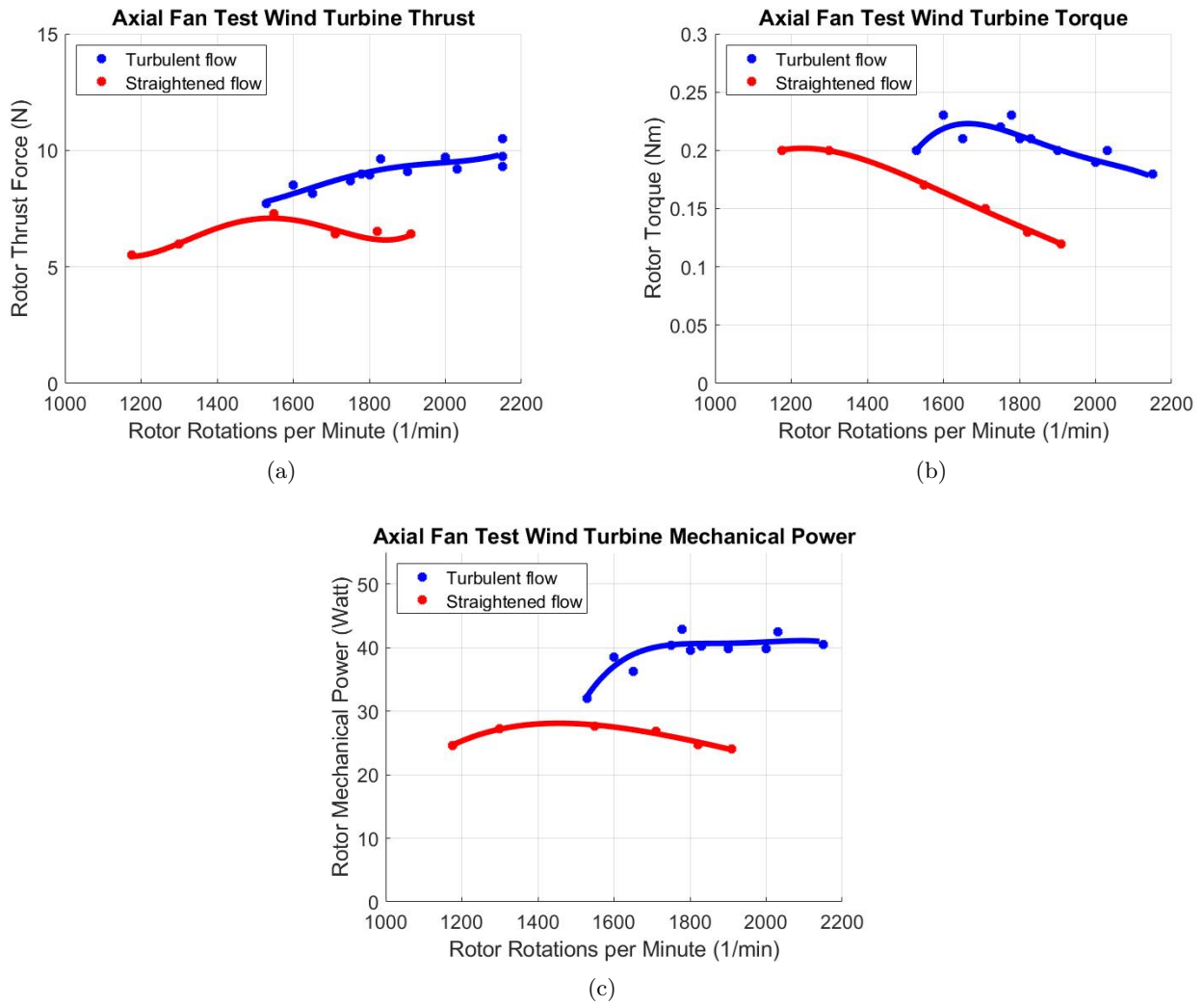


Figure 6.5: The thrust force (a), torque (b), and power (c) of the TwIN Turbine at a pitch angle of 0° using the rented fan.



Figure 6.6: The chipped rotor blade.

6.3 Test 3: Wind Tunnel Testing

On 4-6-2020 the TwIN turbine was tested in the UT aeroacoustic wind tunnel. Due to time constraints (limited to 1 day of testing) only the most important measurements were performed.

6.3.1 Test 3 Setup

Test 3 involved testing the wind turbine in the wind tunnel, the aim was to test a large amount of parameters such as varying wind speed, pitch angle and TSR. Before the test could be done the setup had to be built in the wind tunnel. The wind turbine had undergone several minor changes.

To prevent the gear from breaking during operation, the smaller gear was replaced with a metal version. A metal version of the bigger gear was also bought, but not used for the test. Due to the use of this smaller metal gear, the axle connected to the generator had to be lowered slightly. To allow for this, the position of the torque sensor was moved to under the the nacelle bottom plate. The inside of the nacelle can be seen in Figure 6.7a. The electric system was also changed slightly. During the wind tunnel tests, it was not allowed for people to be inside the wind tunnel. To be able to use the 'control box' with the LCD screen and potention meter outside the wind tunnel, it was fitted with long 5m cables that allowed the use of the control box outside of the wind tunnel. The control box was also fitted with six 50 W, 2.5 Ω resistors connected in series. These resistors could be added to the electrical system with an alligator clip, allowing the resistance in the system to be increased to up to 20 Ω including the potention meter. A picture of the modified control box can be seen in Figure 6.7b.

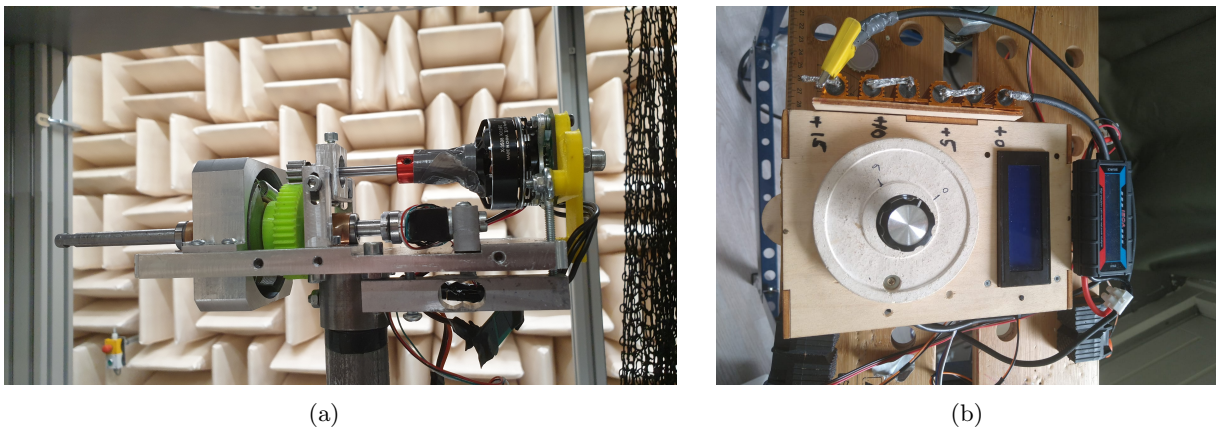


Figure 6.7: The inside of the nacelle (a), and control box (b) used during wind tunnel testing.

For the test, the wind turbine was mounted in the wind tunnel. Mounting the turbine in the wind tunnel included connecting the turbine to the testing table that was already present. Around the table, nets were put up for safety. In case of mechanical or structural failure, any loose parts would be caught by the net, preventing damage to the wind tunnel. Because it was not allowed to be inside the wind tunnel when it was running, the cables were guided through a hole in the wind tunnel wall. The wind turbine setup inside the wind tunnel can be seen in Figure 6.8a. Outside of the wind tunnel the control box was placed on a desk. The wind tunnel is equipped with a camera, pressure sensor and temperature sensor. The data from these sensors could be read from a desktop computer outside of the wind tunnel. The computer also showed a live feed of the camera in the wind tunnel. Using the data and a program installed on the computer a live feed of air velocity could also be read and graphed. Figure 6.8b shows the outside of the wind tunnel with the computers and control box.

During the operation of the wind tunnel data on air velocity and temperature, ambient pressure from the live feed was written down, as well as the data from the control box. Although the plan was to do many more measurements, only a variation of TSR over a range of 8.33 - 13.88 m/s was tested. The tested TSRs were all TSRs that could be reached with the available electrical resistance in the system (the six resistors and the potention meter). Finally, a brake test was performed to confirm the workings of the brake at 13.88 m/s . All data was entered in an Excel sheet for later processing in MatLab.

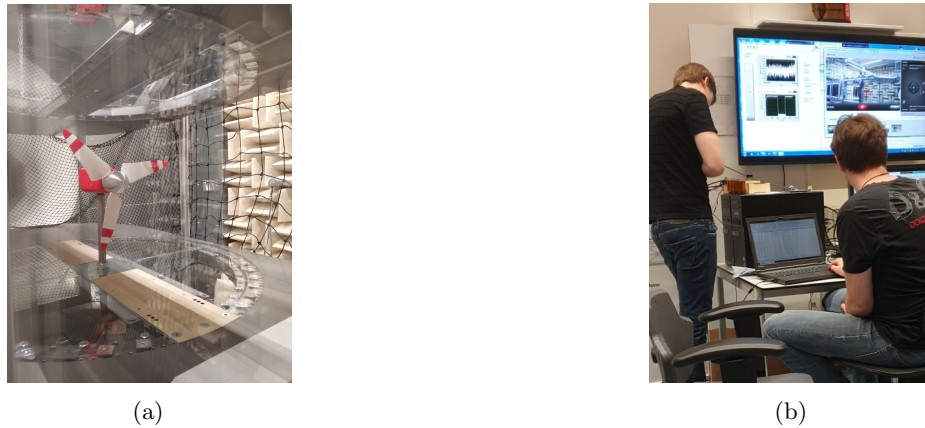


Figure 6.8: The inside of the wind tunnel (a), and the systems outside the tunnel (b).

6.3.2 Test 3 Results

The quantitative wind tunnel test results can be found in Appendix G. This data is used to create graphs in MatLab, which are discussed below. Qualitative results are discussed first. The TwIN Turbine was tested at wind speeds from 8.2 - 13.9 m/s in 5 steps. for each test as many reachable TSRs as possible were documented.

The wind turbine performed well in the wind tunnel tests. No parts showed signs of wear or malfunction. The metal gear that was used for the first time in this test, also performed well, not breaking and not tearing into the softer plastic large gear it is paired with. During operation the wind turbine produces a lot of noise, both from the rotor and from inside the nacelle. After the first test, the turbine was disassembled and inspected, it is possible that something was not assembled correctly during this reassembly, because there was a slight increase in cut-in speed after this reassembly. However, it did not impact the rotor performance significantly enough to notice during operation and the effects were only found out when the results were analysed.

The electrical system did encounter some problems. Due to a strong electromagnetic field coming from the wind tunnel 'on-switch' cable and/or badly insulated sensor cables, the sensors and control box stopped working when the wind tunnel was switched on. This was solved by guiding the sensor cables through a pipe, after this, the control box functioned properly. Other problems occurred when running the wind turbine in a high wind speed (13.9 m/s) and at low electrical resistance (1Ω) in the system. Because of the way the electrical system was designed, this meant that in this situation a lot of electrical power (ca. 90 W) was being dissipated over a very short distance in the potentiometer. This meant that the potentiometer became extremely hot. The potentiometer (and its case) became so hot that the experiment had to be stopped after several measurements at this wind speed. In the future, this could be fixed by using an electrical load instead of the potentiometer and resistor array, or by placing several resistors in parallel in the electrical system, collectively dissipating the power over a much larger distance/area.

When the raw data (see Appendix G) is observed, it can be observed that the measured torque values are not consistent. The raw torque values do not show any clear trend or dependence on the wind speed or rotor operation conditions. The reason for this is unknown, it could be that the torque sensor was influenced somehow, or that the new location does not work that well, however when the sensor was tested before the wind tunnel tests, it seemed to work correctly. After observation of these results, it was decided that a different method of determining the torque was required. This was done through characteristics of the generator, which were mapped in earlier tests. The torque is directly linked to the current produced by the generator. The connection was mapped and can be seen in Figure 6.9a. Using this relation, the torque was calculated using the known current values. The torque values as measured by the sensor and 'corrected' with this method can be seen in Figure 6.9b and 6.9c, respectively. In the rest of the results, the torque as determined from the current is used.

Next, each aspect of the rotor performance is discussed and compared to the QBlade (including corrections) predictions. Firstly, the thrust coefficient is observed. The thrust coefficient for all measurements can be seen in Figure 6.10. It must be noted that these thrust values were corrected by subtracting the error left on the thrust measurement after the test (T_{err} in Appendix G), to create more consistent results.

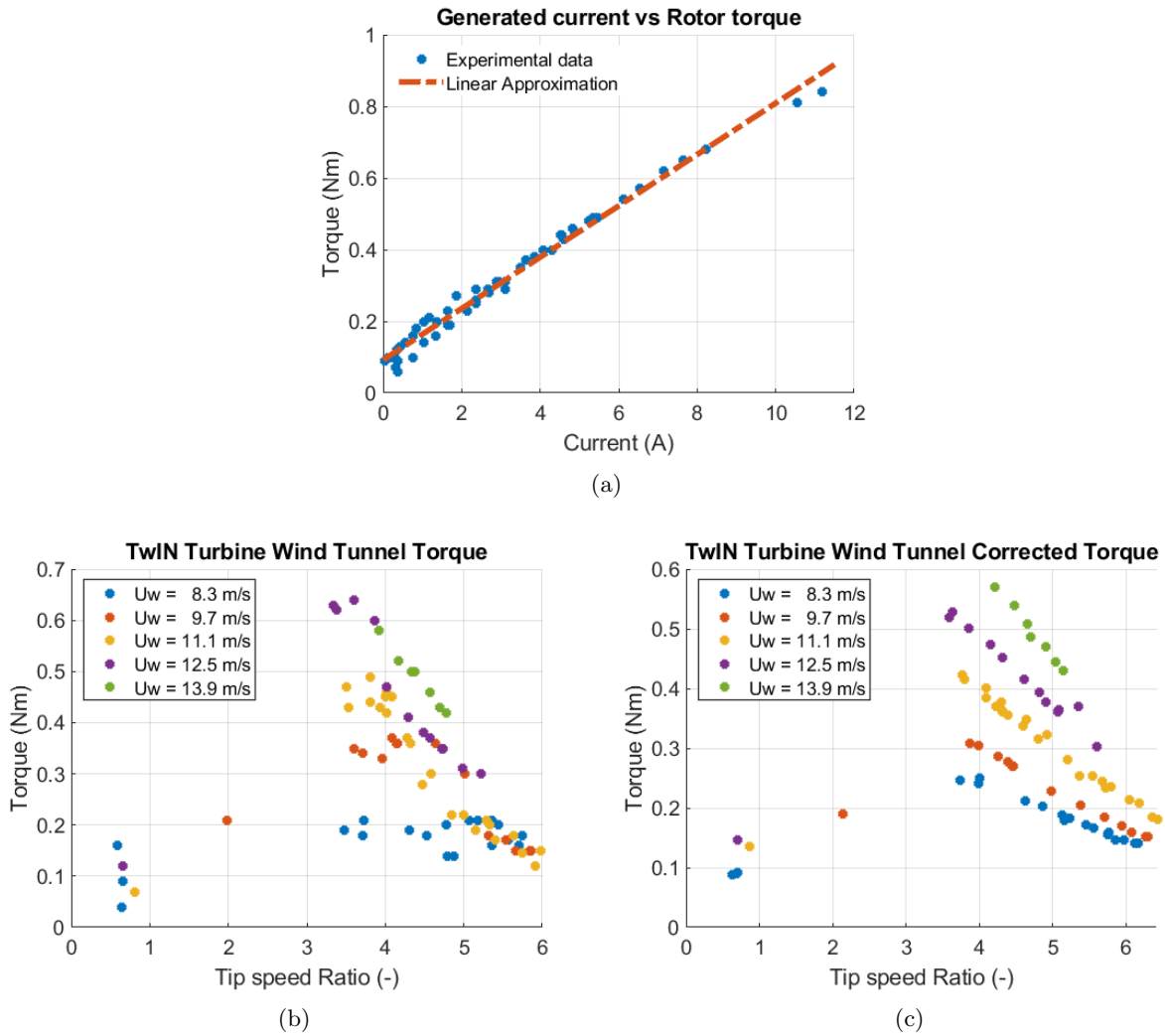


Figure 6.9: The relation between torque and current of the generator (a), the torque determined by the sensor (b) and determined from the current (c) at various wind speeds.

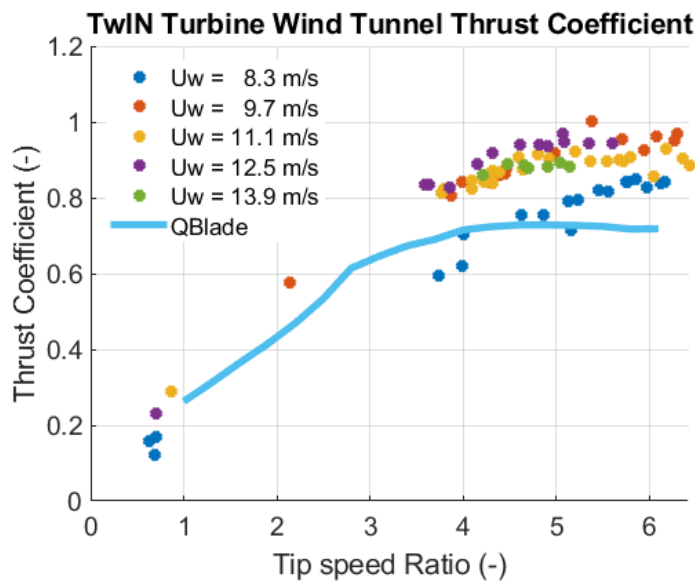


Figure 6.10: Thrust coefficient measurement results at various wind speeds and the QBlade prediction.

The first thing that is noticed is that the measurement at a wind velocity of 8.3 m/s is much lower than the measurements at higher wind velocities. The higher wind velocities yield roughly the same thrust coefficients at each TSR. A possible explanation for this is that the Reynolds number of the flow at the blades differs from the predicted Reynolds number at 11.11 m/s . No experimental data for the SD7037 airfoil at Reynolds numbers < 100.000 is known. If the comparable airfoils with data on polars for lower Reynolds numbers in Appendix C are observed, it can be seen that for these airfoils the polar performance collapses quite severely for $Re < 100.000$, it can be assumed that this is also the case for the SD7037 airfoil used on the TwIN turbine rotor blades. This would explain the low thrust coefficient for lower wind speeds. It would also explain why this does not happen for higher wind speeds/Reynolds numbers. The increase in performance is not as significant for these higher Reynolds numbers compared to severe performance drop below $Re = 100.000$.

The thrust coefficient measurements show values that are generally much higher than the QBlade prediction. With the exception of the measurement at 8.3 m/s the peak occurs between a TSR of 4 - 6 and is almost 1. This is higher than the predicted peak of around 0.75. The reason for this difference could be the blockage effect. This effect is important for ducted fans or turbines or turbines that are not placed in a completely open environment, such as the wind tunnel situation. This effect will influence the experiment if the blockage factor is larger than 10%. The blockage factor is the area of the rotor divided by the area of the test section. In the experiment the test section is determined by the upper and lower plates of the test table. However the sides are open, making it hard to determine the exact blockage factor. However, it can be an explanation for the high thrust coefficient measurement. In a situation without blockage effect the flow is partly directed away from the turbine rotor, because it chooses the path of least resistance. However, in a constrained test region the flow is partly forced through the rotor area. This increases the local air velocity. Using the work by Ryi J. et al. [35] the wind velocity at the rotor is estimated to be between 5 and 15% higher than the actual measured wind speed, due to this blockage effect. Using this increased wind speed puts the QBlade prediction roughly on the measurements. However, to determine if the blockage effect is really the reason for the high thrust coefficient values and to find what the exact blockage factor is, further research is required.

The results for the torque coefficient of the wind tunnel tests are shown in Figure 6.11. The graph includes a comparison to the predicted results from QBlade. The results are again corrected by subtracting the error in the sensor after the test from the measured value (Q_err in Appendix G) to create more consistent results.

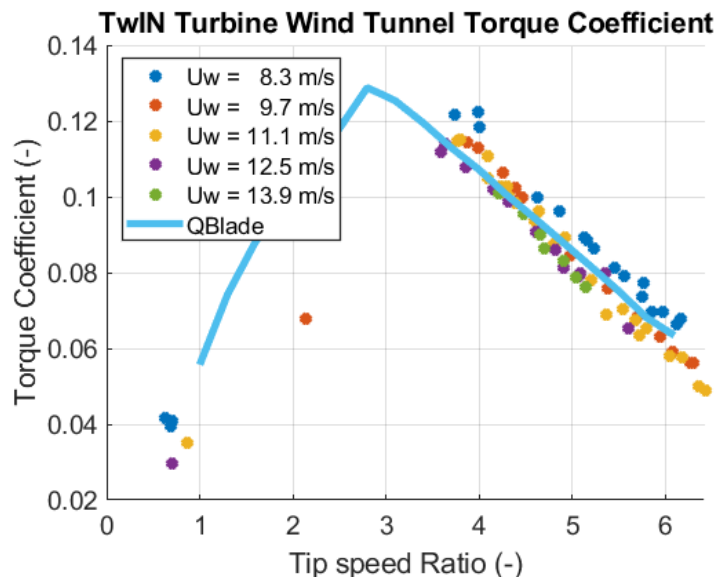


Figure 6.11: Torque coefficient measurement results at various wind speeds and the QBlade prediction.

Several interesting conclusions can be drawn from Figure 6.11. Firstly, the fact that the 8.3 m/s measurement shows the highest values for the torque coefficient. This seems to contradict the earlier theory that the lower Reynolds number influences the rotor performance at low air velocities. It is possible to find an explanation that does not contradict this theory. Because the turbine was disassembled after the 8.3 m/s test, it is possible that after reassembling the nacelle cover, the generator was experiencing internal friction, either due to heat or some other reason. This could explain both the torque and thrust coefficient behaviour. If the generator was indeed malfunctioning and experiencing friction, this would mostly influence the rotor torque (due to the

increased rotational friction on the rotating axle in the generator), lowering the value of all torque measurements after the first test, because only the 'useful' torque is measured using the generator current method. It would however, not influence the thrust sensor as it is measured on the main axle and is not influenced by the rotational friction on the generator axle. If this is true then it means that the generator friction effect is stronger than the reduced performance due to lower Reynolds numbers. It would mean that if the generator friction was not present, the torque coefficient data for $U_{wind} > 8.3 \text{ m/s}$ would be above the blue dots of the 8.3 m/s measurement. To validate this theory it is recommended that the test is performed again, making sure the generator is working correctly. This theory is also a possible explanation for the increased cut-in speed after the first test.

The next thing that can be noted from the torque coefficient graph is that the measurements match the QBlade prediction quite well, however if one takes into account the possibility of the generator experiencing friction, as well as the blockage effect, this creates a problem. The inclusion of the blockage effect would lower the torque coefficient below the QBlade prediction, but the removal of the possible generator friction would raise the torque coefficient. To see where the actual torque coefficient ends up, the blockage effect needs to be taken into account, the generator friction needs to be eliminated and the test needs to be performed again.

A final observation from the torque coefficient graph with respect to the QBlade prediction is the fact that stall of the rotor occurs near TSR 3.7, rather than the predicted 2.7. The explanation for this behaviour is probably the 360° polar extrapolation. At the time the prediction was performed in QBlade (Section 4.3), The Viterna 360° extrapolation method[24] was chosen. It was already noted that this method estimates relatively high lift values for large angles of attack. The alternative method is the method by Montgomerie[23]. When the Montgomerie method is applied to the QBlade prediction of the torque coefficient, it is found that stall is predicted to occur at around a TSR of 3.5. This is much closer to reality. Therefore it is recommended that for further QBlade performance predictions the Montgomerie 360° extrapolation is applied, especially for the case of this wind turbine.

Finally, the curve for the turbine power coefficient is observed and compared to the QBlade prediction. The power coefficient test results and QBlade comparison can be seen in Figure 6.12. The power coefficient was determined using the torque and RPM data. In this case the torque data that was determined using the electric current was used, because this gives the most insight into the 'useful' torque that is being produced in the wind turbine.

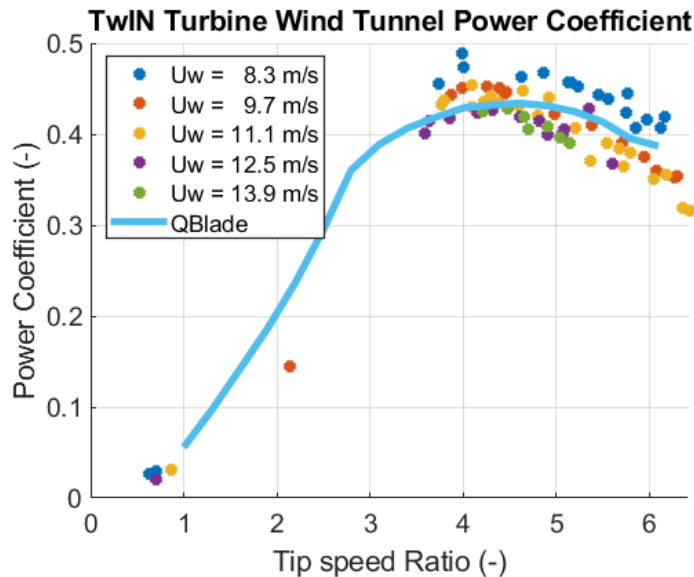


Figure 6.12: Power coefficient measurement results at various wind speeds and the QBlade prediction.

The power coefficient is directly dependent on the torque coefficient, which means that the comments above also apply to this data. The blockage effect and possible friction in the generator also apply to the power coefficient graph. Again the lowest speed measurement yields the highest values for the power coefficient, which is most likely incorrect. It would be incorrect to conclude that QBlade delivers an accurate prediction of the power coefficient without further testing. However through all tests it seems that QBlade correctly predicts the behaviour of the measured parameters as well as a semi-accurate prediction of when stall occurs, especially

when the Montgomerie 360° extrapolation method is used.

It is concluded that the requirement set in in Section 2.4 of a minimal power coefficient of 0.3 at optimal settings is met. This requirement is met even with the possible generator friction as well as in the case that the blockage effect is near the high estimation. Therefore it is concluded from this graph that a well-designed and efficient rotor was created for the TwIN Turbine. It would be possible to create an even better rotor by investigating other aerodynamic effects as well changing several aspects of the design, although efficiency gains would be marginal. Examples are things like adding winglets or decreasing the hub size. Of course many more changes can be made and further research is encouraged to increase the efficiency of the rotor, although efficiency is not the main goal for the research and measurement accuracy and reproducibility are of much higher priority

.

Chapter 7

Conclusions & Recommendations

The aim of this thesis was to design and test a wind turbine for use in the wind energy lecture series' practicals. This goal was achieved in the shape of the Twente Instrumented Nacelle Turbine (TwIN Turbine). A small wind turbine that fits the UT's aeroacoustic wind tunnel was designed and build. The rotor spins well at the tested wind speeds and the turbine generates electricity. The rotor blades were designed using blade element momentum (BEM) theory. The performed test using an industrial fan indicated that the turbine behaviour roughly matches the predicted behaviour. Further (limited) testing in the UT aeroacoustic wind tunnel indicated several problems with the QBlade and BEM performance predictions. The most prominent problem was the fact that the blockage effect is not taken into account in the numerical simulations, giving results that would only match a completely unblocked test section, which was not the case in the setup used in the UT wind tunnel, because the test table and table ceiling cause the blockage effect. However, the severity of this problem is not known. It is estimated that the blockage effect increases the local speeds at the rotor by 5 – 15%. If the exact number is known, BEM theory could be applied at these speeds to create a more accurate prediction of rotor performance. Furthermore, it is suspected that a malfunction in the generator interfered with the results. It is recommended that all tests are performed again without the generator experiencing internal friction. It is also recommended that the severity of the blockage effect of the TwIN Turbine in the UT wind tunnel is researched and mapped.

For the QBlade performance predictions the Viterna 360° extrapolation method was used. From the experiment results it was found that this method underestimates the TSR at which stall will occur. For further research it is recommended that the alternative method for extrapolation is used in QBlade, which is the Montgomerie method. Another thing that could solve this problem is to more extensively map the behaviour of the applied SD7037 airfoil, this would increase performance prediction accuracy, but this is probably a time consuming process for a relatively small increase in performance prediction accuracy.

During operation in the wind tunnel problems occurred with the electromegnetic field that came from the wind tunnel cables. It is recommended to better insulate the cables connected to the TwIN turbine in further research. A problem with the torque sensor in the turbine also occurred. The sensor gave inconsistent values, the exact reason for this is yet unknown. It might have to do with the electromagnetic field in the wind tunnel or with the friction in the generator during the wind tunnel tests. The sensor was tested outside of the wind tunnel after the tests were performed and seemed to work correctly. It is recommended to find the root of the problem and fix it. If this is not possible, the current of the generator can be used to determine the torque on the generator, as was done in this research.

The requirements set at the start of the research were mostly met by the wind turbine. The required TSR range of 3-6 was reached for wind speeds from 8.3 - 13.8 m/s . The TSR is a very important aspect of the design, because it plays a big part in wind turbine theory. For this reason several generators, potentio meters and electrical resistances were applied to the turbine to create a suitable cut-in wind speed and range of reachable TSRs. However, this system is far from ideal, because performing tests at low electrical resistance and high wind speeds results in the potentio meter becoming very hot. The potentio meter became so hot that testing had to be stopped at a wind velocity of 13.8 m/s . Because testing low TSR values at higher wind speeds could lead to a potential fire hazard, it is recommended that the electrical system is adapted to allow for higher wind speeds to be tested. This can be done by adding an array of resistors in parallel to the system over which the dissipated heat will be divided. If this change is made, tests can be performed at higher wind speeds to see what the limitations of the design are.

Due to a lack of time in the wind tunnel, pitch angle variation tests were not performed. It would be interesting to compare this results to QBlade predictions and to include this data in the wind turbine performance database. It is recommended to perform these tests.

Some structural alterations and finishing are also recommended. Firstly, during testing, one of the rotor blades chipped. It is recommended to print a new blade to replace the chipped blade. The rotor hub has only one hole for a set screw to connect it to the axle. It is recommended to add another hole on the other side for two reasons. Firstly, it will ensure a tighter fit of the hub on the axle and prevent the rotor from slipping. Secondly, the rotor needs to be perfectly symmetric to prevent vibrations. The blade foot components at the edge of the blades are currently made out of aluminium, as well as the hub component. Although in its current state the blade pitch can be altered well, it is recommended that, if new blade foot parts were to be made, they are made out of brass. Using brass will lower the friction between the blade foot and the hub and will make it easier to rotate the blade and adjust the pitch. For the rotor axle that connects the hub to the nacelle some alterations are also recommended. Firstly, it is connected to remake this axle out of hardened steel rather than the currently used unhardened steel. This is recommended because the bearings on the axle are leaving marks on the axle, which could influence the rotor performance long term. Furthermore, the edges of the end of the axle at the hub side should be filed down to ensure a better fit with the hub, because the set screws in the hub are currently not touching the flat sides of the rotor axle.

The designed rotor is deemed quite efficient and definitely suitable for operation. However, improvements can be made. Blades can be redesigned and more aerodynamic effects can be taken into account during this process. Things that could increase rotor efficiency if incorporated effectively are adding winglets and decreasing the hub size. Many more alterations can be made and research into improvements is encouraged but not considered a priority.

In conclusion, a wind turbine for use at the UT aeroacoustic wind tunnel was designed. In its current state the wind turbine can be applied in the wind tunnel safely at wind speeds from 8.3 - 13.8 m/s Performance predictions using QBlade match the rotor performance well, but many effects are not being taken into account. Much more research into turbine performance is recommended and many more tests can be done.

Bibliography

- [1] BP, “Bp statistical review of world energy,” 2019. 68th edition.
- [2] C. F. Climate and E. Solutions, “Renewable energy,” 2020. <https://www.c2es.org/content/renewable-energy/>.
- [3] D. Roberts, “These huge new wind turbines are a marvel. theyre also the future.,” March 2019. VOX(2019), <https://www.vox.com/energy-and-environment/2018/3/8/17084158/wind-turbine-power-energy-blades>.
- [4] Knivesandtools.com, “Texenergy infinite air wind turbine ia-001, wind generator,” 2020. <https://www.knivesandtools.com/en/pt/-texenergy-infinite-air-wind-turbine-ia-001-wind-generator.htm>.
- [5] Makerbot, “Thingiverse,” 2020. <https://www.thingiverse.com/>.
- [6] Knivesandtools.com, “Mkiii 50 watt 3d printable wind turbine by 3dprintable1,” april 2018. <https://www.thingiverse.com/thing:2851306>.
- [7] C. L. Botasso, F. Campagnolo, and V. Petrovic, “Wind tunnel testing of scaled wind turbine models:beyond aerodynamics,” April 2014. Journal of Wind Engineeringand Industrial Aerodynamics Volume 127, Pages 11-28.
- [8] U. of Twente.
- [9] B. Afework, J. Hanania, K. Stenhouse, and J. Donev, “Betz limit,” July 2018. University of Calgary, <https://www.c2es.org/content/renewable-energy/>.
- [10] A. van Garrel, “Wind energy lecture slides,” 2019. University of Twente, Faculty of Engineering Technology, Department of Thermal and Fluid Engineering.
- [11] P. J. Schubel and R. J. Crossley, “Wind turbine blade design,” May 2012. Energies 2012, 5, 3425-3449; doi:10.3390/en5093425.
- [12] M. O. L. Hansen, “Aerodynamics of wind turbines,” 2015. Earthscan,978-1-138-77507-7,978-1-315-76998-1.
- [13] N. Hall, “The lift equation,” May 2015. NASA ,<https://www.grc.nasa.gov/www/k-12/airplane/lifteq.html>.
- [14] J. Manwell, J. McGowan, and A. Rogers, “Wind energy explained, theory, design and application,” 2009. Wiley, ISBN 978-0-470-01500-1.
- [15] S. Gundtoft, “Wind turbines,” june 2009. Fluid Dynamics, Department of Mechanical Engineering, University College of Aarhus.
- [16] O. de Vries, “Fluid dynamic aspects of wind energy conversion,” july 1979. AGARDograph No. 243.
- [17] H. Snel, R. Houwink, J. Bosschers, W. J. Piers, G. J. Van Bussel, and A. Bruining, “Sectional prediction of s-d effects for stalled flow on rotating blades and comparison with measurements,” Mar 1993.
- [18] D. Marten and J. Wendler, “Qblade guidelines,” January 2013. v0.6, TU berlin.
- [19] J. Hernndez and A. Crespo, “Aerodynamic calculation of the performance of horizontal axis wind turbines and comparison with experimental results,” *Wind Engineering*, vol. 11, no. 4, 1987.

-
- [20] C. A. Lyon, A. P. Broeren, P. Gigure, A. Gopalarathnam, and M. S. Selig, "Summary of low-speed airfoil data," 1997. Soartech Publications, ISBN 0-9646747-3-4.
- [21] MultiMedia LLC, "Airfoil tools," 2019. <http://airfoiltools.com/>, 2019-12-3.
- [22] Wikipedia, "Drag polar," november 2018. https://en.wikipedia.org/wiki/Drag_polar, 2019-12-3.
- [23] B. Montgomerie, "Methods for root effects, tip effects and extending the angle of attack range to +180, with application to aerodynamics for blades on wind turbines and propellers," June 2005. Swedish Defence Research Agency, Aeronautics, FFA, SE-172 90, Stockholm, ISSN 1650-1942.
- [24] L. A. Vitera and R. D. Corrigan, "Fixed pitch rotor performance of large horizontal axis wind turbines," January 1982. SA Lewis Research Center, Cleveland, Ohio.
- [25] C. Butterfield, A. Hansen, D. Simms, and G. Scott, "Dynamic stall on wind turbine blades," December 1991. National Renewable Energy Laboratory(NREL).
- [26] Emhart Teknologies, "Helicoil insert systems," 2003. Emhart Teknologies Heli-Coil Bulletin.
- [27] ASM Aerospace Specification Metals Inc. , "Aluminum 6061-t6; 6061-t651 asm material data sheet." <http://asm.matweb.com/search/SpecificMaterial.asp?bassnum=MA6061T6>.
- [28] University of Twente, "Rapid prototyping lab, techniques," 2020. <https://www.utwente.nl/en/rpl/Techniques/>.
- [29] University of Twente, "Rapid prototyping lab, 3d-printers," 2020. <https://www.utwente.nl/en/rpl/3D-Printers/>.
- [30] Formlabs, "Clear photopolymer resin for form 1+ and form 2," April 2016. <https://www.utwente.nl/en/rpl/Data%20sheets/Form%202/clear-datasheet.pdf>.
- [31] e-Manufacturing Solutions, "Pa 2200 performance 1.0," March 2010. <https://www.utwente.nl/en/rpl/Data%20sheets/Formiga%20P110/pa2200-preformance-1.0.pdf>.
- [32] T. de Lange, "A study on the limitations and the correction models of the blade element momentum method," 2018. University of Twente, Faculty of Engineering Technology.
- [33] W. Z. Shen, R. Mikkelsen, J. N. Srensen, and C. Bak, "Tip loss corrections for wind turbine computations," *Wind Energy*, vol. 8, 2005. <https://onlinelibrary.wiley.com/doi/abs/10.1002/we.153>.
- [34] A. Maheri, C. Toomer, and S. Noroozi, "Damping the fluctuating behaviour and improving the convergence rate of the axial induction factor in the bemt-based rotor aerodynamic codes," March 2006. ISBN 9781622764679.
- [35] J. e. a. Rye, "Blockage effect correction for a scaled wind turbine rotor by using wind tunnel test data," November 2014. *Renewable Energy* (2014), <http://dx.doi.org/10.1016/j.renene.2014.11.057>.

Appendix A

BEM Equations Derivation

To determine the airfoil geometry and performance two theories are applied. These are the blade element theory and momentum theory. In momentum theory, an analysis is done of the forces on a control volume based on the conservation of linear and angular momentum. In blade element theory a section of the blade is analyzed with respect to the blade geometry. When these two theories are combined, the blade shape can be related to the power extracted from the wind. This theory is called the Blade Element Momentum (BEM) theory. In this section, both theories are explained, with and without wake rotation. This theory can be used to design a simple wind turbine rotor and is used to explain the workings of the optimisation done by the QBlade program that is applied to this project in section 4.3.

A.1 Momentum Theory

The aim in this section is to find expressions for the thrust and torque using linear and angular momentum conservation. First a situation without wake rotation is considered. A control volume with boundaries at the start, the end and at two cross-sections in a stream tube is considered. In this schematic these cross-sections are designated 1-4 and parameters at these cross-sections will be denoted with a subscript. An actuator disc is placed in the stream tube, which represents the turbine. This disc creates a discontinuity in the pressure of the air that flows through it. The flow is assumed to be homogeneous, incompressible and steady state. Furthermore, the disc is assumed to have no frictional drag, the thrust is uniform over the disc the wake is non-rotating and the far upstream and downstream pressures are assumed to be equal. The situation can be seen in Figure A.1.

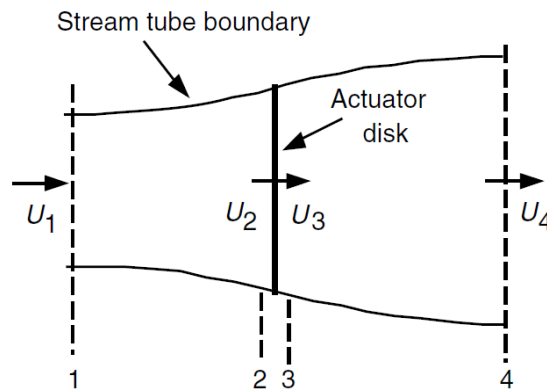


Figure A.1: Actuator disc model of a wind turbine; U , mean air velocity; 1, 2, 3, and 4 indicate locations[14]

The force that the wind exerts on the blades/disc is called the thrust. The thrust in case of a one dimensional, incompressible, time-invariant flow is equal to the change of momentum of the air stream. This is defined as:

$$T = U_1 (\rho AU)_1 - U_4 (\rho AU)_4 \quad (\text{A.1})$$

With ρ the density, A the cross-sectional area and U the air velocity.

For steady state flow, the mass flow \dot{m} is constant. Since $\dot{m} = \rho AU$:

$$T = \dot{m} (U_1 - U_4) \quad (\text{A.2})$$

No work is done in the fluids between 1-2 and 3-4, therefore Bernoulli's equation for pressure can be used. Resulting in:

$$p_1 + \frac{1}{2}\rho U_1^2 = p_2 + \frac{1}{2}\rho U_2^2 \quad (\text{A.3})$$

and

$$p_3 + \frac{1}{2}\rho U_3^2 = p_4 + \frac{1}{2}\rho U_4^2 \quad (\text{A.4})$$

The pressure difference Δp over the disc can be defined as:

$$\Delta p = p_3 - p_2 \quad (\text{A.5})$$

Equation A.4 can then be rewritten to:

$$p_2 - \Delta p + \frac{1}{2}\rho U_3^2 = p_4 + \frac{1}{2}\rho U_4^2 \quad (\text{A.6})$$

Now, subtracting Equations A.3 and A.6 gives:

$$\Delta p = \frac{1}{2}\rho (U_1^2 - U_4^2) \quad (\text{A.7})$$

This gives the static pressure drop over the disc. The pressure drop can also be determined using the change of momentum over time $\dot{m}dv$ in the rotor:

$$\Delta p = \rho U_{rot} (U_1 - U_4) \quad (\text{A.8})$$

Where U_{rot} is the axial speed in the rotor plane. Since the mass flow is constant: $\rho U_2 A_2 = \rho U_3 A_3$ and $A_2 = A_3$, this means the axial speed through the rotor is $U_{rot} = U_2 = U_3$.

Combining Equations A.7 and A.8 gives an expression for the axial speed through the rotor U_{rot} :

$$U_{rot} = \frac{1}{2} (U_1 - U_4) \quad (\text{A.9})$$

This means that the wind velocity at the rotor plane is the average of the free stream velocity and the downstream wind speed. The fractional decrease in wind velocity between the free stream and the rotor plane is defined as a , this is called the axial induction factor:

$$a = \frac{U_1 - U_2}{U_1} \quad (\text{A.10})$$

Defining the rotor plane wind speed as $U_2 = U_1(1 - a)$ and the downstream wind speed $U_4 = U_1(1 - 2a)$. when a approaches 1/2 the wind slows down to zero and the used model becomes unusable. Finally, $U_1 a$ is called the induced velocity at the rotor.

The thrust can be defined as the result of the pressure difference over the area over the disc, resulting in:

$$T = A (\Delta p) = \frac{1}{2}\rho A (U_1^2 - U_4^2) \quad (\text{A.11})$$

When the axial induction factor is used, Equation A.11 can be rewritten to:

$$T = \frac{1}{2}\rho A U^2 [4a(1 - a)] \quad (\text{A.12})$$

Where $A = A_2$, the rotor area and $U = U_1$, the free stream wind velocity.

The power P produced by the rotor is defined as the change in kinetic energy in the air and can be expressed as a function of the axial induction factor a :

$$P = \frac{1}{2}\rho (U_1 - U_4) A = 2\rho a (1 - a)^2 \quad (\text{A.13})$$

The equations for thrust and power A.11 and A.13 can be expressed as:

$$P = \frac{1}{2} \rho v_1^3 A C_P \quad (\text{A.14})$$

$$T = \frac{1}{2} \rho v_1^2 A C_T \quad (\text{A.15})$$

with:

$$C_t = 4a(1 - a) \quad (\text{A.16})$$

$$C_p = 4a(1 - a)^2 \quad (\text{A.17})$$

Optimising the power coefficient C_P is the key to designing an efficient wind turbine. It can be deduced that the optimal value for C_P occurs at $a = 1/3$, resulting in a power coefficient of $C_P = 16/27$, which is known as the Betz limit.

Next, it is noted that wake rotation is present in the flow behind the disc. A new situation is proposed, with a rotating actuator disc. A schematic view of the flow through an horizontal axis turbine with wake rotation is shown in Figure A.2. The rotation in the wake means that less energy is extracted by the rotor than is expected in the case without wake rotation. It is assumed that the rotation in the wake ω is small compared to the rotation speed of the blades Ω . Because of this, it is assumed that the pressure in the free stream is equal to the pressure in the far wake: $p_1 = p_4$. In this stream, an annular control volume is considered that moves with the angular velocity of the blades. This annular stream tube has a radius r and a thickness of dr and can be seen in Figure A.3.

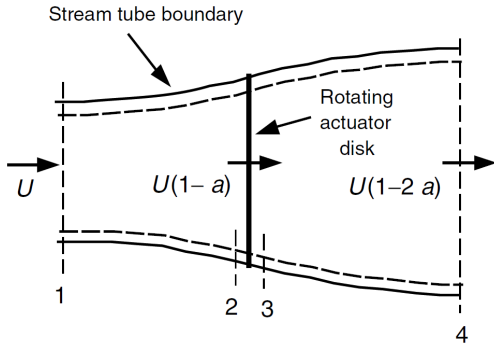


Figure A.2: Geometry for rotor analysis; U , velocity of undisturbed air; a , induction factor; r , radius[14]

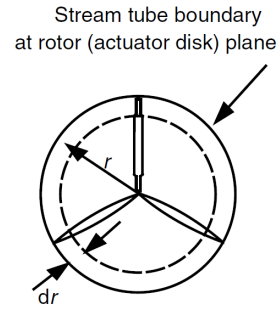


Figure A.3: Annular stream tube[14]

The area of the cross-sectional area is equal to:

$$dA = 2\pi r dr \quad (\text{A.18})$$

Bernoulli's equation for pressure is applied to sections before and after the blades, to derive an expression for the static pressure difference across the blades. Across the flow of the disc, the angular velocity of the flow increases with ω , axial component remains constant.[14] This gives:

$$p_2 + \frac{1}{2} \rho (\Omega r)^2 = p_3 + \frac{1}{2} \rho ((\Omega + \omega) r)^2 \quad (\text{A.19})$$

Therefore:

$$p_2 - p_3 = \rho \left(\Omega + \frac{1}{2} \omega \right) \omega r^2 \quad (\text{A.20})$$

From this, the resulting thrust on an annular element in the disc can be calculated:

$$dT = (p_2 - p_3) dA = \left[\rho \left(\Omega + \frac{1}{2} \omega \right) \omega r^2 \right] 2\pi r dr \quad (\text{A.21})$$

When an angular induction factor a' is defined as:

$$a' = \omega/2\Omega \quad (\text{A.22})$$

The equation for thrust force including wake rotation then becomes:

$$dT = 4a'(1 + a')\frac{1}{2}\rho\Omega^2r^22\pi r dr \quad (\text{A.23})$$

When the thrust equation is determined in the same manner, but using the axial induction factor a , the thrust equation then becomes:

$$dT = 4a(1 - a)\frac{1}{2}\rho U^2r^22\pi r dr \quad (\text{A.24})$$

Equating Equations A.24 and A.23 gives:

$$\frac{a(1 - a)}{a'(1 + a')} = \frac{\Omega^2r^2}{U^2} = \lambda_r^2 \quad (\text{A.25})$$

Where λ_r is the local speed ratio. The tip speed ratio λ is defined:

$$\lambda = \Omega R/U \quad (\text{A.26})$$

The equation for torque Q is defined using the conservation of angular momentum. The exerted torque on the rotor Q must equal the change in angular momentum of the wake. Using $U_2 = U(1 - a)$ and $a' = \omega/2\Omega$ this becomes:[15]

$$dQ = d\dot{m}(\omega r)(r) = (\rho U_2 2\pi r dr) (\omega r)(r) = 4a'(1 - a)\frac{1}{2}\rho U \Omega r^3 2\pi r dr \quad (\text{A.27})$$

The total torque can be defined:

$$Q = \frac{1}{4}\rho A D U^2 C_q \quad (\text{A.28})$$

and

$$C_q = 4a'(1 - a)\lambda \quad (\text{A.29})$$

A.1.1 Blade Element Theory

Next, blade element theory is considered. For this theory it is assumed that the forces on the blades are determined purely by the lift and drag coefficients of the airfoil. To determine the forces, the blade is divided into N sections with a length of dr . It is assumed that there is no radial flow and therefore no interactions between the sections. The lift force is perpendicular to the relative wind velocity and the drag force is parallel to the relative wind velocity. The relative wind velocity consists of the wind velocity at the rotor and the wind velocity due to rotation of the blade. The rotational component consists of the blade angular velocity and the induced angular velocity. The equation for the rotational component becomes:

$$\Omega r + (\omega/2)r = \Omega r(1 + a') \quad (\text{A.30})$$

before the derivation is continued, first a number of parameters have to be defined. To do this a schematic view of the airfoil is shown, including forces, important angles and geometry parameters. situation can be seen in Figure A.4.

In Figure A.4, $U(1 - a)$ is the wind velocity at the blades, U_{rel} is the relative wind velocity, θ_p is the section pitch angle, also known as the twist, α is the angle of attack (AoA), $\varphi = \theta_p + \alpha$ is the angle of relative wind, dF_L is the lift force, dF_D is the drag force, dF_T is the thrust force and dF_M is the force that induces a moment and drives the rotation of the rotor. Furthermore several equations can be derived from these figures and Equations 3.10 and 3.11 for lift and drag:

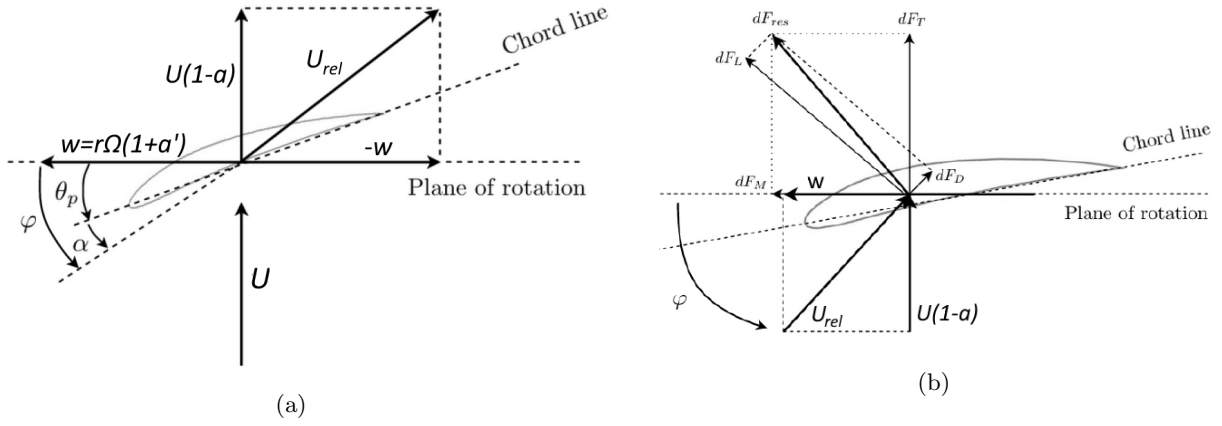


Figure A.4: Geometric(a) and force(b) parameters working on the airfoil

$$\varphi = \theta_p + \alpha \quad (\text{A.31})$$

$$\tan \varphi = \frac{U(1-a)}{\Omega r(1+a')} = \frac{(1-a)}{(1+a')\lambda_r} \quad (\text{A.32})$$

$$U_{rel} = U(1-a)/\sin \varphi \quad (\text{A.33})$$

$$dF_L = C_l \frac{1}{2} \rho U_{rel}^2 c dr \quad (\text{A.34})$$

$$dF_D = C_d \frac{1}{2} \rho U_{rel}^2 c dr \quad (\text{A.35})$$

$$dF_T = dF_L \cos \varphi + dF_D \sin \varphi \quad (\text{A.36})$$

$$dF_M = dF_L \sin \varphi - dF_D \cos \varphi \quad (\text{A.37})$$

When B is defined as the number of blades, the thrust force on a section r from the centre can be defined as:

$$dF_T = B \frac{1}{2} \rho U_{rel}^2 (C_l \cos \varphi + C_d \sin \varphi) c dr \quad (\text{A.38})$$

The torsion at a section r from the center is defined:

$$dQ = B r dF_M = B \frac{1}{2} \rho U_{rel}^2 (C_l \sin \varphi - C_d \cos \varphi) c r dr \quad (\text{A.39})$$

A.1.2 Applying BEM Theory to Determine Blade Shape

The BEM theory can be applied to determine the shape of the rotor blade, It uses parts of both momentum and beam element method. Assuming that $C_d = 0$ and there are no tip loss effects (which will be explained later). To describe the optimal relative velocity angle φ and chord length two methods can be applied, resulting in different angles and chord lengths. The first is the Betz optimal chord, which is determined, considering only the Betz limit (best performance at $a = 1/3$) as a factor for the chord length optimization. It assumes no wake rotation, therefore $a' = 0$. Applying these assumptions to Equation A.32 yields:

$$\varphi_{Betz} = \tan^{-1} \left(\frac{2}{3} \lambda_r \right) \quad (\text{A.40})$$

Next, the ideal chord length, assuming no wake rotation is determined. Equation A.39 is considered and assuming that $C_l \gg C_d$ this becomes:

$$dQ = B \frac{1}{2} \rho U_{rel}^2 C_l \sin(\varphi) c r dr \quad (\text{A.41})$$

The power produced results from the torsion working on the blade. The total power then becomes:

$$dP = dQ\Omega = B\frac{1}{2}\rho U_{rel}^2 dr c C_l \sin(\varphi) c\Omega \quad (\text{A.42})$$

From Betz' law the maximum power is known:

$$dP_{Betz} = \frac{16}{27} \frac{1}{2} \rho U^3 (2\pi r dr) \quad (\text{A.43})$$

Since no wake rotation is assumed for the Betz' optimal chord the rotational speed is defined as:

$$w = \Omega r = \cos(\varphi) U_{rel} \quad (\text{A.44})$$

Combining Equations A.42 and A.43 and adding the definitions in Equation A.33 and A.44 and assuming $a = (1/3)$, results in the Betz optimal chord length c_{Betz}

$$c_{Betz} = \frac{8\pi r}{3BC_l \lambda_r} \sin(\varphi) \quad (\text{A.45})$$

The Betz optimal is a good indication of the ideal chord length and twist, however a more efficient rotor blade can be designed when the wake rotation is taken into account. When this is the case, $a' \neq 0$ and the ideal twist and chord length change.

As mentioned in Section A.1, The change in velocity in the rotor plane is half of the total velocity change between the upstream and downstream flows (see Figure A.3). Which means that for the difference in relative velocity, a vector \vec{v} can be defined as:

$$\vec{v} = \vec{U}_{rel1} + \frac{1}{2} \Delta \vec{v} \quad (\text{A.46})$$

Again assuming the drag force to be much smaller than the lift force, it can be assumed that the direction of the vector $\Delta \vec{v}$ is parallel to the lift force vector dF_L . And the flow directions can be defined in the upstream, rotor plane and downstream flow, as seen in Figure A.5.

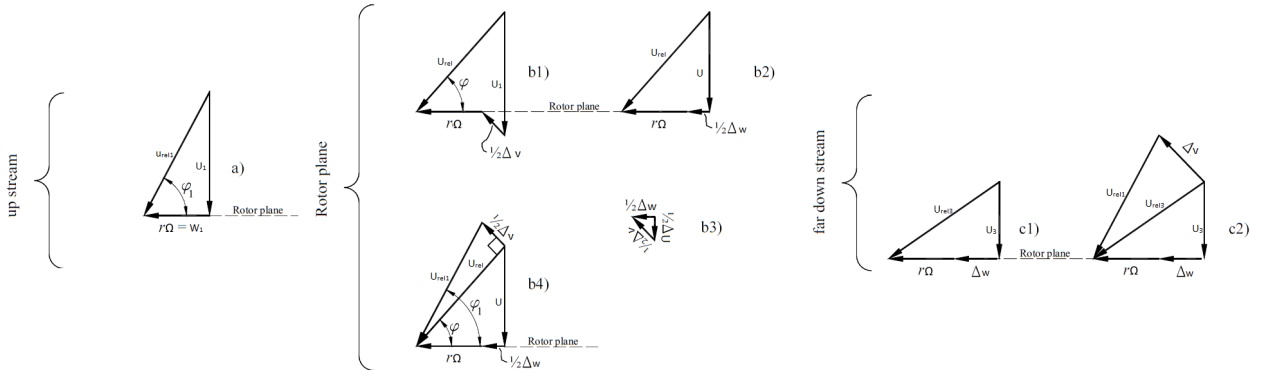


Figure A.5: Speed in the rotor plane a) far upstream; b) in the rotor plane and; c) far down stream[15]

From Figure A.5 the following relations can be derived:

$$v = U_{rel1} \cos(\varphi_1 - \varphi) \quad (\text{A.47})$$

$$U = w \sin(\varphi) \quad (\text{A.48})$$

$$U = U_{rel1} \cos(\varphi_1 - \varphi) \sin(\varphi) \quad (\text{A.49})$$

$$\Delta v = 2U_{rel1} \sin(\varphi_1 - \varphi) \quad (\text{A.50})$$

From conservation of momentum can be derived:

$$dF_L = \Delta v \dot{m} \quad (\text{A.51})$$

Where \dot{m} is the mass flow through the ring element at r :

$$\dot{m} = 2\rho\pi r dr U \quad (\text{A.52})$$

The power then equals:

$$dP = dM\omega \quad (\text{A.53})$$

$$= dF_L \sin(\varphi) r \omega \quad (\text{A.54})$$

$$= \Delta v \dot{m} \sin(\varphi) r \omega \quad (\text{A.55})$$

$$= \{2U_{rel1} \sin(\varphi_1 - \varphi)\} (2\rho\pi r dr) U_{rel1} \cos(\varphi_1 - \varphi) \sin(\varphi) \sin(\varphi) r \omega \quad (\text{A.56})$$

$$= r^2 \omega \rho 2\pi dr U_{rel1}^2 \sin[2(\varphi_1 - \varphi)] \sin^2(\varphi) \quad (\text{A.57})$$

This results in an equation that links the power to the angle of relative wind φ . Solving $d(dP)/d\varphi = 0$ will yield the angle φ that yields the highest power. Solving this gives:

$$\varphi_{Schmitz} = \frac{2}{3}\varphi_1 \quad (\text{A.58})$$

Noting in Figure A.5 that $\varphi_1 = \tan^{-1}(U_1/r\omega)$ then:

$$\varphi_{Schmitz} = \frac{2}{3}\varphi_1 = \frac{2}{3}\tan^{-1}(U_1/r\omega) = \frac{2}{3}\tan^{-1}(1/\lambda_r) \quad (\text{A.59})$$

Next, the Schmitz optimal chord length is determined. Looking at Equation A.56, Equation A.58 is added to gain the expression:

$$dF_L = 2U_{rel1}^2 2\rho\pi r dr \sin\left(\frac{\varphi_1}{3}\right) \cos\left(\frac{\varphi_1}{3}\right) \sin\left(\frac{2\varphi_1}{3}\right) = 2U_{rel1}^2 2\rho\pi r dr \sin^2\left(\frac{\varphi_1}{3}\right) \cos^2\left(\frac{\varphi_1}{3}\right) \quad (\text{A.60})$$

Equation A.34 from the beam element theory is applied together with Equation A.49 and rewritten to:

$$dF_L = \frac{1}{2}\rho U_{rel1}^2 B c dr C_L \cos\left(\frac{\varphi_1}{3}\right) \quad (\text{A.61})$$

Combining Equation A.60 and A.61, where $\varphi_1 = 2/3\varphi$, gives the Schmitz optimal chord length:

$$c_{Schmitz} = \frac{1}{B} \frac{16\pi r}{C_l} \sin^2\left(\frac{1}{3}\tan^{-1}\left(\frac{R}{\lambda r}\right)\right) \quad (\text{A.62})$$

A.1.3 Tip and Root Loss

These proposed geometry parameters are a good start for designing the rotor blades, however the design is not yet reliable enough. Some effects that are not taken into account such as tip and root loss.

In practice air flows around the tip and root from the lower to the upper surface, due to the difference in pressure. This effect reduces the lift the blade generates and therefore the power. To correct for this loss, a correction factor F is introduced. The proposed correction factor is the one by Prandtl[16] For the tip loss:

$$F_{tip} = \left(\frac{2}{\pi}\right) \cos^{-1} \left[\exp\left(-\left\{\frac{(B/2)[1 - (r/R)]}{(r/R) \sin \varphi}\right\}\right) \right] \quad (\text{A.63})$$

Where the inverse cosine is in radians (otherwise the first factor becomes $1/90$), F is always between 0 and 1. This tip loss correction factor is added to the equations for thrust and torque A.24 and A.27:

$$dT = F_{tip} \rho U^4 a(1-a)\pi r dr \quad (\text{A.64})$$

$$dQ = F_{tip} (\rho U^2 2\pi r dr) (\omega r)(r) = 4F a'(1-a)\rho U \pi r^3 \Omega dr \quad (\text{A.65})$$

When this change in the torque equation is applied to the derivations for the optimal chord lengths, the result equals:

$$c_{Betz} = F_{tip} \frac{8\pi r}{3BC_l \lambda r} \sin(\varphi) \quad (\text{A.66})$$

$$c_{Schmitz} = F_{tip} \frac{1}{B} \frac{16\pi r}{C_l} \sin^2\left(\frac{\varphi_1}{3}\right) \quad (\text{A.67})$$

A similar equation exists for the root loss which is:

$$F_{root} = \frac{2}{\pi} \cos^{-1} \left[\exp \left(- \left\{ \frac{(B/2) [r - R_{hub}]}{r \sin \varphi} \right\} \right) \right] \quad (\text{A.68})$$

With the newly adapted equations, the chord length reduces to zero at the tip, creating a pointed blade end.

Appendix B

Lift Over drag Graphs for Selig Airfoils

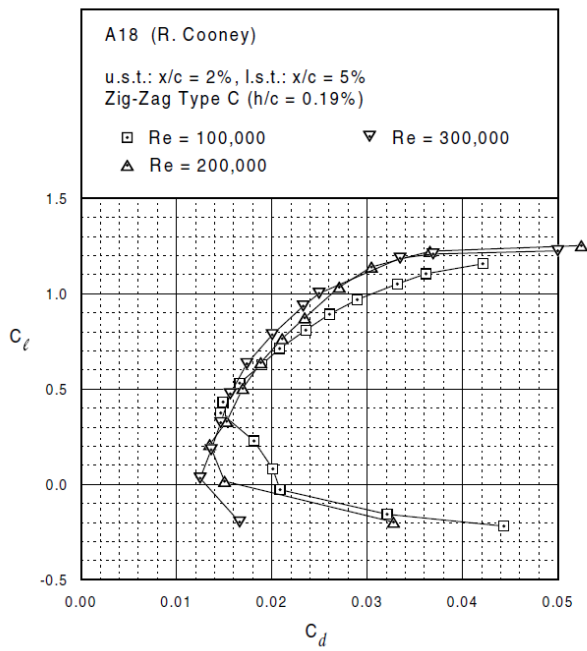


Figure B.1

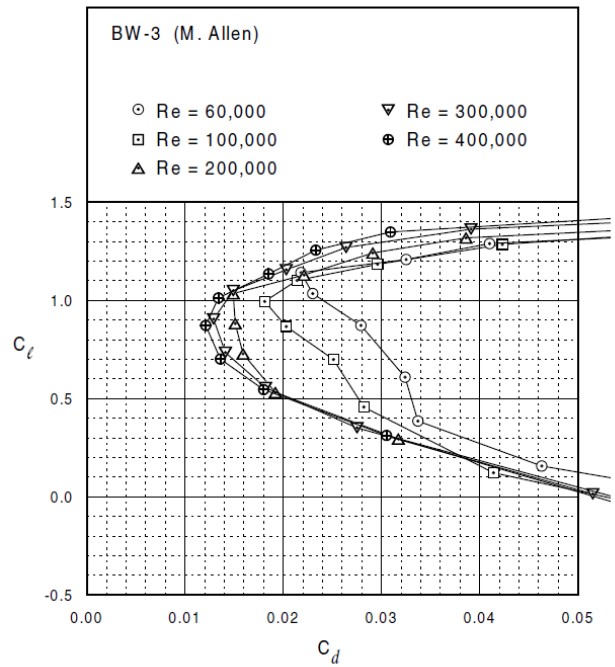


Figure B.2

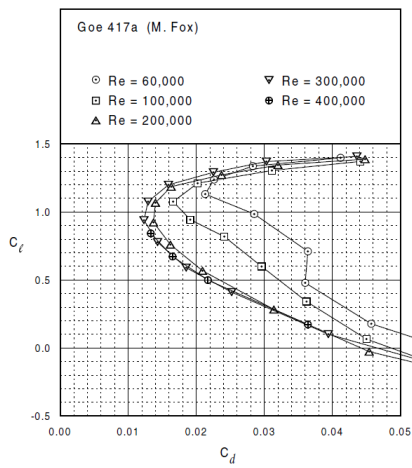


Figure B.3

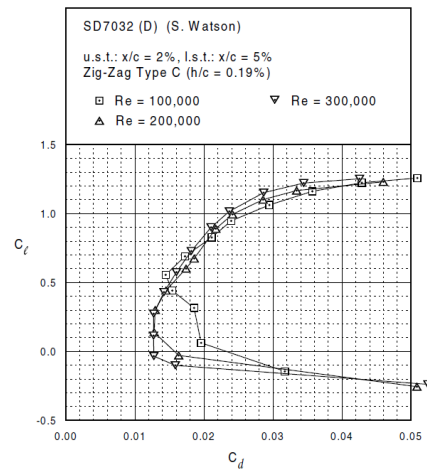


Figure B.4

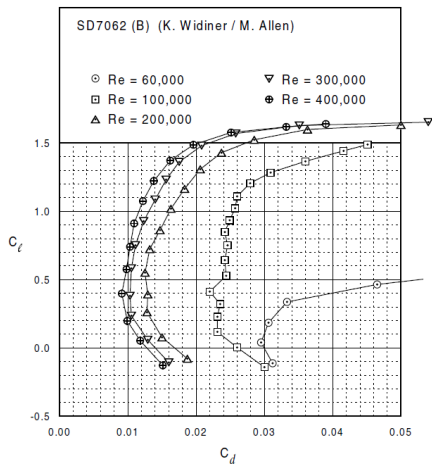


Figure B.5

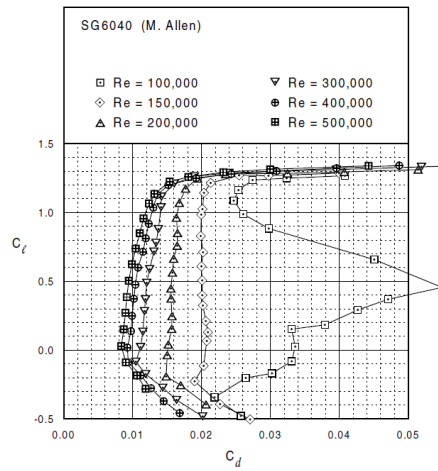


Figure B.6

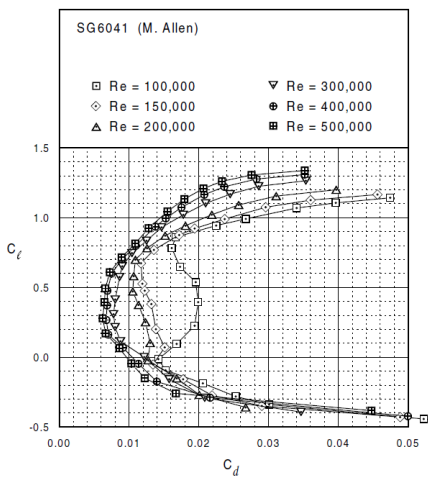


Figure B.7

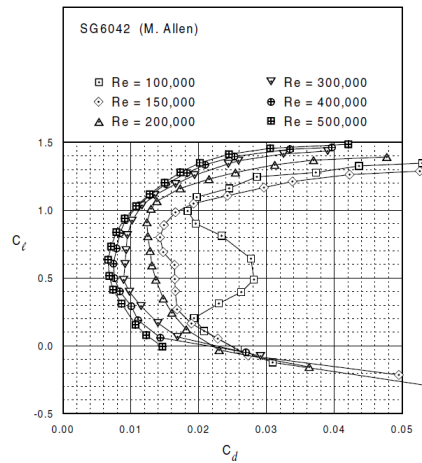


Figure B.8

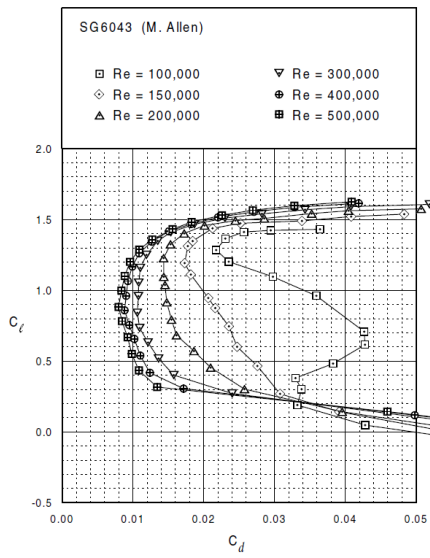


Figure B.9

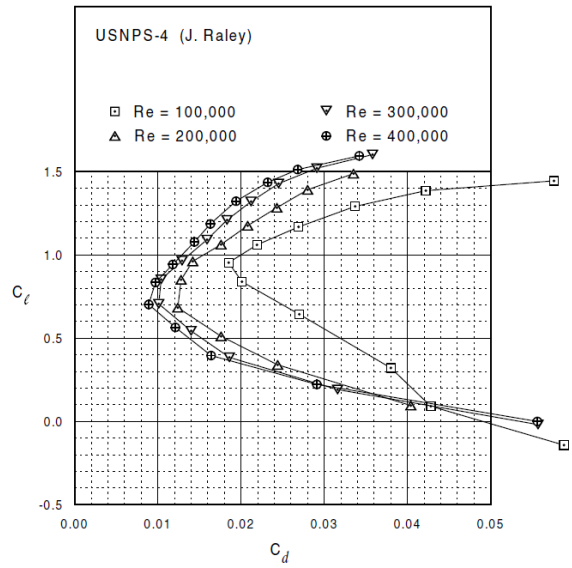


Figure B.10

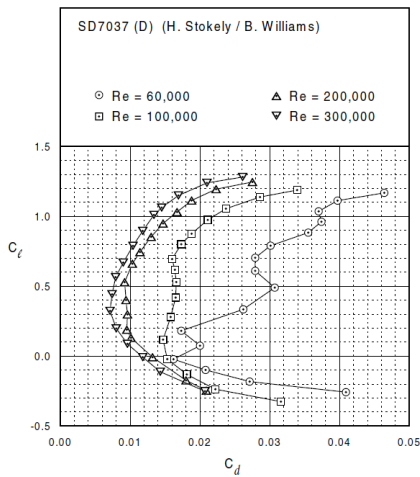


Figure B.11

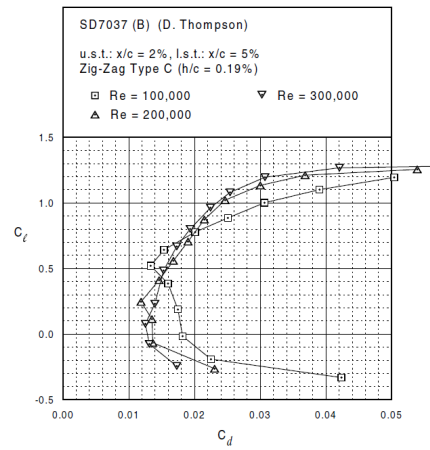


Figure B.12

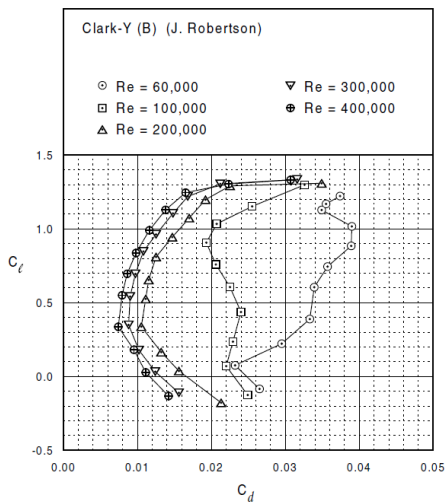


Figure B.13

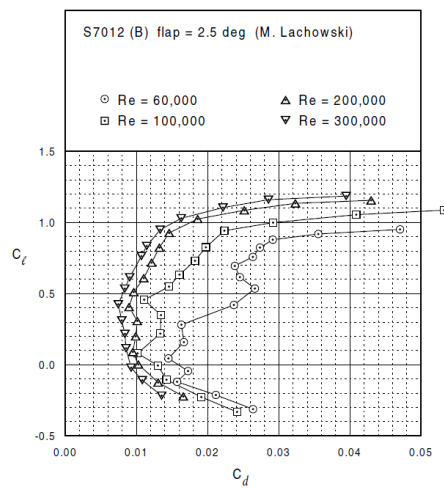


Figure B.14

Appendix C

SD7037 Selig Polar File

QBlade v0.8 on XFLR5 v6.06

Empirical polar for: SD7037

1 1 Reynolds number fixed Mach number fixed

xtrf = 0.02 (top) 0.05 (bottom)

Mach = 0.000

Re = 0.100 e 6 Ncrit = 9.000

alpha	CL	CD	CDp	Cm
-4.000	-0.3000	0.04200	0.04200	-0.0600
-3.000	-0.2000	0.02200	0.02200	-0.0600
-2.000	0.0000	0.01800	0.01800	-0.0600
0.000	0.2000	0.01750	0.01750	-0.0800
2.000	0.4000	0.01600	0.01600	-0.0900
3.000	0.5000	0.01400	0.01400	-0.0800
4.000	0.6000	0.01500	0.01500	-0.0800
6.000	0.8000	0.02000	0.02000	-0.0700
8.000	0.9000	0.02500	0.02500	-0.0600
9.000	1.0000	0.03000	0.03000	-0.0600
11.000	1.1000	0.03900	0.03900	-0.0600
12.000	1.2000	0.05000	0.05000	-0.0500

Appendix D

Rotorblade Tables for Concept Rotors

The Matlab Design		
Radial position [m]	Chord Length [m]	Twist angle[deg]
20	20	64.4
30	84	48.2
40	90	40.2
50	91	33.8
60	89	28.8
70	85	24.8
80	81	21.5
90	76	18.8
100	72	16.6
110	67	14.7
120	63	13.1
130	60	11.8
140	56	10.6
150	53	9.5
160	50	8.6
170	47	7.8
180	44	7.0
190	41	6.4
200	38	5.8
210	35	5.2
220	31	4.7
230	26	4.3
240	18	3.8
250	0	3.5

The QBlade Design		
Radial position [mm]	Chord Length [mm]	Twist angle[deg]
20	20	64.4
30	84	48.2
40	90	40.2
50	91	33.8
60	89	28.8
70	85	24.8
80	81	21.5
90	76	18.8
100	72	16.6
110	68	14.7
120	64	13.1
130	60	11.8
140	57	10.6
150	54	9.5
160	51	8.6
170	49	7.8
180	47	7.0
190	44	6.4
200	43	5.8
210	41	5.2
220	39	4.7
230	38	4.3
240	36	3.8
250	35	3.5

APPENDIX D. ROTORBLADE TABLES FOR CONCEPT ROTORS

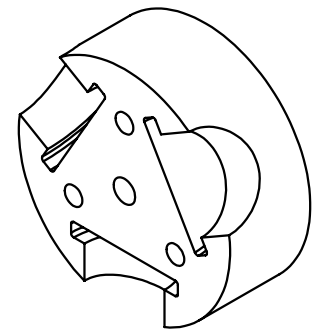
The Linear Chord		
Radial position [mm]	Chord Length [mm]	Twist angle[deg]
20	20	64.4
30	79	48.2
40	77	40.2
50	74	33.8
60	72	28.8
70	70	24.8
80	67	21.5
90	65	18.8
100	63	16.6
110	60	14.7
120	58	13.1
130	56	11.8
140	54	10.6
150	51	9.5
160	49	8.6
170	47	7.8
180	44	7.0
190	42	6.4
200	40	5.8
210	37	5.2
220	35	4.7
230	33	4.3
240	30	3.8
250	28	3.5

The Multi-Foil			
Radial position [mm]	Chord Length [mm]	Twist angle[deg]	Airfoil Type
20	20	64.4	NACA 3318
30	84	47.7	NACA 3318
40	90	39.7	NACA 3318
50	91	33.3	NACA 3315
60	89	27.8	NACA 3315
70	85	23.8	NACA 3315
80	81	20.5	NACA 3312
90	76	17.3	NACA 3312
100	72	15.1	NACA 3312
110	67	13.2	NACA 3312
120	63	11.6	SD7037
130	60	11.8	SD7037
140	56	10.6	SD7037
150	53	9.5	SD7037
160	50	8.6	SD7037
170	47	7.8	SD7037
180	44	7.0	SD7037
190	41	6.4	SD7037
200	38	5.8	SD7037
210	35	5.2	SD7037
220	31	4.7	SD7037
230	26	4.3	SD7037
240	18	3.8	SD7037
250	0	3.5	SD7037

The Final Concept		
Radial position [m]	Chord Length [m]	Twist angle[deg]
0.02	0.02	64.36
0.03	0.08	48.25
0.04	0.09	40.17
0.05	0.09	33.81
0.06	0.08	28.78
0.07	0.08	24.76
0.08	0.08	21.51
0.09	0.07	18.84
0.10	0.07	16.62
0.11	0.07	14.75
0.12	0.06	13.15
0.13	0.06	11.77
0.14	0.06	10.57
0.15	0.05	9.52
0.16	0.05	8.60
0.17	0.05	7.77
0.18	0.04	7.03
0.19	0.04	6.37
0.20	0.04	5.77
0.21	0.03	5.22
0.22	0.03	4.72
0.23	0.03	4.27
0.24	0.02	3.85
0.25	0.00	3.46

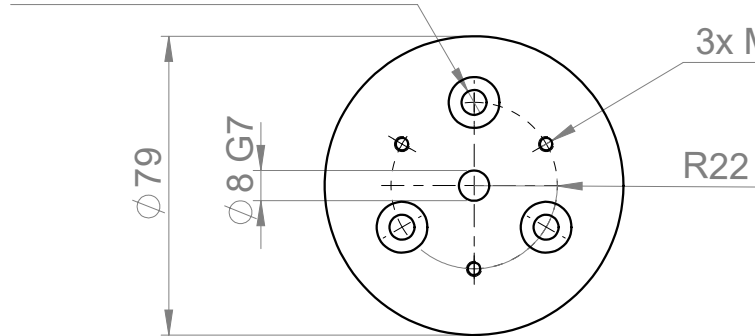
Appendix E

Technical Drawings

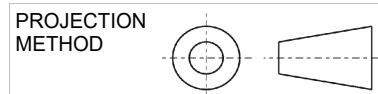
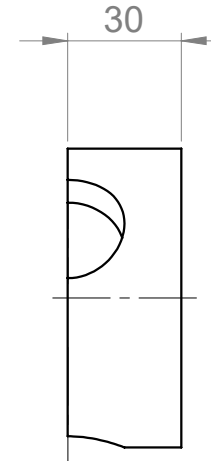
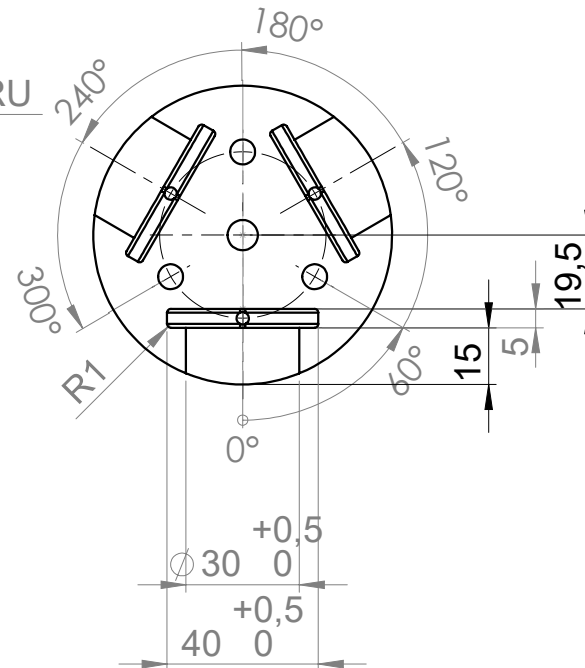


Back

3 x ∇ R3 X 90° THRU
+0.5
-0



Front



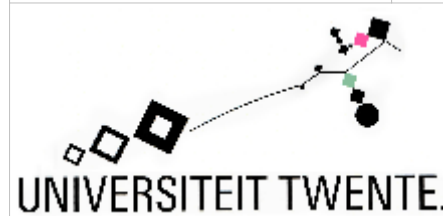
UNLESS STATED
OTHERWISE:
TOLERANCES $\pm 0,5$ MM

DRAWN
CHECKED

Cedric van Wijk

DATE
SCALE

3-2-2020
1:2



MATERIAL
Aluminium

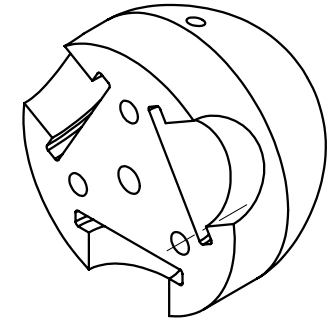
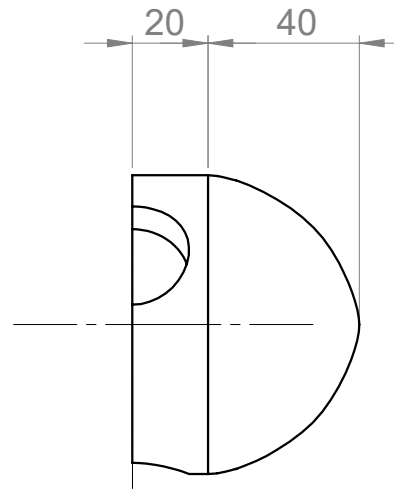
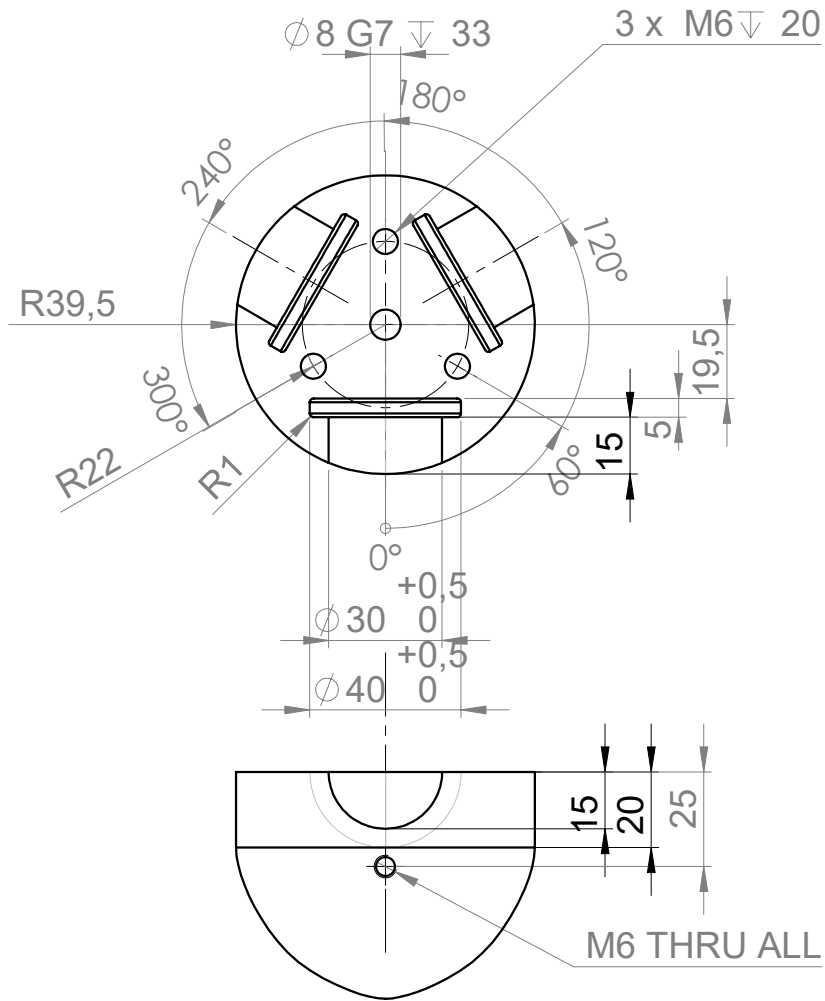
SURFACE FINISH

TITLE
Hub part 1

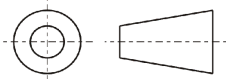
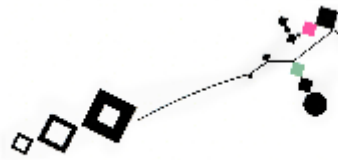
DRAWING NO.
R1

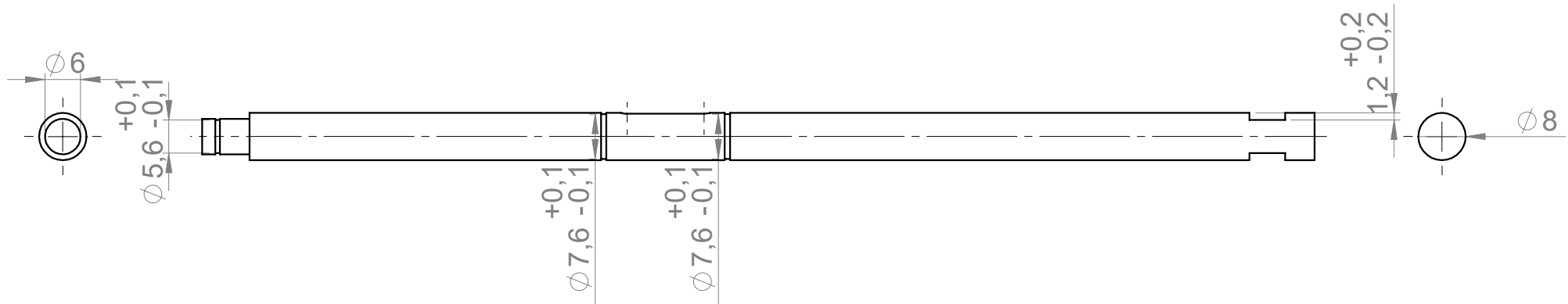
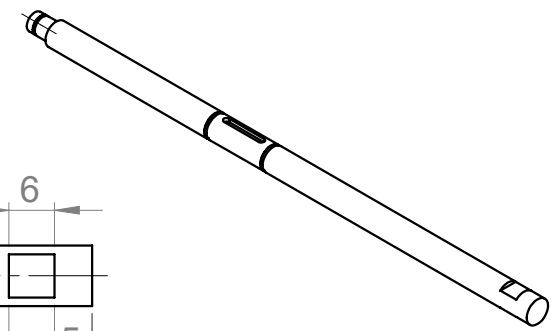
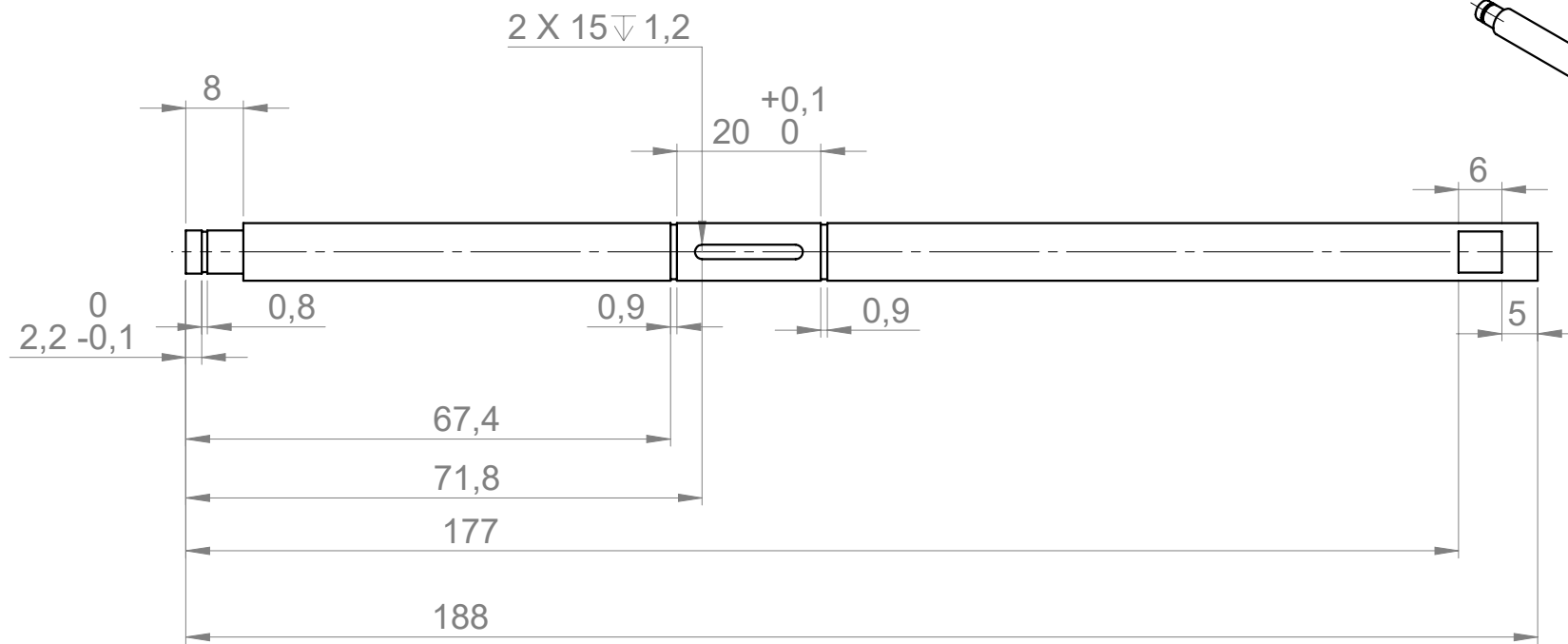
FILE / PART NAME
Bighub79-1.sldprt

REV.
02
A4

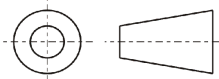
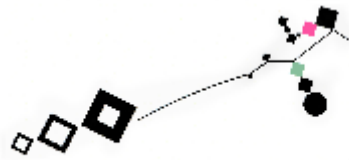


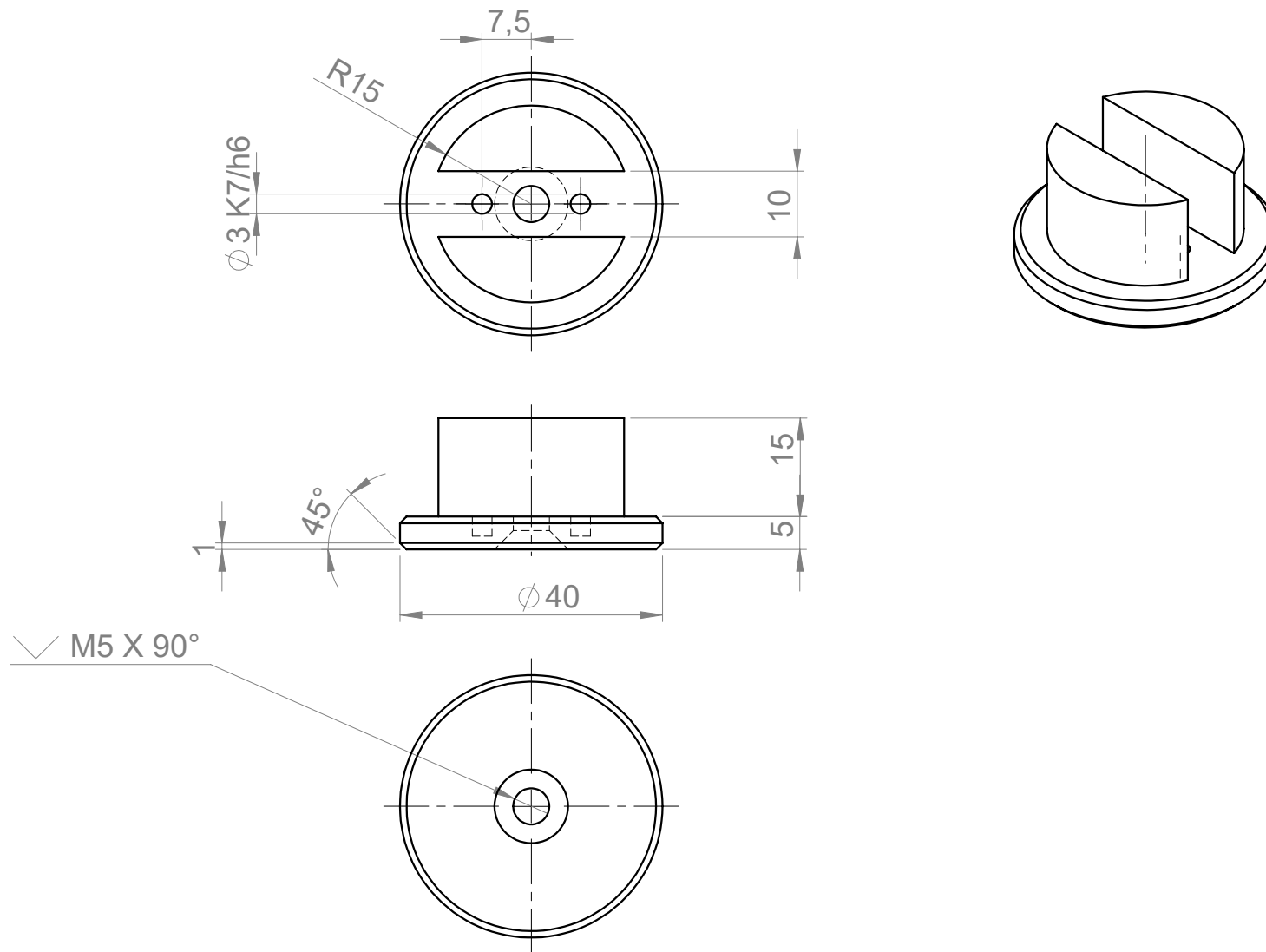
SCHERPE KANTEN BREKEN

PROJECTION METHOD 	UNLESS STATED OTHERWISE: TOLERANCES $\pm 0,5$ MM	DRAWN	Cedric van Wijk	DATE	3-2-2019			
		CHECKED		SCALE	1:2			
 UNIVERSITEIT TWENTE.	MATERIAL	Aluminium			TITLE	Hub part 2	REV.	03
	SURFACE FINISH				DRAWING NO.	R2		
			FILE / PART NAME	Bighub79-2.sldprt			A4	
FACULTY OF ENGINEERING		DIMENSIONS IN MILLIMETERS			SHEET 1 OF 1			



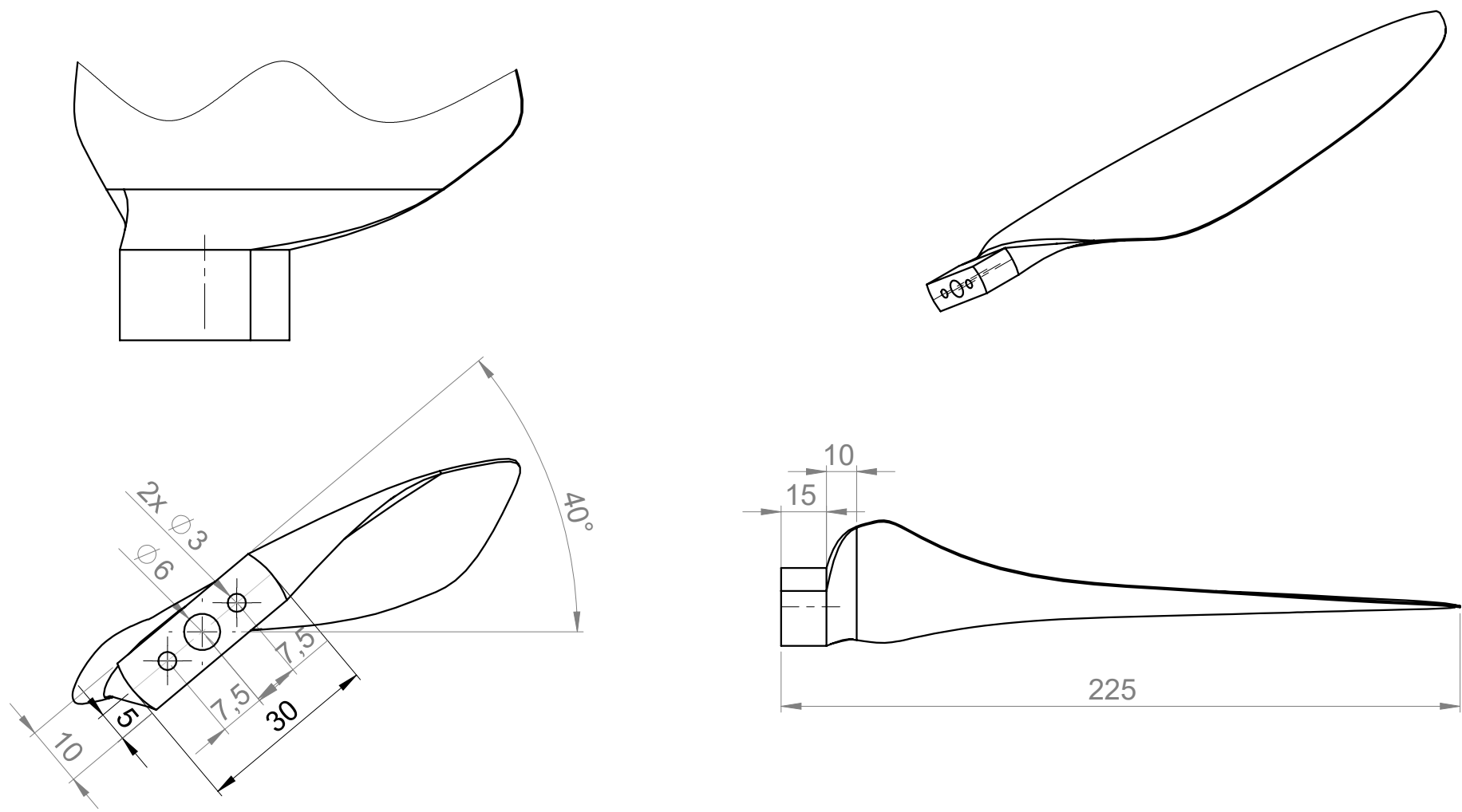
SCHERPE KANTEN BREKEN

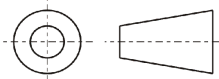
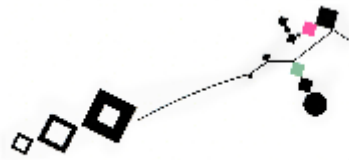
PROJECTION METHOD 	UNLESS STATED OTHERWISE: TOLERANCES $\pm 0,5$ MM	DRAWN Rowan van Wijk	DATE 08/01/20
		CHECKED	SCALE 1:1
 UNIVERSITEIT TWENTE.	MATERIAL Steel	TITLE Rotor Axle	
	SURFACE FINISH	DRAWING NO. N7	REV. 01
FACULTY OF ENGINEERING	DIMENSIONS IN MILLIMETERS	FILE / PART NAME Rotor Axle.SLDprt	SHEET 1 OF 1



SCHERPE KANTEN BREKEN

PROJECTION METHOD 	UNLESS STATED OTHERWISE: TOLERANCES $\pm 0,5$ MM	DRAWN	Cedric van Wijk	DATE	27-11-19
		CHECKED		SCALE	1:1
 UNIVERSITEIT TWENTE.	MATERIAL	TITLE			REV.
	Aluminium	Blade base			02
	SURFACE FINISH	DRAWING NO.			A4
	20191127-1				
FACULTY OF ENGINEERING		FILE / PART NAME			
		Bigbase			
DIMENSIONS IN MILLIMETERS				SHEET 1 OF 1	



PROJECTION METHOD 	UNLESS STATED OTHERWISE: TOLERANCES $\pm 0,5$ MM	DRAWN	Cedric van Wijk	DATE	3-3-20
		CHECKED		SCALE	1:1 & 1:2
 UNIVERSITEIT TWENTE.	MATERIAL	TITLE			REV.
	3D printed PA2200	Blade Root			01
	SURFACE FINISH	DRAWING NO. R5			A4
	FILE / PART NAME SWBlade_TEGap.sldprt				
FACULTY OF ENGINEERING	DIMENSIONS IN MILLIMETERS			SHEET 1 OF 1	

Appendix F

PA2200 Material properties

PA 2200 Performance 1.0

PA12

EOS GmbH - Electro Optical Systems

Product Texts

Product Texts

This whitish fine powder PA 2200 on the basis of polyamide 12 serves with its very well-balanced property profile a wide variety of applications. Laser-sintered parts made from PA 2200 possess excellent material properties:

- high strength and stiffness
- good chemical resistance
- excellent long-term constant behaviour
- high selectivity and detail resolution
- various finishing possibilities (e.g. metallisation, stove enamelling, vibratory grinding, tub colouring, bonding, powder coating, flocking)
- bio compatible according to EN ISO 10993-1 and USP/level VI/121 °C
- approved for food contact in compliance with the EU Plastics Directive 2002/72/EC (exception: high alcoholic foodstuff)

Typical applications of the material are fully functional plastic parts of highest quality. Due to the excellent mechanical properties the material is often used to substitute typical injection moulding plastics. The biocompatibility allows its use e.g. for prostheses, the high abrasion resistance allows e.g. the realisation of movable part connections.

100 µm layer thickness

Performance is the parameter set of choice for parts with high demands on mechanical properties and fracture behaviour, especially when the part is going to be subjected to multiaxial loading in all three directions. Performance parts are characterized by the highest degree of isotropic strength and rigidity. The choice of 100 µm layer thickness results in fine resolution and also very high surface quality and detail resolution.

Mechanical properties	Value	Unit	Test Standard
Izod Impact notched (23°C)	4.4	kJ/m ²	ISO 180/1A
Shore D hardness (15s)	75	-	ISO 868

3D Data	Value	Unit	Test Standard
The properties of parts manufactured using additive manufacturing technology (e.g. laser sintering, stereolithography, Fused Deposition Modelling, 3D printing) are, due to their layer-by-layer production, to some extent direction dependent. This has to be considered when designing the part and defining the build orientation.			
Tensile Modulus			ISO 527-1/-2
X Direction	1700	MPa	
Y Direction	1700	MPa	
Z Direction	1700	MPa	
Tensile Strength			ISO 527-1/-2
X Direction	50	MPa	
Y Direction	50	MPa	
Z Direction	50	MPa	
Strain at break			ISO 527-1/-2
X Direction	20	%	
Y Direction	20	%	
Z Direction	10	%	
Charpy impact strength (+23°C, X Direction)	53	kJ/m ²	ISO 179/1eU
Charpy notched impact strength (+23°C, X Direction)	4.8	kJ/m ²	ISO 179/1eA
Flexural Modulus (23°C, X Direction)	1500	MPa	ISO 178

Thermal properties	Value	Unit	Test Standard
Melting temperature (20°C/min)	176	°C	ISO 11357-1/-3
Vicat softening temperature (50°C/h 50N)	163	°C	ISO 306

Other properties	Value	Unit	Test Standard
Density (lasersintered)	930	kg/m ³	EOS Method
Powder colour (ac. to safety data sheet)	White	-	-

Appendix G

Wind Tunnel Test Data

v	Q	T	RPM	U	I	T	Patm	T_err	Q_err	Pmech	Pel	TSR
8,3	0,14	7,77	1635	12,9	1,18	17,4	99670			23,97	15,22	5,16
8,2	0,18	6,88	1250	9,04	1,94	18,1	99670			23,56	17,54	3,99
8,3	0,19	6,8	1185	8,3	2	17,8	99670			23,58	16,6	3,74
8,5	0,14	8,7	1700	13,5	1,22	18,9	99670	2		24,92	16,47	5,24
8,5	0,16	9,1	1870	15,1	0,9	18,5	99670	2		31,33	13,59	5,76
8,5	0,16	9,1	1990	16,5	0,72	18,1	99670	2		33,34	11,88	6,13
8,5	0,17	9	1940	16	0,8	18	99670	2		34,54	12,8	5,98
8,5	0,21	8,9	1805	14,5	1,04	17,9	99670	2		39,69	15,08	5,56
8,5	0,18	8,4	1580	12,15	1,48	17,9	99670	2		29,78	17,98	4,87
8,7	0,09	3,5	235	0,63	0,14	17,8	99670	2		2,21	0,088	0,71
8,8	0,04	1,1	230	0,6	0,12	17,3	99670			0,96	0,072	0,68
8,5	0,16	1,34	204	0,38	0,11	17,6	99670	1,3		3,42	0,042	0,63
8,5	0,19	6,4	1505	11,5	1,58	17,7	99670	1,3		29,94	18,17	4,64
8,5	0,21	6,93	1770	14,2	1,1	17,8	99670	1,3		38,92	15,62	5,45
8,5	0,2	7,2	1900	15,5	0,8	17,8	99670	1,3		39,79	12,4	5,85
8,4	0,18	6,95	1980	16,5	0,72	17,8	99670	1,3		37,32	11,88	6,17
8,4	0,21	6,95	1850	15	0,95	17,8	99670	1,3		40,68	14,25	5,77
8,5	0,2	6,7	1665	13,1	1,3	17,8	99670	1,3		34,87	17,03	5,13
8,5	0,21	5,95	1300	9,4	2,06	17,8	99670	1,3		28,59	19,36	4,00
11,11	0,3	13,1	2090	15,7	2,99	17,6	99670	0,7	0,05	65,66	46,94	4,92
11,1	0,36	12,63	1970	14,3	3,3	17,7	99670	0,7	0,05	74,27	47,19	4,65
11,2	0,45	12,45	1840	12,9	3,7	17,7	99670	0,7	0,05	86,71	47,73	4,30
11,1	0,49	12,2	1735	11,7	4	17,7	99670	0,7	0,05	89,03	46,8	4,09
11,2	0,47	11,95	1612	10,3	4,3	17,7	99670	0,7	0,05	79,34	44,29	3,77
11,2	0,22	13,2	2300	18,2	2,1	17,7	99670	0,7	0,05	52,99	38,22	5,38
11,1	0,21	13	2410	19,3	1,98	17,7	99670	0,7	0,05	53,00	38,21	5,68
11,2	0,2	13,2	2450	20	1,85	17,7	99670	0,7	0,05	51,31	37	5,73
11,2	0,18	12,6	2590	21,5	1,6	17,7	99670	0,7	0,05	48,82	34,4	6,05
11,2	0,15	13	2750	22,8	1,2	17,7	99670	0,7	0,05	43,20	27,36	6,43
11,2	0,12	13,3	2720	23,5	1,25	17,3	99670	0,7	0,05	34,18	29,38	6,36
11,1	0,17	13,1	2460	19,8	1,88	17,7	99670	0,7	0,05	43,79	37,22	5,80
11,1	0,145	13,4	2620	21,5	1,53	17,9	99670	0,7	0,05	39,78	32,9	6,18
11,1	0,19	12,95	2350	18,7	2,11	18	99670	0,7	0,05	46,76	39,46	5,54
11,1	0,28	13,18	2040	15,1	2,88	18	99670	0,7	0,05	59,82	43,49	4,81
11,1	0,22	13,3	2210	17	2,45	18,1	99670	0,7	0,05	50,91	41,65	5,21
11,1	0,37	13,1	1950	14,1	3,17	18,1	99670	0,7	0,05	75,56	44,7	4,60
11,2	0,42	12,8	1845	12,8	3,5	18,2	99670	0,7	0,05	81,15	44,8	4,31
11,2	0,44	12,1	1750	11,95	3,8	18,2	99670	0,7	0,05	80,63	45,41	4,09
11,1	0,43	11,9	1610	10,4	4,2	18,2	99670	0,7	0,05	72,50	43,68	3,80
11,5	0,07	4,5	380	1,7	0,67	18,2	99670	0,7	0,05	2,79	1,139	0,87
11,1	0,43	12,15	1795	12,5	3,6	18,3	99670	0,7	0,05	80,83	45	4,23
11,1	0,46	12,1	1830	13	3,48	18,3	99670	0,7	0,05	88,15	45,24	4,32
11,1	0,45	12,5	1865	13,3	3,4	18,3	99670	0,7	0,05	87,89	45,22	4,40
9,6	0,36	10,04	1634	12,2	2,3	17,9	99670			61,60	28,06	4,46

9,6	0,3	11,5	1975	15,5	1,5	17,9	99670		62,05	23,25	5,39	
9,6	0,17	10,7	2180	18	1,08	18	99670		38,81	19,44	5,95	
9,6	0,15	10,98	2300	19,6	0,85	18	99670		36,13	16,66	6,27	
9,6	0,36	10,2	1640	12,1	2,3	17,9	99670		61,83	27,83	4,47	
9,6	0,33	9,8	1560	11,3	2,52	17,9	99670		53,91	28,48	4,25	
9,6	0,34	9,8	1463	10,2	2,75	17,9	99670		52,09	28,05	3,99	
9,8	0,21	7,2	800	5	1,32	18	99670		17,59	6,6	2,14	
9,6	0,35	9,4	1420	9,75	2,8	18	99670		52,05	27,3	3,87	
9,6	0,37	10	1610	11,7	2,39	18	99670		62,38	27,96	4,39	
9,6	0,36	10,6	1830	14,2	1,78	18	99670		68,99	25,28	4,99	
9,6	0,18	11	2095	16,75	1,25	18	99670		39,49	20,94	5,71	
9,6	0,15	11,1	2230	19	0,95	18	99670		35,03	18,05	6,08	
9,6	0,15	11,15	2310	19,25	0,85	18	99670		36,29	16,36	6,30	
12,5	0,35	17,7	2424	18,3	3,48	18,1	99670		88,84	63,68	5,08	
12,6	0,3	17,55	2700	21	2,73	18,2	99670		84,82	57,33	5,61	
12,6	0,31	17,5	2580	19,5	3,6	18,2	99670		83,75	70,2	5,36	
12,6	0,37	17,41	2363	17,6	3,7	18,3	99670		91,56	65,12	4,91	
12,5	0,35	17,3	2430	18,05	3,52	18,3	99670		89,06	63,54	5,09	
12,5	0,38	17,2	2300	16,3	3,9	18,3	99670		91,53	63,57	4,82	
12,5	0,41	17,2	2200	15,5	4,2	18,3	99670		94,46	65,1	4,61	
12,5	0,47	16,8	2060	14	4,7	18,3	99670		101,39	65,8	4,31	
12,6	0,6	16,5	2000	13	5	18,4	99670		125,66	65	4,16	
12,6	0,64	15,4	1860	11,5	5,4	18,4	99670		124,66	62,1	3,86	
12,6	0,62	15,5	1750	10,4	5,8	18,4	99670		113,62	60,32	3,64	
13	0,12	4,6	350	1,3	0,8	18,4	99670		4,40	1,04	0,70	
12,6	0,63	15,5	1730	10,4	5,65	18,4	99670		114,13	58,76	3,59	
							99670					
13,9	0,46	20,85	2610	18,5	4,95	18,5	99670	0,88	0,02	125,73	91,58	4,92
13,9	0,43	21,1	2680	19,2	4,6	18,8	99670	0,88	0,02	120,68	88,32	5,05
13,9	0,42	20,86	2730	19,5	4,4	18,5	99670	0,88	0,02	120,07	85,8	5,14
13,9	0,5	20,7	2500	16,8	5,2	18,5	99670	0,88	0,02	130,90	87,36	4,71
13,9	0,5	20,9	2470	16,4	5,5	18,5	99670	0,88	0,02	129,33	90,2	4,65
13,9	0,52	21	2380	15,2	5,95	18,5	99670	0,88	0,02	129,60	90,44	4,48
13,9	0,58	20,3	2240	14	6,4	18,5	99670	0,88	0,02	136,05	89,6	4,22

Appendix H

Matlab Code for Preliminary Blade Design

```
1 clc
2 clear all
3 close all
4
5 set(0,'DefaultAxesXGrid','on','DefaultAxesYGrid','on')
6 set(0,'DefaultAxesFontSize',14)
7 set(0,'DefaultLineLineWidth',4);
8
9 %environmental parameters
10 rho = 1.208; %kg/m^3 at 15.5 C
11 mu = 1.825 * 10^(-5); %kg/ms
12
13 %Set TSR
14 TSR = 4;
15
16 %lift & drag coefficient at AoA
17 alpha = 6;
18 c_l = 0.8;
19 c_d = 0.02;
20
21 %Number of blades
22 B = 3;
23
24 %operating wind speed
25 U_wind = 40/3.6; %m/s
26
27
28 %dr blade element length, minimum and maximum blade length
29 dr = 0.0005;
30 rmin = 0.04;
31 rmax = 0.25; %blade radius
32
33 r = rmin:dr:rmax;
34
35
36 %velocity of blade element
37 U = TSR*(r./rmax) .* U_wind; %m/s
38 w = (TSR*U_wind)/rmax; %rad/s
39
40 % Maximum operating conditions
41 Umax_wind = 90/3.6; %m/s
42 Umax = TSR*(r./rmax) .*Umax_wind;%m/s
43 wmax =(3000*2*pi)/60; %rad/s %Brake at 3000 rpm!! %TSR*Umax_wind/rmax;%=without
brake
44
45 %calculate twist
46 phi_Betz = atand(2./(3.*TSR.*(r./rmax))); %deg
47 phi_Schmitz = (2./3).*atand(1./(TSR.*(r./rmax))); %deg
48 phi = phi_Betz;%deg
```

```

49
50 twist_Betz = phi_Betz-alpha;%deg
51 twist_Schmitz = phi_Schmitz-alpha;%deg
52 twist = phi-alpha;%deg
53
54 p = (polyfit(r,twist,1)); %linear approximation of twist_schmitz
55 twist_lin = p(1).*r+p(2); %Linear fuction of p
56
57 %Calculate Prandtl tip loss factor
58 F_tip = (2./pi).*(acos(exp((-((B./2).*(1-(r./rmax)))./(r./rmax).*sind(
(phi))))));
59 F_root=(2./pi) .* acos(exp((-B./2)).*abs(((r-rmin)./(r.*sind(phi))))));
60 F_tip=F_tip.*F_root;
61
62
63 %Calculate Betz & Schmitz chord lengths
64 C_betz = ((8.*pi.*r.*sind(phi_Betz))./(3.*B.*c_1.*TSR.*(r./rmax))).*F_tip;
65 C_schmitz = ((16.*pi.*r)./(B.*c_1)).*(sind((1./3).*atand(rmax./(TSR.*r))).^2)).
*F_tip;
66
67 % p = (polyfit(r,C_schmitz,1));
68
69 p= [-0.3341 0.1032];
70 C_lin = p(1).*r+p(2);
71
72 %airfoil max chord thickness at each element
73 max_thickness = 0.092 ; %!airfoil porperty
74 dt = max_thickness.*C_schmitz;
75
76 %estimated blade volume & weight
77 V = sum(0.7.*C_schmitz.*dt.*dr); %assume square of 70% chord length and height =
max thickness
78 rho_alu = 2700; %kg/m^3
79 m_alu = V*rho_alu;
80 rho_polyamide = 820.6; %kg/m^3
81 % m_polyamide = V*rho_polyamide;
82 m_polyamide = 43*10^(-3);
83 %relative velocity
84 U_rel = U./cosd(phi);
85
86 %Reynolds number
87 Re = (rho.*U_rel.*C_schmitz)./(mu);
88
89 %Betz limit optimals:
90 a=1/3;
91 a_p = (1-3*a)/(4*a-1);
92 CPBetz = 4*a*(1-a)^2; % = Betz limit
93
94 %Optimal TSR

```

```
95 TSRmin = 0;
96 TSRmax = 15;
97 TSR2 = (TSRmin:0.1:TSRmax);
98
99 %calculate CP optimal
100 CR = c_l/c_d;
101 A1 = ((1-(0.416./(B.*TSR2))).^2);
102 B1 = (exp(-0.35./(TSR2.^1.29)))-TSR2.*(1/CR);
103 CPopt = CPBetz.*(A1.*B1);
104
105 CPmax = max(CPopt);
106 [CPh,idx1] = max(CPopt);
107 TSROpt = TSR2(idx1);
108
109
110 %Calculation of forces
111 %area of elements and forces on elements
112 dA = C_schmitz*dr;
113
114
115 dFL = (1/2).*rho.*U_rel.^2.*dA.*c_l;
116 dFD = (1/2).*rho.*U_rel.^2.*dA.*c_d;
117 dFT = dFL.*cosd(phi)+dFD.*sind(phi);
118 dFM = dFL.*sind(phi)-dFD.*cosd(phi);
119
120 %Calculate total forces on blade
121 FL = sum(dFL);
122 FD = sum(dFD);
123 FT = sum(dFT);
124 FM = sum(dFM);
125
126 %Moment and power on elements
127 dM = r.*dFM;
128 dP = w.*dM;
129
130 %Total moment and power
131 M = sum(dM);
132 P = sum(dP);
133 P_rot = P*B;
134 A_rotor = pi*rmax^2;
135 Cp = P_rot/(0.5*rho*A_rotor*U_wind^3);
136
137 %Centrifugal forces
138 F_centrifugal_alu = m_alu * w^2 *(rmax/2);
139 Fmax_centrifugal_alu = m_alu * wmax^2 *(rmax/2);
140
141 F_centrifugal_polyamide = m_polyamide * w^2 *(rmax/2);
142 Fmax_centrifugal_polyamide = m_polyamide * wmax^2 *0.10515;
143
```

```
144 %Calculate shear tension
145 Droot = 0.02;%
146 hbase = 0.003;%
147 shear_alu = F_centrifugal_alu/(pi*Droot*hbase);
148 shearmax_alu = Fmax_centrifugal_alu/(pi*Droot*hbase);
149
150 shear_polyamide = F_centrifugal_polyamide/(pi*Droot*hbase);
151 shearmax_polyamide = Fmax_centrifugal_polyamide/(pi*Droot*hbase);
152
153 %Bending stress
154 %assume rectangle of dt*0.7*c for cross-sectional area
155 C=C_schmitz; %Choose which chord distribution to use (C_schmitz, C_lin, C_betz)
156
157 C=0.7*C;
158 Arotor = pi*rmax^2;%m^2
159
160 Fwind = (1/2)*rho*Umax_wind^2*Arotor;%N
161
162 Fwindblade = ((1/3)*(Fwind/Arotor));%N/m divided load
163 Fwindlblade = (1/3)*Fwind;%N
164
165 Fy = Fwindlblade;%N
166 M0 = Fwindlblade*(1/2)*rmax;%Nm
167
168 V_line = Fy-(Fwindlblade/rmax)*r;
169 M_line = Fy*r-(Fwindlblade)/(2*rmax)*r.^2 -M0;
170
171 I_rot = (C.*dt)./12.*(dt.^2.*cosd(twist).^2+(C).^2.*sind(twist).^2); %Rotating ↵
blade, variable in thickness and length
172 I_rad = (1/12).*(C).*dt.^3; %Non-rotating, but variable thickness and width over ↵
radius
173 I_avg = (1/12)*mean(C)*mean(dt)^3;% non-rotating average thickness and height)
174
175 cy_rot = (dt.*cosd(twist)+C.*sind(twist))/2;
176 cy = (1/2)*dt;
177 E_alu = 69*10^9;
178 E_polyamide = 2.5*10^9;
179
180 I = I_rad; % Choose which I to use for stress calculation
181
182 if I == I_rot
183     cy = cy_rot;
184 elseif I == I_avg
185     cy = (1/2).*mean(dt);
186 end
187
188 sigma = (abs(M_line).*cy)./I;
189 sigma_max = max(sigma)';
190
```

```

191 figure
192 hold on
193 plot(r,sigma/1000000)
194 xlabel('Blade radius [m]')
195 ylabel('Stress [MPa]')
196 title('Bending stress')
197
198
199 %calculate deflection with variable I
200 %I_rot function approximated by Excel and integrated using Wolfram Alpha:
201 %I = 1E-7exp(-33.11*r)
202 %I = f*exp*(b*r)
203 % f = 1E-7;
204 % b = -33.11;
205
206 E = E_polyamide; %Elastic modulus of chosen material
207 L = rmax-rmin; %Beam length
208 % %C1 at r = 1, theta = 0
209 % % C1 = -(Fwindlblade *(-2 + 2M *b *L + b^2 *L^2 - 2 *b* 0 + 2* b^2 *L *0 - b^2 *
*0^2))/(2 *a *b^3 *exp(b *0) *L *E);
210 % C1 = -(Fwindlblade *(-2 + 2 *b *L + b^2 *rmax^2))/(2 *a *b^3 *L *E)
211 % %C2 at r=0, delta = 0
212 % % C2 = (-6 *Fwindlblade + 4 *b *Fwindlblade *L+ b^2 *Fwindlblade *L^2 - 4 *b *
*Fwindlblade *0 + 2 *b^2 *Fwindlblade *rmax *0 - b^2 *Fwindlblade *0^2 - 2 *a *b^4 *
*C1 *exp(b *0) *L *0 *E)/(2 *a *b^4 *exp(b *0) *L *E);
213 % C2 = (Fwindlblade *(-6 + 4 *b *L + b^2 *L^2))/(2 *a *b^4 *L *E)
214 % % calculate deflection delta at L
215 % delta_rot = C1 *L + (Fwindlblade *(6 - 4 *b *(L - L) + b^2 *(-L^2 - 2 *L *L +
L^2)))/(2 *a *b^4 *exp(b *L) *L*E) +C2
216
217
218 delta_avg = (Fwindblade*L^4)/(8*E*I_avg);
219
220 %Plots
221 %
222 figure
223 hold on
224 plot(r,twist_Betz);
225 plot(r, twist_Schmitz);
226 title('Twist distribution')
227 xlabel('Blade radius [m]')
228 ylabel('Twist angle [°]')
229 legend('Betz','Schmitz')
230
231 figure
232 hold on
233 plot(r, C_betz)
234 plot(r, C_schmitz)
235 plot(r, C_lin)

```

```

236 title('Chord distribution')
237 xlabel('Blade radius [m]')
238 ylabel('Chord length [m]')
239 legend('Betz','Schmitz','Schmitz, linear')
240
241 % %QBlade and matlab comparison
242 % c_schmitz_QB = [2.00E+03 8.40E+03 8.99E+03 9.07E+03 8.85E+03 8.48E+03 8.06E+03 ↵
7.61E+03 7.18E+03 6.77E+03 6.38E+03 6.03E+03 5.71E+03 5.41E+03 5.14E+03 4.89E+03 4.66 ↵
E+03 4.45E+03 4.26E+03 4.08E+03 3.91E+03 3.76E+03 3.62E+03 3.48E+03].*10^(-5);%
243 % r_QB = [2.00E+03 3.00E+03 4.00E+03 5.00E+03 6.00E+03 7.00E+03 8.00E+03 9.00E+03 ↵
1.00E+04 1.10E+04 1.20E+04 1.30E+04 1.40E+04 1.50E+04 1.60E+04 1.70E+04 1.80E+04 1.90 ↵
E+04 2.00E+04 2.10E+04 2.20E+04 2.30E+04 2.40E+04 2.50E+04 ].*10^(-5);
244 % twist_QB = [6.44E+06 4.82E+06 4.02E+06 3.38E+06 2.88E+06 2.48E+06 ↵
2.15E+06 1.88E+06 1.66E+06 1.47E+06 1.31E+06 1.18E+06 1.06E+06 ↵
9.52E+05 8.60E+05 7.77E+05 7.03E+05 6.37E+05 5.77E+05 5.22E+05 ↵
4.72E+05 4.27E+05 3.85E+05 3.46E+05].*10^(-5);
245 %
246 % figure
247 % hold on
248 % plot(r, C_schmitz)
249 % plot(r_QB, c_schmitz_QB)
250 % title('Chord distribution')
251 % xlabel('Blade radius [m]')
252 % ylabel('Chord length [m]')
253 % legend('Schmitz BEM','Schmitz QBlade')
254 %
255 % figure
256 % hold on
257 % plot(r,twist_Betz);
258 % plot(r_QB,twist_QB)
259 % title('Twist distribution')
260 % xlabel('Blade radius [m]')
261 % ylabel('Twist angle [°]')
262 % legend('Betz BEM','QBlade')
263 % % ↵
----- ↵
-----
264
265 figure
266 area(r, (dP/dr))
267 title('Total Power')
268 xlabel('Element position on blade radius [m]')
269 ylabel('power per element [w/m]')
270
271 figure
272 hold on
273 plot(r,dFL/dr)
274 plot(r,dFD/dr)
275 plot(r,dFT/dr)

```

```
276 plot(r,dFM/dr)
277 hold off
278 ylim([0 140])
279 title('Forces on rotor blade')
280 xlabel('Element position on blade radius [m]')
281 ylabel('Force per blade element [N/m]')
282 legend('dF_L','dF_D','dF_T','dF_M')
283
284 figure
285 plot(r, Re)
286 title('Reynolds numbers along radius')
287 xlabel('blade radius [m]')
288 ylabel('Reynolds number [-]')
289 grid on
290
291 figure
292 plot(r,V_line)
293 title('Shear line')
294 xlabel('blade radius [m]')
295 ylabel('internal shear force [N]')
296
297 figure
298 plot(r,M_line)
299 title('Moment line')
300 xlabel('blade radius [m]')
301 ylabel('internal bending moment [Nm]')
302 set(gca,'XMinorTick','on','YMinorTick','on')
303
```

Appendix I

Matlab Code for Rotor Performance Predictions

```
1 clc
2 clear all
3 close all
4
5 set(0,'DefaultAxesXGrid','on','DefaultAxesYGrid','on')
6 set(0,'DefaultAxesFontSize',14)
7 set(0,'DefaultLineLineWidth',4);
8 % set(groot,'defaultFigureUnits','normalized')
9 % set(groot,'defaultFigurePosition',[0 0 1 1])
10
11 %Blade design Parameters
12 rmin = 0.04;
13 rmax = 0.25;
14 TSR_opt = 4;
15 B = 3;
16 alpha_opt = 6;
17 c_l_opt = 0.8;
18 U_wind_opt = 40/3.6;
19
20
21 %Blade design function
22 [phi, C, twist, r, dr] = BladeShape(rmin,rmax,TSR_opt,B,alpha_opt,c_l_opt,U_wind_opt);
23
24 %Operation Parameters
25 U_wind = 40/3.6;
26 TSR = 4;
27 pitch = 0;
28
29 %Remove last point of r,c because C= gives problems
30 r(end) = [];
31 C(end) = [];
32
33 %Use Prandtl Tip and/or root loss factor? 1 = yes 0 = no
34 TipLoss = 0;
35 RootLoss = 0;
36
37 varyTSR = 1; % Set VaryTSR to 1 or 0
38 TSRmin = 1; % minimal TSR to be tested
39 dTSR = 0.05; % Step size
40 TSRmax = 8; % Maximal TSR to be tested
41
42
43 varyPitch = 1; % Set VaryPitch to 1 or 0
44 Pitchmin = -10; % minimal Pitch angle to be tested
45 dPitch = 1; % Step size
46 Pitchmax = 20; % Maximal Pitch angle to be tested
47
48 varyWind = 1; % Set VaryWind to 1 or 0
```

```
49 U_windmin = 5;    % minimal Wind velocity to be tested
50 dU_wind = 1;     % Step size
51 U_windmax = 30;  % Maximal Wind Velocity to be tested
52
53 RF = 0.35;
54
55 if varyTSR == 1
56 [X, Y, Z] = VaryTSR(TSRmin, dTSR, TSRmax, C, twist, rmin, rmax, RF, U_wind, r, B , dr , TSR , TipLoss ,RootLoss, pitch);
57 end
58
59 if varyPitch == 1
60 [X, Y, Z] = VaryPitch(Pitchmin, dPitch, Pitchmax, C, twist, rmin, rmax, RF, U_wind, TSR, r, B, dr, TipLoss ,RootLoss);
61 end
62
63 if varyWind == 1
64 [X, Y, Z] = VaryWind(U_windmin, dU_wind, U_windmax, C, twist, rmin, rmax, RF, U_wind, TSR, r, B, dr, TipLoss ,RootLoss, pitch);
65 end
```

```
1
2 function [phi, C, twist, r, dr] = BladeShape(rmin,rmax,TSR,B,alpha,c_l,U_wind)
3
4 %enviromental parameters
5 rho = 1.208; %kg/m^3 at 15.5 C
6 mu = 1.825 * 10^(-5); %kg/ms
7
8 %dr blade element length, minimum and maximum blade length
9 dr = 0.0001;%(0.25-0.04)/19;
10 w = (TSR*U_wind)/rmax; %rad/s
11 r = rmin:dr:rmax;
12
13
14 %velocity of blade element
15 U = TSR*(r./rmax) .* U_wind; %m/s
16 w = (TSR*U_wind)/rmax; %rad/s
17
18 %calculate twist
19 phi_Betz = atand(2./(3.*TSR.*(r/rmax))); %deg
20 phi_Schmitz = (2./3).*atand(1./(TSR.*(r./rmax))); %deg
21 phi = phi_Betz;%deg
22
23 twist_Betz = phi_Betz-alpha;%deg
24 twist_Schmitz = phi_Schmitz-alpha;%deg
25 twist = phi-alpha;%deg
26
27 %Calculate Prandtl tip loss factor
28 F_tip = (2./pi).*(acos(exp((-B./2))*(((rmax-r)./(r.*sind(phi))))));
29
30
31 %Calculate Betz & Schmitz chord lengths
32 C_betz = (((8.*pi.*r.*sind(phi_Betz))./(3.*B.*c_l.*TSR.*(r./rmax)))).*F_tip;
33 C_schmitz = (((16.*pi.*r)./(B.*c_l)).*(sind((1./3).*atand(rmax./(TSR.*r))).^2)).*
34 *F_tip;
35 C = C_schmitz;
36
37 end
```

```

1 function [X, Y, Z] = VaryTSR(TSRmin, dTSR, TSRmax, C, twist, rmin, rmax, RF, U_
U_wind, r, B, dr, TSR, TipLoss, RootLoss, pitch)
2
3 k=0;
4 TSR2 = TSR;
5 twist2 = twist - pitch;
6
7
8 for TSR2 = TSRmin:dTSR:TSRmax
9     k=k+1;
10
11 w = (TSR2*U_wind)/rmax; %rad/s
12
13
14 j=0;
15
16
17 for i = length(r):-1:1
18 a=0.3;
19 b=0.000001;
20 a_prev = 1;
21 b_prev = 1;
22 a_2prev = 0;
23 b_2prev=0;
24 Diff_a = 1;
25 Diff_b = 1;
26 j=0;
27 z=0;
28 %
29 while abs(a-a_prev) > 0.00001 && abs(b-b_prev) > 0.00001% && Diff_a>0.001 &&
Diff_b>0.001
30 Diff_a = abs((a-a_prev)/a_prev);
31 Diff_b = abs((b-b_prev)/b_prev);
32 j=j+1;
33     a_2prev = a_prev;
34     b_2prev=b_prev;
35     a_prev = a;
36     b_prev = b;
37
38 %     Phi = atand( ((1-a)./(1+b)).*((U_wind)./(r(i).*w)) );
39 Un     = U_wind*(1 - a);           % Normal velocity [m/s]
40 Ut     = w.*r(i).*(1 + b);       % Tangential velocity [m/s]
41 Urel   = sqrt(Un.^2 + Ut.^2);    % Relative velocity [m/s]
42 Phi    = atand(Un/Ut);
43
44 alpha  = Phi-twist2(i);           % Angle of Attack [deg]
45
46     c_l   = -0.0025.*alpha.^2 + 0.1122.*alpha + 0.1928; %lift coefficient
(polynomial approximation)

```

```

47     c_d      = 0.0004.*alpha.^2 - 0.0024.*alpha + 0.0173; %Drag coefficient (↵
"
48
49     if alpha>12                                     %Polynomial↵
approximation of high angle Cl and Cd
50         c_l=(alpha-12)*-(1.2/(90-12))+1.1792;
51     elseif alpha < -10
52         c_l = (alpha+10)*(1.2)/(90-12)-1.1792;
53     end
54
55     if alpha > 12 && c_l<0
56         c_l=0;
57     elseif alpha < -10 && c_l>0
58         c_l = 0;
59     end
60
61
62     c_x      = c_l.*sind(Phi)-c_d.*cosd(Phi);
63     c_y      = c_l.*cosd(Phi)+c_d.*sind(Phi);
64
65     if TipLoss == 1
66         F_tip= max((2/pi) *   acos(exp((-B/2))*(((rmax-r(i))/(r(i)*sind(Phi)))))), ↵
0.1);
67     elseif TipLoss == 0
68         F_tip = 1;
69     else
70         msgbox('ERROR! Set tip/root loss to 1 or 0');
71     end
72
73
74     if RootLoss == 1
75         F_root=max(((2/pi) *   acos(exp((-B/2))*abs((((r(i)-rmin)/(r(i)*sind ↵
(Phi))))))))), 0.1);
76     elseif RootLoss == 0
77         F_root = 1;
78     else
79         msgbox('ERROR! Set tip/root loss to 1 or 0');
80     end
81     F=F_tip*F_root;
82
83
84     sigma = (C(i)*B) / (2*pi*r(i));
85
86     if sind(Phi) == 0
87         a = 1;
88     end
89
90
91     if a_prev <= 0.25

```

```
92     a         = 1./(((4.*F.*sind(Phi).^2)./(sigma.*c_y)) + 1);
93     else
94         K = (4.*F.*sind(Phi).^2)./(sigma.*c_y);
95         a_c=0.2;
96         a = .5.*(2 + K.*(1 - 2.*a_c) - sqrt(abs((K.*(1 - 2.*a_c) + 2).^2 + 4.*(K.*
*a_c.^2 - 1)))));
97     end
98
99
100    if j <10
101        a = a;
102    elseif j <11
103        a = 0.25.*a + 0.5.*a_prev + 0.25.*a_2prev;
104    else
105        a = RF.*a + (1 - RF).*a_prev;
106    end
107    TSRr = (TSR2/rmax)*r(i);
108    b     = 0.5.*(sqrt(abs(1 + 4./TSRr.^2.*a.*(1 - a))) - 1);
109
110
111
112    if j>10000
113        break
114    end
115 end
116
117    PHI(i) = Phi;
118    A(i) = a;
119    B2(i) = b;
120    CL(i) = c_l;
121    CD(i) = c_d;
122    ALPHA(i) = alpha;
123    FF(i) = F;
124    SIGMA(i) = sigma;
125 %     KK(i) = K
126 end
127
128 %Calculation of forces
129
130 %enviromental parameters
131 rho = 1.225; %kg/m^3 at 15.5 C
132 mu = 0.00001647; %kg/ms
133
134
135 U = w.*r.*(1+B2);
136 V = U_wind.*(1-A);
137 U_rel = sqrt(U.^2+V.^2);
138
139
```

```
140 %area of elements and forces on elements
141 dA = C*dr;
142
143
144 dFL = (1/2).*rho.*U_rel.^2.*dA.*CL;
145 dFD = (1/2).*rho.*U_rel.^2.*dA.*CD;
146 dFT = dFL.*cosd(PHI)+dFD.*sind(PHI);
147 dFM = dFL.*sind(PHI)-dFD.*cosd(PHI);
148
149 %Calculate total forces on blade
150 FL = sum(dFL);
151 FD = sum(dFD);
152 FT = sum(dFT);
153 FM = sum(dFM);
154
155 %Moment and power on elements
156 dM = r.*dFM;
157 dP = w.*dM;
158 %
159
160 %Total moment and power
161 M = sum(dM);
162 P = sum(dP);
163 P_rot = P*B;
164 A_rotor = pi*rmax^2;
165 T_rot = FT*B;
166 M_rot = M*B;
167
168 % figure(8)
169 % plot(r(1:length(r)),dM)
170
171 Cp(k) = P_rot/(0.5*rho*A_rotor*U_wind^3);
172 Ct(k) = T_rot/(0.5*rho*U_wind^2*A_rotor);
173 cq(k) = M_rot/(0.5*rho*rmax*U_wind^2*A_rotor);
174
175 P3(k)=P_rot;
176 M3(k)=M*B;
177 T3(k)=B*FT;
178
179 end
180 TSR2 = [TSRmin :dTSR: TSRmax];
181 X = figure();
182 %subplot(2,2,1);
183 hold on
184 plot(TSR2,Ct)
185 TSR_QBlade=[1 1.5 2 2.5 3 3.5 4 4.5 5 5.5 6 6.5 7 7.5 8];
186 if pitch == 0
187 T_QBlade=[3.84 5.09 6.34 7.87 9.28 9.87 10.44 10.65 10.71 ↵
10.76 11.15 11.51 12.38 11.88 9.26];
```

```
188 T_QBladeRF = [3.85  5.10  6.35  7.88  9.30  9.89  10.46  10.63  10.66 ↵
10.59  10.53  10.46  10.26  9.90  9.24];
189 Ct_QBlade = [2.59E-01  3.43E-01  4.27E-01  5.30E-01  6.26E-01  6.65E-01 ↵
7.03E-01  7.18E-01  7.22E-01  7.25E-01  7.52E-01  7.77E-01  8.35E-01 ↵
8.02E-01  6.25E-01];
190 Ct_QBladeRF = [0.259214 0.343633  0.427608  0.530709  0.626289  0.666089 ↵
0.704451  0.715785  0.717986  0.713366  0.709187  0.704876  0.690853 ↵
0.666747  0.622246];
191 end
192
193 plot(TSR_QBlade, Ct_QBlade)
194 plot(TSR_QBlade, Ct_QBladeRF)
195
196 legend('MatLab BEM', 'QBlade', 'Qblade RF = 0.1', 'Location', 'northwest')
197 xlabel('TSR')
198 ylabel('Rotor Thrust Coefficient C_t[-]')
199 title(['Thrust Coefficient vs TSR at Pitch Angle ' num2str(pitch) '°'])
200
201 Y = figure()
202 % subplot(2,2,2)
203 hold on
204 plot(TSR2,cq)
205 if pitch == 0
206 M_QBlade=[0.20  0.31  0.37  0.43  0.46  0.42  0.39  0.35  0.31 ↵
0.28  0.27  0.26  0.28  0.24  0.09];
207 M_QBladeRF = [0.204562 0.308696  0.370461  0.433401  0.460146  0.423379 ↵
0.386665  0.348606  0.31127 0.270936  0.234931  0.204913  0.171136 ↵
0.13373 0.0864576];
208 cq_QBlade = [0.0550615 0.0830172  0.0996466  0.116619  0.123586  0.113715 ↵
0.103837  0.0944539  0.0846792  0.075447  0.0717026  0.0689261  0.0747046 ↵
0.0645728  0.0241845];
209 cq_QBladeRF = [0.0551216  0.0831815  0.0998248  0.116785  0.123991 ↵
0.114084  0.104191  0.0939356  0.083875  0.0730066  0.0633048  0.0552161 ↵
0.0461146  0.036035  0.0232969];
210 plot(TSR_QBlade,cq_QBlade)
211 plot(TSR_QBlade,cq_QBladeRF)
212 end
213
214 legend('MatLab BEM', 'QBlade', 'Qblade RF = 0.1', 'Location', 'northeast')
215 xlabel('TSR')
216 ylabel('Torque [Nm]')
217 title(['Torque Coefficient vs TSR at Pitch Angle ' num2str(pitch) '°'])
218
219 Z = figure()
220 % subplot(2,2,3)
221 hold on
222 plot(TSR2,Cp)
223 if pitch == 0
224 P_QBlade=[6.4517  7.53505 8.73987 10.0773 11.5597 13.1991 15.0076 17.0018 ↵
```

```
19.1955 21.6056 24.2484 27.1449 30.3062 33.7545 37.5293 41.6688 46.2154 51.0833 ↵
55.8161 59.4478 60.6792 61.9225 63.1993 64.299 65.102 65.7459 66.4665 67.2274 ↵
67.9635 68.6354 69.1689 69.5025 69.9063 70.2258 70.5072 70.6535 70.6951 70.5718 ↵
70.5018 70.4779 70.3324 70.6707 70.5954 70.1029 69.5647 69.0095 68.1972 67.3957 ↵
66.4789 65.6854 64.9125 64.3494 64.049 64.296 64.6865 64.4938 64.3436 64.0136 ↵
60.9657 56.8977 52.2266 45.9432 44.0912 42.1696 40.2263 38.4366 36.6107 35.057 ↵
33.8382 32.9574];
225 Cp_QBladeRF =[0.0551216 0.124772 0.19965 0.291962 0.371974 0.399294 ↵
0.416764 0.42271 0.419375 0.401536 0.379829 0.358905 0.322802 ↵
0.270263 0.186376];
226 Cp_QBlade = [0.06 0.12 0.20 0.29 0.37 0.40 0.42 0.43 0.42 ↵
0.41 0.43 0.45 0.52 0.48 0.19];
227 plot(TSR_QBlade, Cp_QBlade)
228 plot(TSR_QBlade, Cp_QBladeRF)
229 end
230
231 legend('MatLab BEM', 'QBlade', 'Qblade RF = 0.1', 'Location','northwest')
232 xlabel('TSR')
233 ylabel('Rotor Power Coefficient [-] ')
234 title(['Rotor Power Coefficient vs TSR at Pitch Angle ' num2str(pitch) '°'])
```

```

1 function [X, Y, Z] = VaryPitch(Pitchmin, dPitch, Pitchmax, C, twist,rmin, rmax,
RF, U_wind, TSR,r,B,dr, TipLoss ,RootLoss, pitch)
2
3 k=0;
4 TSR2 = TSR;
5 twist2 = twist;
6
7
8 for pitch = Pitchmin:dPitch:Pitchmax
9     twist2 = twist-pitch;
10    k=k+1;
11
12 w = (TSR2*U_wind)/rmax; %rad/s
13
14
15 j=0;
16
17
18 for i = length(r):-1:1
19 a=0.3;
20 b=0.000001;
21 a_prev = 1;
22 b_prev = 1;
23 a_2prev = 0;
24 b_2prev=0;
25 Diff_a = 1;
26 Diff_b = 1;
27 j=0;
28 z=0;
29 %
30 while abs(a-a_prev) > 0.00001 && abs(b-b_prev) > 0.00001% && Diff_a>0.001 &&
Diff_b>0.001
31 Diff_a = abs((a-a_prev)/a_prev);
32 Diff_b = abs((b-b_prev)/b_prev);
33 j=j+1;
34     a_2prev = a_prev;
35     b_2prev=b_prev;
36     a_prev = a;
37     b_prev = b;
38
39 %     Phi = atand( ((1-a)./(1+b)).*((U_wind)./(r(i).*w)) );
40 Un     = U_wind*(1 - a);           % Normal velocity [m/s]
41 Ut     = w.*r(i).*(1 + b);       % Tangential velocity [m/s]
42 Urel   = sqrt(Un.^2 + Ut.^2);    % Relative velocity [m/s]
43 Phi    = atand(Un/Ut);
44
45 alpha  = Phi-twist2(i);           % Angle of Attack [deg]
46
47     c_l   = -0.0025.*alpha.^2 + 0.1122.*alpha + 0.1928; %lift coefficient

```

```

(polynomial approximation)
48     c_d      = 0.0004.*alpha.^2 - 0.0024.*alpha + 0.0173; %Drag coefficient (↵
"
    )
49
50     if alpha>12                                     %Polynomial↵
approximation of high angle Cl and Cd
51         c_l=(alpha-12)*-(1.2/(90-12))+1.1792;
52     elseif alpha < -10
53         c_l = (alpha+10)*(1.2)/(90-12)-1.1792;
54     end
55
56     if alpha > 12 && c_l<0
57         c_l=0;
58     elseif alpha < -10 && c_l>0
59         c_l = 0;
60     end
61
62
63     c_x      = c_l.*sind(Phi)-c_d.*cosd(Phi);
64     c_y      = c_l.*cosd(Phi)+c_d.*sind(Phi);
65 if TipLoss == 1
66     F_tip= max((2/pi) *   acos(exp((-B/2))*(((rmax-r(i))/(r(i)*sind(Phi))))), ↵
0.1);
67 elseif TipLoss == 0
68 F_tip = 1;
69 else
70 msgbox('ERROR! Set tip/root loss to 1 or 0');
71 end
72
73
74 if RootLoss == 1
75     F_root=max(((2/pi) *   acos(exp((-B/2))*abs((((r(i)-rmin)/(r(i)*sind ↵
(Phi))))))))), 0.1);
76 elseif RootLoss == 0
77 F_root = 1;
78 else
79 msgbox('ERROR! Set tip/root loss to 1 or 0');
80 end
81     F=F_tip*F_root;
82
83     sigma = (C(i)*B) / (2*pi*r(i));
84
85 if sind(Phi) == 0
86     a = 1;
87 end
88
89
90     if a_prev <= 0.25
91         a      = 1./(((4.*F.*sind(Phi).^2)./(sigma.*c_y)) + 1);

```

```
92     else
93         K = (4.*F.*sind(Phi).^2)./(sigma.*c_y);
94         a_c=0.2;
95         a = .5.*(2 + K.*(1 - 2.*a_c) - sqrt(abs((K.*(1 - 2.*a_c) + 2).^2 + 4.*(K.*
*a_c.^2 - 1)))));
96     end
97
98
99     if j <10
100         a = a;
101     elseif j <11
102         a = 0.25.*a + 0.5.*a_prev + 0.25.*a_2prev;
103     else
104         a = RF.*a + (1 - RF).*a_prev;
105     end
106     TSRr = (TSR2/rmax)*r(i);
107     b = 0.5.*(sqrt(abs(1 + 4./TSRr.^2.*a.*(1 - a))) - 1);
108
109
110
111     if j>10000
112         break
113     end
114 end
115
116     PHI(i) = Phi;
117     A(i) = a;
118     B2(i) = b;
119     CL(i) = c_l;
120     CD(i) = c_d;
121     ALPHA(i) = alpha;
122     FF(i) = F;
123     SIGMA(i) = sigma;
124 %     KK(i) = K
125 end
126
127 %Calculation of forces
128
129 %enviromental parameters
130 rho = 1.225; %kg/m^3 at 15.5 C
131 mu = 0.00001647; %kg/ms
132
133
134 U = w.*r.*(1+B2);
135 V = U_wind.*(1-A);
136 U_rel = sqrt(U.^2+V.^2);
137
138
139 %area of elements and forces on elements
```

```

140 dA = C*dr;
141
142
143 dFL = (1/2).*rho.*U_rel.^2.*dA.*CL;
144 dFD = (1/2).*rho.*U_rel.^2.*dA.*CD;
145 dFT = dFL.*cosd(PHI)+dFD.*sind(PHI);
146 dFM = dFL.*sind(PHI)-dFD.*cosd(PHI);
147
148 %Calculate total forces on blade
149 FL = sum(dFL);
150 FD = sum(dFD);
151 FT = sum(dFT);
152 FM = sum(dFM);
153
154 %Moment and power on elements
155 dM = r.*dFM;
156 dP = w.*dM;
157 %
158
159 %Total moment and power
160 M = sum(dM);
161 P = sum(dP);
162 P_rot = P*B;
163 A_rotor = pi*rmax^2;
164 T_rot = FT*B;
165 M_rot = M*B;
166
167 % figure(8)
168 % plot(r(1:length(r)),dM)
169
170 Cp(k) = P_rot/(0.5*rho*A_rotor*U_wind^3);
171 Ct(k) = T_rot/(0.5*rho*U_wind^2*A_rotor);
172 cq(k) = M_rot/(0.5*rho*rmax*U_wind^2*A_rotor);
173
174 P3(k)=P_rot;
175 M3(k)=M*3;
176 T3(k)=3*FT;
177
178 end
179
180 pitch2 = [Pitchmin :dPitch: Pitchmax];
181 X = figure()
182 % subplot(2,2,1)
183 hold on
184 plot(pitch2,Ct)
185 pitch_QBlade=[-10.00    -9.00    -8.00    -7.00    -6.00    -5.00    -4.00    -3.00 ↵
-2.00    -1.00    0.00    1.00    2.00    3.00    4.00    5.00    6.00    7.00    8.00 ↵
9.00    10.00    11.00    12.00    13.00    14.00    15.00    16.00    17.00    18.00    19.00 ↵
20.00];

```

```

186
187 if TSR == 4
188 Ct_QBlade = [0.28936    0.328306    0.366122    0.406638    0.450017    0.494794
0.538867    0.582659    0.62374 0.66571 0.703448    0.73445 0.762855    0.789463
0.817614    0.847148    0.875338    0.90242 0.931235    0.962533    0.986027
1.00059 1.01236 1.02697 1.03584 1.04688 1.06428 1.07627 1.08839 1.10235 1.11713];;
189 T_QBlade=[4.30  4.87    5.43    6.04    6.68    7.34    8.00    8.65    9.26
9.88    10.44   10.90   11.32   11.72   12.14   12.58   12.99   13.40   13.82   14.29
14.64   14.85   15.03   15.24   15.38   15.54   15.80   15.98   16.16   16.36
16.58];
190 plot(pitch_QBlade, Ct_QBlade)
191 end
192
193 legend('MatLab BEM', 'QBlade', 'Location', 'northwest')
194 xlabel('Pitch angle[°]')
195 ylabel('Thrust Coefficient [-]')
196 title(['Thrust Coefficient vs Pitch angle at TSR ' num2str(TSR)])
197
198 Y = figure()
199 % subplot(2,2,2)
200 hold on
201 plot(pitch2,cq)
202 if TSR == 4
203 M_QBlade=[0.21  0.23    0.26    0.28    0.30    0.33    0.35    0.36    0.37
0.38    0.39    0.39    0.38    0.38    0.37    0.36    0.35    0.34    0.32    0.31
0.29    0.27    0.24    0.21    0.18    0.15    0.12    0.08    0.04    0.01
-0.03];
204 cq_QBlade = [0.0570465  0.0632661    0.0689187    0.0751804    0.0820413    0.0881152
0.0932111    0.0973972    0.100128    0.10272 0.103942    0.104058    0.103362
0.101707    0.0992121    0.0964629    0.0935468    0.0903303    0.0870079    0.0830695
0.0779356    0.071654    0.0643962    0.057107    0.0485758    0.0398562    0.0314326
0.0218458    0.0118501    0.00164875  -0.0088684];
205 plot(pitch_QBlade,cq_QBlade)
206 end
207
208 legend('MatLab BEM', 'QBlade', 'Location', 'northeast')
209 xlabel('Pitch angle[°]')
210 ylabel('Torque [Nm]')
211 title(['Torque Coefficient vs Pitch angle at TSR ' num2str(TSR)])
212
213 Z = figure()
214 % subplot(2,2,3)
215 hold on
216 plot(pitch2,Cp)
217 if TSR == 4
218 Cp_QBlade = [0.23    0.25    0.28    0.30    0.33    0.35    0.37    0.39    0.40
0.41    0.42    0.42    0.41    0.41    0.40    0.39    0.37    0.36    0.35    0.33
0.31    0.29    0.26    0.23    0.19    0.16    0.13    0.09    0.05    0.01
-0.04];

```

```
219 plot(pitch_QBlade, Cp_QBlade)
220 end
221
222 legend('MatLab BEM', 'QBlade', 'Location', 'northeast')
223 xlabel('Pitch angle[°]')
224 ylabel('Power coefficient C_p')
225 title(['Power Coefficient vs Pitch angle at TSR ' num2str(TSR)])
```

```

1 function [X, Y, Z] = VaryWind(U_windmin, dU_wind, U_windmax, C, twist, rmin,
rmax, RF, U_wind, TSR,r,B,dr, TipLoss ,RootLoss, pitch)
2
3 k=0;
4 TSR2 = TSR;
5 twist2 = twist - pitch;
6
7
8 for U_wind = U_windmin:dU_wind:U_windmax
9     k=k+1;
10
11 w = (TSR2*U_wind)/rmax; %rad/s
12
13
14 j=0;
15
16
17 for i = length(r):-1:1
18 a=0.3;
19 b=0.000001;
20 a_prev = 1;
21 b_prev = 1;
22 a_2prev = 0;
23 b_2prev=0;
24 Diff_a = 1;
25 Diff_b = 1;
26 j=0;
27 z=0;
28 %
29 while abs(a-a_prev) > 0.00001 && abs(b-b_prev) > 0.00001% && Diff_a>0.001 &&
Diff_b>0.001
30 Diff_a = abs((a-a_prev)/a_prev);
31 Diff_b = abs((b-b_prev)/b_prev);
32 j=j+1;
33     a_2prev = a_prev;
34     b_2prev=b_prev;
35     a_prev = a;
36     b_prev = b;
37
38 %     Phi = atand( ((1-a)./(1+b)).*((U_wind)./(r(i).*w)) );
39 Un     = U_wind*(1 - a);           % Normal velocity [m/s]
40 Ut     = w.*r(i).*(1 + b);       % Tangential velocity [m/s]
41 Urel   = sqrt(Un.^2 + Ut.^2);    % Relative velocity [m/s]
42 Phi    = atand(Un/Ut);
43
44 alpha  = Phi-twist2(i);           % Angle of Attack [deg]
45
46     c_l   = -0.0025.*alpha.^2 + 0.1122.*alpha + 0.1928; %lift coefficient
(polynomial approximation)

```

```

47     c_d      = 0.0004.*alpha.^2 - 0.0024.*alpha + 0.0173; %Drag coefficient (↵
"
48
49     if alpha>12                                     %Polynomial↵
approximation of high angle Cl and Cd
50         c_l=(alpha-12)*-(1.2/(90-12))+1.1792;
51     elseif alpha < -10
52         c_l = (alpha+10)*(1.2)/(90-12)-1.1792;
53     end
54
55     if alpha > 12 && c_l<0
56         c_l=0;
57     elseif alpha < -10 && c_l>0
58         c_l = 0;
59     end
60
61
62     c_x      = c_l.*sind(Phi)-c_d.*cosd(Phi);
63     c_y      = c_l.*cosd(Phi)+c_d.*sind(Phi);
64
65     if TipLoss == 1
66         F_tip= max((2/pi) *   acos(exp((-B/2))*(((rmax-r(i))/(r(i)*sind(Phi))))), ↵
0.1);
67     elseif TipLoss == 0
68         F_tip = 1;
69     else
70         msgbox('ERROR! Set tip/root loss to 1 or 0');
71     end
72
73
74     if RootLoss == 1
75         F_root=max(((2/pi) *   acos(exp((-B/2))*abs((((r(i)-rmin)/(r(i)*sind ↵
(Phi))))))))), 0.1);
76     elseif RootLoss == 0
77         F_root = 1;
78     else
79         msgbox('ERROR! Set tip/root loss to 1 or 0');
80     end
81     F=F_tip*F_root;
82
83     sigma = (C(i)*B) / (2*pi*r(i));
84
85     if sind(Phi) == 0
86         a = 1;
87     end
88
89
90     if a_prev <= 0.25
91         a      = 1./(((4.*F.*sind(Phi).^2)./(sigma.*c_y)) + 1);

```

```
92     else
93         K = (4.*F.*sind(Phi).^2)./(sigma.*c_y);
94         a_c=0.2;
95         a = .5.*(2 + K.*(1 - 2.*a_c) - sqrt(abs((K.*(1 - 2.*a_c) + 2).^2 + 4.*(K.*
*a_c.^2 - 1)))));
96     end
97
98
99     if j <10
100         a = a;
101     elseif j <11
102         a = 0.25.*a + 0.5.*a_prev + 0.25.*a_2prev;
103     else
104         a = RF.*a + (1 - RF).*a_prev;
105     end
106     TSRr = (TSR2/rmax)*r(i);
107     b = 0.5.*(sqrt(abs(1 + 4./TSRr.^2.*a.*(1 - a))) - 1);
108
109
110
111     if j>10000
112         break
113     end
114 end
115
116     PHI(i) = Phi;
117     A(i) = a;
118     B2(i) = b;
119     CL(i) = c_l;
120     CD(i) = c_d;
121     ALPHA(i) = alpha;
122     FF(i) = F;
123     SIGMA(i) = sigma;
124 %     KK(i) = K
125 end
126
127 %Calculation of forces
128
129 %enviromental parameters
130 rho = 1.225; %kg/m^3 at 15.5 C
131 mu = 0.00001647; %kg/ms
132
133
134 U = w.*r.*(1+B2);
135 V = U_wind.*(1-A);
136 U_rel = sqrt(U.^2+V.^2);
137
138
139 %area of elements and forces on elements
```

```

140 dA = C*dr;
141
142
143 dFL = (1/2).*rho.*U_rel.^2.*dA.*CL;
144 dFD = (1/2).*rho.*U_rel.^2.*dA.*CD;
145 dFT = dFL.*cosd(PHI)+dFD.*sind(PHI);
146 dFM = dFL.*sind(PHI)-dFD.*cosd(PHI);
147
148 %Calculate total forces on blade
149 FL = sum(dFL);
150 FD = sum(dFD);
151 FT = sum(dFT);
152 FM = sum(dFM);
153
154 %Moment and power on elements
155 dM = r.*dFM;
156 dP = w.*dM;
157 %
158
159 %Total moment and power
160 M = sum(dM);
161 P = sum(dP);
162 P_rot = P*B;
163 A_rotor = pi*rmax^2;
164
165 % figure(8)
166 % plot(r(1:length(r)),dM)
167
168 Cp(k) = P_rot/(0.5*rho*A_rotor*U_wind^3);
169
170 P3(k)=P_rot;
171 M3(k)=M*3;
172 T3(k)=3*FT;
173
174 end
175 U_wind2 = [U_windmin :dU_wind:U_windmax];
176 X = figure();
177 % subplot(2,2,1);
178 hold on
179 plot(U_wind2,T3)
180
181 U_QBlade=[4.00  4.50  5.00  5.50  6.00  6.50  7.00  7.50  8.00 ↵
8.50  9.00  9.50  10.00  10.50  11.00  11.50  12.00  12.50  13.00  13.50 ↵
14.00  14.50  15.00  15.50  16.00  16.50  17.00  17.50  18.00  18.50  19.00 ↵
19.50  20.00  20.50  21.00  21.50  22.00  22.50  23.00  23.50  24.00  24.50 ↵
25.00  25.50  26.00  26.50  27.00  27.50  28.00  28.50  29.00  29.50 ↵
30.00];
182 if pitch == 0 && TSR == 4
183 T_QBlade=[1.35  1.71  2.11  2.56  3.04  3.57  4.14  4.76  5.41 ↵

```

```
6.11    6.85    7.63    8.46    9.32    10.23   11.18   12.18   13.21   14.29   15.41 ↵
16.57   17.78   19.03   20.32   21.65   23.02   24.44   25.90   27.40   28.94   30.53 ↵
32.15   33.82   35.54   37.29   39.09   40.93   42.81   44.73   46.70   48.71   50.76 ↵
52.85   54.99   57.16   59.38   61.64   63.95   66.30   68.68   71.12   73.59 ↵
76.10];
184 plot(U_QBlade, T_QBlade)
185 end
186 legend('MatLab BEM', 'QBlade', 'Location','northwest')
187 xlabel('U_w_i_n_d [m/s]')
188 ylabel('Thrust Force [N]')
189 title(['Thrust Force vs Wind speed at TSR ' num2str(TSR) ' and Pitch Angle ' ↵
num2str(pitch) '°'])
190
191 Y = figure();
192 % subplot(2,2,2)
193 hold on
194 plot(U_wind2,M3)
195 if pitch == 0 && TSR == 4
196 M_QBlade=[0.05  0.06  0.08  0.09  0.11  0.13  0.15  0.18  0.20 ↵
0.23  0.25  0.28  0.31  0.34  0.38  0.41  0.45  0.49  0.53  0.57 ↵
0.61  0.66  0.70  0.75  0.80  0.85  0.90  0.96  1.01  1.07  1.13 ↵
1.19  1.25  1.31  1.38  1.44  1.51  1.58  1.65  1.72  1.80  1.87 ↵
1.95  2.03  2.11  2.19  2.28  2.36  2.45  2.54  2.63  2.72 ↵
2.81];
197 plot(U_QBlade,M_QBlade)
198 end
199
200 legend('MatLab BEM', 'QBlade', 'Location','northeast')
201 xlabel('U_w_i_n_d [m/s]')
202 ylabel('Torque [Nm]')
203 title(['Torque vs Wind speed at TSR ' num2str(TSR) ' and Pitch Angle ' num2str ↵
(pitch) '°'])
204
205 Z = figure();
206 % subplot(2,2,3)
207 hold on
208 plot(U_wind2, P3)
209 if pitch == 0 && TSR == 4
210 P_QBlade=[3.20  4.55  6.24  8.31  10.79  13.72  17.14  21.08  25.58 ↵
30.68  36.42  42.83  49.96  57.83  66.50  75.98  86.33  97.58  109.76 ↵
122.92 137.09 152.31 168.61 186.04 204.64 224.43 245.45 267.75 291.37 ↵
316.33 342.67 370.45 399.68 430.41 462.68 496.52 531.97 569.07 607.86 ↵
648.37 690.64 734.71 780.62 828.40 878.09 929.73 983.36 1039.00 1096.71 ↵
1156.52 1218.47 1282.58 1348.91];
211 % Cp_QBlade = [0.06 0.12  0.20  0.29  0.37  0.40  0.42  0.43  0.42 ↵
0.41  0.43  0.45  0.52  0.48  0.19];
212 plot(U_QBlade, P_QBlade)
213 end
214
```

```
215 legend('MatLab BEM', 'QBlade', 'Location', 'northwest')
216 xlabel('U_w_i_n_d [m/s]')
217 ylabel('Rotor powe Power [W]')
218 title(['Rotor Power vs Wind speed at TSR ' num2str(TSR) ' and Pitch Angle ' ↵
num2str(pitch) '°'])
```